UNIVERSITÀ DEGLI STUDI "G. d'Annunzio"

Chieti-Pescara

SCUOLA SUPERIORE "G. d'Annunzio"

DOTTORATO DI RICERCA IN MEDICINA TRASLAZIONALE

CICLO XXXVIII

p16INK4a loss in perioperative metastatic progression of adrenocortical carcinoma: preclinical modeling and CAR T-Cell immunotherapy

Dipartimento di **Medicina e Scienze dell'Invecchiamento**

Settore Scientifico Disciplinare **MEDS-02/A**

Dottorando
Dott.ssa Isabella D'Amario

Coordinatore
Prof.ssa Antonia Patruno

Tutor
Prof.Renato Mariani-Costantini

Co-tutor
Dott. Fabio Verginelli

Anni Accademici 2022/2025

Abstract

Adrenocortical carcinoma (ACC) is a rare and aggressive malignancy characterized by considerable biological, molecular, and clinical heterogeneity, with limited therapeutic options and poor prognosis. This doctoral thesis aimed to investigate the perioperative metastatic progression of ACC, focusing on the role of p16INK4a loss, through integrated molecular characterization, preclinical model development, and evaluation of novel immunotherapy approaches.

A case study of a 60-year-old female patient with advanced-stage ACC, presenting with autonomous cortisol secretion, hyperandrogenism, multiple hepatic metastases, and an inferior vena cava (IVC) tumor thrombus, was analyzed in depth. Despite extensive cytoreductive surgery and initiation of adjuvant mitotane therapy, the patient experienced rapid metastatic progression and succumbed within 40 days postoperatively. Comprehensive histopathological, immunohistochemical, and ultrastructural analyses revealed a high-grade conventional ACC with heterogeneous expression of diagnostic markers and two distinct cellular morphotypes exhibiting active steroidogenesis and mitochondrial dysfunction.

Genomic profiling using targeted next-generation sequencing (NGS) and comparative genomic hybridization-single nucleotide polymorphism (CGH-SNP) arrays identified a likely pathogenic TP53 missense mutation and extensive chromosomal instability (CIN), notably a homozygous deletion of the CDKN2A/B locus at 9p21.3, encoding the tumor suppressors p16INK4a, p14ARF, and p15INK4b. Immunohistochemistry demonstrated heterogeneous p16INK4a expression in the primary tumor, with complete loss in metastatic lesions and tumor thrombus, correlating with increased proliferative indices (Ki67) and mitotic activity, implicating p16INK4a loss as a driver of aggressive metastatic behavior and a potential biomarker of poor prognosis.

To model tumor biology, patient-derived in vitro and in vivo systems were established, including primary ACC cell cultures, patient-derived xenografts (PDXs), and cell line-derived xenografts (CDXs). The established cellular and xenograft models replicate key biological, histological, molecular, and functional features of ACC including steroid hormone production, providing robust platforms for mechanistic studies, drug testing, and preclinical therapeutic screening of identified vulnerabilities. Multiplex immunophenotyping revealed a predominantly immune-cold tumor microenvironment with preserved expression of B7-H3 (CD276), an immune checkpoint molecule.

Leveraging this, B7-H3-targeted chimeric antigen receptor (CAR) T cells were generated and demonstrated potent cytotoxic activity in co-culture assays against established ACC lines,

primary tumor–derived cells, and xenograft-derived cells, supporting the therapeutic potential of CAR T-cell immunotherapy for ACC, particularly in aggressive, metastatic, and treatment-resistant contexts.

This thesis provides novel insights into the molecular mechanisms underpinning perioperative metastatic progression in ACC, highlighting the critical role of CDKN2A/B deletion and p16INK4a loss in promoting tumor proliferation and metastasis within a CIN-driven context. The established patient-derived models constitute valuable platforms for mechanistic studies and preclinical evaluation of targeted and immune-based therapies. The promising preclinical efficacy of B7-H3 CAR T cells warrants further investigation as a potential personalized therapeutic option for aggressive and metastatic ACC, supporting future clinical translation in treatment-resistant disease settings.

Collectively, these findings contribute to advancing the understanding of ACC biology and open avenues for the development of innovative treatment strategies aimed at improving outcomes in this challenging malignancy.

Keywords: Adrenocortical carcinoma, p16INK4a, CDKN2A/B deletion, chromosomal instability, metastasis, patient-derived models, CAR T-cell therapy, immunotherapy, tumor microenvironment, steroidogenesis.

Table of contents

Introduction 8

1 Adrenocortical gland 8

1.1 Functional zonation and hormone production 8

1.2 Cellular origins and renewal mechanisms 9

1.3 Key regulatory pathways 11

1.4 Adrenocortical diseases 12

2 Adrenocortical carcinoma: 13

2.1 Epidemiology and Incidence 13

2.2 Clinical Presentation 13

3 Diagnosis and classification 15

3.1 Diagnostic approaches 15

3.2 WHO Classification 16

3.3 Histopathological diagnosis and diagnostic markers of ACC 17

3.4 Hormonal evaluation 18

3.5 Radiological and morphological diagnosis (Imaging) 19

3.6 ACC Staging 21

3.7 Prognosis and clinical relevance 22

4 ACC therapies 24

4.1 Localized adrenocortical carcinoma: 24

4.1.1 Surgery 24

4.1.2 ACC Adjuvant therapy 25

4.2 Therapies for metastatic ACC 28

4.2.1 Molecularly targeted therapy 29

4.2.2 ACC tumor microenvironment 31

4.2.3 ACC Immunotherapy 32
5 Preclinical models 33
Purpose of the study 35
Materials and Methods 37
Ethics Statement 37
Sample collection and processing 37
Genetic characterization 37
Next-Generation Sequencing (NGS) and Comparative Genomic Hybridization – Single Nucleotide Polymorphism array (CGH-SNP) 38
Microsatellite Instability Analysis 40
Primary cell culture establishment 40
Determination of hormone production in ID7ACC cell culture 42
Flow Cytometry Immunophenotyping 43
In vitro CAR T cell co-culture 44
Generation of Patient- and Cell-Derived Xenograft models 45
Histopathology and immunohistochemical procedures 46
Transmission Electron Microscopy 47
MACSima Imaging Cyclic Staining (MICS) 47
Antibody staining and MICS setup 48
MACSima Imaging Cycling Staining 48
Results 50
Clinicopathological presentation 50
Integrated histopathological, immunophenotypic, and ultrastructural characterization of the tumor 53
Mutational and structural genetic landscape 56
Correlation of $p16^{INK4a}$ status with tumor proliferation and mitotic instability 65
MACSima characterization of ACC primary tumor and hepatic metastasis 71
Establishment and characterization of in vitro and in vivo models 77

Morphological and proliferative stability of ID7 ACC cell model 78
Evaluation of Hormone Secretion Profiles of ID7ACC cell model 79
Flow cytometric phenotypic characterization of ACC cell lines 82
Integrated histopathological and immunophenotypic characterization of the ID7 CDX model 84
Histopathological and ultrastructural characterization of PDX and CDX models 86
Evaluation of CAR T cell–induced tumor killing in ACC primary cultures and in commercial cell lines 92
Discussion and conclusions 94
Bibliography 101

Introduction

1 Adrenocortical gland

1.1 Functional zonation and hormone production

The adrenal glands are vital endocrine organs that play essential roles in maintaining body homeostasis by regulating metabolism, stress response, immune function, and electrolyte balance. They are located bilaterally above the kidneys and consist of two distinct tissues with different developmental origins and functions: the adrenal cortex, derived from the mesodermal coelomic epithelium and specialized in the production of steroid hormones, and the adrenal medulla, of ectodermal origin, which contains chromaffin cells that secrete catecholamines [1]. The adrenal cortex constitutes approximately 90% of the gland and is organized into three histologically and functionally distinct zones that together ensure the coordinated production of steroid hormones [2,3]. During the perinatal period, the establishment of this functional zonation leads to the formation of three concentric layers: the zona glomerulosa (zG), the zona fasciculata (zF), and the zona reticularis (zR). This zonal organization must be actively maintained throughout life, despite the continuous centripetal renewal of cortical cells [4]. The adrenal capsule, which surrounds the gland, not only provides structural support but also serves as a niche for stem and progenitor cells that contribute to this lifelong regeneration [3,4]. Each cortical zone exhibits distinct structural and biochemical characteristics that determine its specific hormonal output. The zona glomerulosa, the outermost layer, is part of the renin–angiotensin–aldosterone system (RAAS) and is responsible for the synthesis of mineralocorticoids, primarily aldosterone. This hormone promotes sodium and water retention while facilitating potassium excretion, thereby regulating extracellular fluid volume and blood pressure. Aldosterone acts on multiple epithelial tissues, including the distal convoluted tubules and collecting ducts of the kidney, where it fine-tunes sodium and potassium balance, as well as on sweat glands, salivary glands, and the intestinal epithelium [5]. In the absence of aldosterone, urinary sodium excretion increases and urinary volume rises. Its secretion is stimulated by angiotensin II through the RAAS, as well as by ACTH, hyperkalemia, hyponatremia, and physiological stress or trauma [5,6]. The zona fasciculata, the largest and

middle layer of the adrenal cortex, synthesizes glucocorticoids, primarily cortisol, under the control of the hypothalamic–pituitary–adrenal (HPA) axis. The hypothalamus secretes corticotropin-releasing hormone (CRH), which stimulates the anterior pituitary to release adrenocorticotropic hormone (ACTH), thereby promoting cortisol synthesis in zF cells via the melanocortin 2 receptor (MC2R) [2,7]. Circulating cortisol levels follow a circadian rhythm, peaking in the early morning and declining throughout the day in synchrony with the sleep–wake cycle [5]. Functionally, cortisol is crucial for metabolic regulation, as it influences glucose production, lipid metabolism, and protein catabolism, while also exerting potent anti-inflammatory and immunosuppressive effects [2]. The zona reticularis, the innermost cortical layer, has a characteristic net-like histological appearance, from which its name derives. It primarily produces adrenal androgens, including dehydroepiandrosterone (DHEA) and androstenedione, which serve as precursors for the synthesis of more potent sex steroids such as testosterone and estrogen in peripheral tissues [4,5]. The secretion of these weak androgens is regulated by ACTH, and their excess can result in hirsutism, acne, oligomenorrhea, and virilization in females, or precocious puberty in males [5]. All steroid hormones of the adrenal cortex derive from cholesterol, which is transported into the mitochondria by the Steroidogenic Acute Regulatory (StAR) protein, where CYP11A1 catalyzes its conversion into pregnenolone, the universal precursor of all steroids. The sequential actions of cytochrome P450 (CYP) enzymes and hydroxysteroid dehydrogenases (HSDs) within the mitochondria and endoplasmic reticulum lead to the production of specific steroid hormones in each zone [7].

Overall, the adrenal cortex represents a highly dynamic and specialized endocrine tissue. Its functional zonation enables a spatially organized synthesis of distinct steroid hormones essential for maintaining homeostasis. The continuous renewal and remodeling of cortical zones ensure the adaptability of the gland to changing physiological demands and stressors throughout life [2,5].

1.2 Cellular origins and renewal mechanisms

The adult adrenal cortex is a dynamic and sexually dimorphic tissue that relies on coordinated stem/progenitor cell activity, lineage conversion and paracrine/endocrine signaling to sustain continuous renewal and adapt to physiological demands. Under homeostatic conditions, adrenocortical renewal originates in the outermost regions of the gland, where resident, where

resident stem and progenitor populations, including GLI1$^+$ capsular cells and SHH$^+$ subcapsular progenitors, continually generate new steroidogenic cells [8,9].

Newly formed cells migrate centripetally through the cortex, differentiating first into zona glomerulosa (zG) cells, and subsequently undergoing lineage conversion into zona fasciculata (zF) cells, before reaching the corticomedullary boundary, where senescent cells are eliminated. This classic "centripetal migration" model, first proposed in the 19th century, is strongly validated by modern lineage-tracing studies, which show radial stripes of Shh$^+$ and Gli1$^+$ descendants moving inward across cortical zones [9,10]. Lineage tracing of CYP11B2$^+$ cells confirms that differentiated zG cells directly convert into zF cells during both homeostasis and regeneration, demonstrating that lineage conversion of mature cells is a key mechanism of cortical renewal[11]. Additional mapping studies indicate that the mesenchymal capsule acts as a bona fide stem cell niche, containing GLI1$^+$ and WT1$^+$ stem cell populations capable of self-renewal and differentiation, although their contribution is modest under basal conditions and becomes significant only under endocrine stress, such as glucocorticoid-induced atrophy or gonadectomy [12]. Multiple progenitor reservoirs also exist in the juxtamedullary region and appear to be activated under specific developmental or stress conditions, supporting the concept that adrenocortical renewal arises from a combination of stem cell activation, progenitor differentiation, and cellular plasticity [4]. Indeed, plasticity mechanisms, including transdifferentiation and dedifferentiation, allow differentiated cortical cells to adopt alternative identities, ensuring functional redundancy and rapid adaptation to physiological or pathological demands. Adrenal renewal is further modulated by sex hormones; androgens restrict recruitment of GLI1$^+$ stem cells, leading to higher renewal rates in females and potentially explaining sex-biased susceptibility to adrenal pathologies [8,12]. Once established, zG and zF undergo lifelong renewal regulated by feedback loops involving SF-1, WNT and SHH pathways, with SF-1 playing an essential role in maintaining zonal identity and supporting lineage conversion, even though SF-1-independent mechanisms exist and can sustain functional zF formation after zG-specific SF-1 loss [11].

Collectively, genetic fate-mapping, molecular profiling and physiological studies converge to support centripetal migration as the fundamental mechanism governing adrenocortical renewal, while revealing that diverse stem/progenitor pools and cell plasticity cooperate to maintain tissue integrity and functional zonation throughout life [10,13].

1.3 Key regulatory pathways

The architecture, function, and renewal of the adrenal cortex are regulated by a complex interplay of systemic, paracrine, and intracellular pathways. At the endocrine level, ACTH is the main driver of steroidogenesis, acting through the cAMP/PKA signalling cascade and controlling StAR expression, which is essential for glucocorticoid production and the maintenance of zona fasciculata identity [14]. Alongside this systemic regulation, local signalling pathways, particularly WNT/β-catenin, play a central role in defining and preserving adrenal cortical zonation. This pathway controls the fate of subcapsular progenitor cells, guiding them toward a zona glomerulosa lineage and ensuring the proper establishment of distinct cortical layers [4,15].

Homeostatic renewal of the cortex relies on the recruitment of capsular Rspo3+/Gli1+/Sf1– stem cells and subcapsular/zG Shh+/Wnt4+/Sf1+ progenitor cells, coordinated through RSPO/WNT/β-catenin and SHH signalling pathways. These progenitors differentiate into zG cells that are displaced centripetally and eventually converted into zF cells. Stem/progenitor populations are maintained by reciprocal signals: Rspo3 induces Wnt4 and Shh expression in steroidogenic cells, while Shh signals back to recruit capsular cells [13].

The adrenal capsule actively contributes to this process by acting as a signalling niche, producing key factors such as RSPO3 that enhance WNT signalling and support centripetal cortical renewal [4,8]. In the adult cortex, WNT and PKA pathways have complementary roles in maintaining functional zonation. Experimental models have shown that RSPO/WNT/β-catenin signalling drives zG identity, represses zF identity, and can be tumorigenic when constitutively activated. Cortical homeostasis also involves growth-regulatory pathways such as ERK1/2, which integrate diverse extracellular signals and contribute to hypertrophy, adaptive remodelling, and stress-induced proliferation [16]. The epigenetic regulator EZH2 further fine-tunes these processes by promoting steroidogenic differentiation, restraining alternative lineage genes, and modulating responsiveness to PKA signalling [17].

Finally, interactions between gonadal hormones and β-catenin signalling have been identified as an additional regulatory layer. Androgen receptor–β-catenin crosstalk influences progenitor recruitment and proliferation, providing a mechanistic basis for sexual dimorphism in adrenal size and renewal, and suggesting that PKA-mediated cortex remodelling may contribute to the higher prevalence of adrenocortical diseases in women [8,13]. Overall, integrative analyses indicate that these systemic and local pathways converge to maintain cortical zonation, growth balance, and hormonal output throughout life [18].

1.4 Adrenocortical diseases

Disorders of the adrenal cortex represent a heterogeneous group of endocrine conditions that can broadly be divided into three categories: adrenal insufficiency, adrenal hyperfunction, and proliferative or neoplastic lesions. These diseases vary widely in etiology, clinical presentation, and prognosis, yet all reflect alterations in hormone synthesis, secretion, or cellular proliferation within the adrenal cortex[19,20].

Adrenal insufficiency (AI) is characterized by inadequate production of adrenal steroids. It may be primary, due to intrinsic adrenal damage (as in autoimmune Addison's disease, infections, or genetic defects in steroidogenesis), or secondary/tertiary, resulting from impaired ACTH secretion by the pituitary or hypothalamus[19,21–24]. Conversely, adrenal hyperfunction arises from excessive production of one or more classes of cortical hormones, leading to conditions such as Cushing's syndrome (hypercortisolism), resulting from chronic glucocorticoid excess [22,25–28], primary aldosteronism (Conn's syndrome), the most frequent cause of secondary hypertension, caused by autonomous aldosterone secretion and adrenogenital syndromes, such as congenital adrenal hyperplasia (CAH), resulting from enzymatic defects in steroidogenesis and androgen excess [22,23,26,29].

Finally, adrenocortical proliferative disorders range from benign hyperplasias and adenomas to malignant carcinomas. These lesions can be either hormonally active—causing clinical hyperfunction—or non-functioning, detected incidentally on imaging studies [23,27,30,31,31,32].

Overall, adrenal cortical diseases represent a heterogeneous group of disorders arising from hormonal imbalance, enzymatic defects, and genetic or neoplastic alterations. Recent advances in molecular genetics have greatly enhanced our understanding of their pathogenesis, enabling more precise classification and the development of targeted therapeutic strategies. Given their biological complexity and the frequent overlap in clinical manifestations, a comprehensive diagnostic approach that integrates hormonal evaluation, imaging techniques, and molecular or genetic profiling is now considered the standard of care [20,31].

2 Adrenocortical carcinoma:

2.1 Epidemiology and Incidence

Adrenocortical carcinoma (ACC) is a rare and biologically heterogeneous malignancy of the adrenal cortex. Epidemiologically, ACC has an estimated incidence in Western populations of 0.5–2.0 new cases per million individuals per year, with most studies reporting values near 0.7–1.5/million [33–36]; incidence varies by geographic region and registry and is influenced by the increased detection of incidental adrenal masses through modern imaging [32,33]. Data from the SEER (Surveillance, Epidemiology, and End Results) database, covering over 28% of the U.S. population, confirm the rarity of ACC and provide detailed information on patient demographics, tumor characteristics, stage at diagnosis, treatment modalities, and survival outcomes. According to SEER, the annual incidence of ACC in adults is approximately 1 per million, while pediatric ACC occurs at a rate of 0.2 per million children per year [32,36–38].

ACC shows a bimodal age distribution, with a small pediatric peak, often linked to hereditary syndromes, and a larger adult peak in the fourth and fifth decades of life [33,34,39]. The disease is more common in females , with a female-to-male ratio of approximately 1.5. Pediatric ACC accounts for less than 0.2% of all childhood malignancies [40–42] and is more frequent in girls (male-to-female ratio 1:2)[32,40,42], with peak incidence between 1 and 4 years of age and a mean age at diagnosis of 5 years [32,34]. In southern Brazil, pediatric incidence is significantly higher, reaching 4 cases per million in children under 10 years, likely due to the high prevalence of germline TP53 mutations (R337H)[32,36,39,40,42] . Up to 50–80% of pediatric patients present with genetic or epigenetic anomalies involving TP53 [42].

ACC constitutes about 1–14% of adrenal incidentalomas and is one of the most common indications for adrenalectomy [32,43]. Pediatric ACC exhibits distinct biological and clinical behavior compared to adult disease, with younger patients (<4 years) generally demonstrating better outcomes [38,39,41]. Due to its complexity, heterogeneous presentation, and high risk of recurrence, all patients with suspected or confirmed ACC should be managed within a multidisciplinary expert team [44].

2.2 Clinical Presentation

Adrenocortical carcinoma (ACC) presents with a wide and variable clinical spectrum, which depends heavily on whether the tumor is hormonally active (functional) or non-functioning [32,36,39,45]. Approximately 40–60% of ACCs secrete steroids such as cortisol, androgens, or more

rarely estrogens or mineralocorticoids, making functional tumors the most common clinical scenario [20,36,39,45–51]. In functionally active ACCs, excess of glucocorticoids most commonly lead to Cushing's syndrome, manifesting as rapid weight gain, muscle weakness, hypertension, glucose intolerance, diabetes mellitus and skin changes [20,32,36,42,47,49,50,52–54]. Androgen-secreting tumors may cause virilization in women, including acne, hirsutism and menstrual irregularities and androgenic alopecia while estrogen-secreting tumors, although rare, can lead to feminization in men, gynecomastia, reduced libido, testicular atrophy, a presentation that is almost invariably associated with a malignant etiology [36,47–50,52,53]. Mineralocorticoid (aldosterone) excess is uncommon but can induce hypertension and hypokalemia. Importantly, some ACCs can produce a mixed hormonal profile, for instance, both cortisol and androgens , which is more typical of malignant adrenocortical tumors [36,39,45,47–50,53].

In contrast, non-secreting (non-functional) ACCs, which account for approximately 30–40% of cases depending on the series, do not produce clinically significant hormone excess and therefore remain silent until they reach a considerable size. These tumors frequently present with non-specific symptoms related to mass effect, such as abdominal or flank pain, early satiety, abdominal fullness, back pain, nausea or fatigue. Systemic symptoms like fever, weight loss, or night sweats occur only in a minority of patients, and it is noteworthy that even large non-functional ACCs may cause surprisingly little constitutional discomfort [20,32,36,48–50,53,54]. Many hormonally "silent" tumors nevertheless exhibit elevated steroid precursors (e.g., DHEA-S or androstenedione), reflecting their adrenocortical origin and the enzymatic dysregulation typical of malignancy. Because of their silent hormonal profile, non-functional ACCs are more likely to be diagnosed at an advanced stage, often with local invasion or metastasis. Indeed, one multicenter study showed that non-secreting ACC had a significantly longer median overall survival (115 months) compared to cortisol- or mixed-secreting tumors [55–57].

ACC can also present as an incidentally discovered adrenal mass. With the widespread use of abdominal CT and MRI, 10–20% of ACCs are now diagnosed as adrenal incidentalomas, although the proportion of incidentalomas that turn out to be ACC is low (1–4%). These incidentally detected tumors are often non-functional or minimally symptomatic, and their deep retroperitoneal location contributes to delayed detection; as a result, a substantial proportion is already large, locally advanced, or invading major vessels, such as the renal vein or inferior vena cava, at the time of diagnosis [20,39,47–50,52–54]. Thus, the functional status of ACC is not only central to its clinical presentation, determining whether endocrine syndromes are evident, but also plays a critical role in disease behavior and prognosis.

3 Diagnosis and classification

3.1 Diagnostic approaches

Adrenocortical carcinoma (ACC) presents significant diagnostic and classification challenges due to its heterogeneity and its frequent overlap with benign adrenal lesions, making early and accurate identification essential for clinical management and prognostic assessment. Diagnosis of ACC relies on an integrated approach that includes clinical evaluation, hormonal assessment, adrenal-focused imaging, and, crucially, histopathological examination[39]. The differential diagnosis of an adrenal mass is broad, encompassing adrenocortical hyperplasia, adenomas, myelolipoma, pheochromocytoma, ACC, metastatic lesions, adrenal hemorrhage, and infectious processes such as tuberculosis; therefore, two key considerations in the initial workup are the assessment of hormonal activity and the exclusion of malignancy [58]. For this reason, every patient with suspected ACC should undergo a detailed clinical assessment, including a thorough case history and physical examination for signs of adrenal hormone excess, followed by structured biochemical work-up and imaging prior to surgery[44,58]. Most patients (40–60%) present with steroid hormone excess—typically glucocorticoids, mineralocorticoids, or androgens or, in approximately 30% of cases, with abdominal mass effects, although 15–20% of ACCs are discovered incidentally [36]. The European Network for the Study of Adrenal Tumors (ENS@T) recommends a comprehensive pre-operative hormonal evaluation in all suspected cases and emphasizes a multidisciplinary diagnostic approach [33,36].

From a pathological perspective, the recently published WHO 5th edition classification has refined diagnostic criteria by categorizing histopathological features into “essential” and “desirable” components, supporting the correct application of the various multi-parametric scoring systems used to distinguish ACC from its mimics, including special variants such as oncocytic or pediatric tumors[59]. ACCs display pronounced intratumoral heterogeneity, both histologically and endocrinologically, including the characteristic phenomenon of “disorganized” or “combined” steroidogenesis, which differentiates them from normal adrenal cortex and adrenocortical adenomas [59]. While ACCs with overt invasive growth or distant metastasis are generally easy to recognize, distinguishing low-grade, noninvasive ACC from benign adenomas remains challenging; this diagnostic ambiguity has historically led to intermediate terms such as “atypical adenoma” or “adrenocortical neoplasm of uncertain malignant potential.” Traditional indicators such as tumor size and weight are not always

reliable, and several algorithms and scoring systems have therefore been developed to improve diagnostic discrimination between adenoma and carcinoma [60]. These scoring frameworks, together with updated histologic criteria and molecular insights, contribute to a more standardized diagnostic pathway but still require integration with clinical and biochemical information to ensure accuracy. The diagnosis of malignancy ultimately relies on a combination of clinical, biological, radiological, and pathological data, evaluated before and after tumor removal [61]. As a result, modern diagnostic practice emphasizes a multimodal, stepwise process that synthesizes endocrine function, imaging characteristics, and histopathological criteria, serving as the foundation for subsequent prognostic stratification and treatment planning.

3.2 WHO Classification

The fifth edition of the WHO classification of endocrine and neuroendocrine tumors provides a comprehensive and integrated framework for the diagnosis of adrenocortical neoplasms, emphasizing the use of multiparameter diagnostic algorithms to improve reproducibility and account for the biological heterogeneity of these tumors. Essential criteria for the diagnosis of adrenocortical carcinoma (ACC) include the application of validated scoring systems, such as the Weiss and modified Weiss systems, the Helsinki score, and the reticulin algorithm, together with confirmation of adrenocortical origin and assessment of proliferative activity through mitotic count and Ki-67 index [31,59]. Histopathology remains the cornerstone of diagnosis, but the 5th edition also integrates contemporary molecular insights to support a more refined and personalized approach to risk stratification [62].

One of the most relevant updates concerns proliferation metrics. The WHO now requires mitotic count to be reported per standardized area (mm^2), replacing the previously used high-power fields. ACC is graded using a two-tiered system: low-grade tumors show ≤20 mitoses per 10 mm^2, whereas high-grade tumors exceed this threshold. Although Ki-67 has strong prognostic value, it is not used as a formal grading parameter because it represents a continuous variable; however, a cutoff of 15% is commonly referenced for risk assessment, and recent studies suggest that a threshold of 10 mitoses per 10 mm^2 may provide improved prognostic performance [31,59,62]. The classification also refines the morphological categorization of ACC, adopting the term “subtype” to differentiate histological patterns from molecular variants [62]. In addition to conventional ACC, the recognized subtypes include oncocytic, myxoid, and sarcomatoid ACC. The oncocytic subtype, defined by >90% oncocytic cells with large,

eosinophilic granular cytoplasm and prominent nucleoli, requires specific diagnostic criteria, as Weiss parameters tend to overestimate malignancy in this setting; the Lin–Weiss–Bisceglia system is therefore preferred [31,59]. Myxoid ACC is characterized by variable extracellular myxoid matrix in which tumor cells form delicate trabeculae, cords, or microcysts; importantly, myxoid change alone is not indicative of malignancy [62]. Sarcomatoid ACC, the rarest subtype, shows mesenchymal differentiation within a carcinomatous adrenocortical component and requires immunohistochemical confirmation to distinguish it from primary adrenal sarcomas [59,62].

Among the diagnostic algorithms, the reticulin framework retains a central position. Disruption of the reticulin network must be accompanied by at least one additional parameter (necrosis, increased mitotic activity, or vascular invasion) to establish malignancy [62]. For pediatric ACC, adult algorithms are not appropriate; instead, the Wieneke/AFIP scoring system is required, although it suffers from incomplete sensitivity and specificity [62]. Finally, the 5th edition introduces refinements to the nomenclature of adrenal cortical nodular disease, moving away from the generic term “hyperplasia” in selected contexts in order to acknowledge the clonal or neoplastic nature of certain lesions, such as sporadic nodular adrenocortical disease [31,59]. In summary, the updated WHO framework integrates architectural, cytological, immunohistochemical, molecular, and proliferative features into a coherent and multiparametric system that enhances diagnostic accuracy and strengthens prognostic assessment in adrenocortical carcinoma.

3.3 Histopathological diagnosis and diagnostic markers of ACC

The histopathologic diagnosis of adrenocortical carcinoma (ACC) relies primarily on established scoring systems that evaluate morphological and proliferative features, complemented by immunohistochemical markers that confirm adrenocortical origin and help define malignant potential. The Weiss scoring system, first proposed in 1984, assesses nine histopathologic parameters: cytological features (nuclear atypia, mitotic count, atypical mitoses), architectural characteristics (diffuse architecture, clear cells, confluent necrosis), and invasion (capsular, venous, sinusoidal); a score ≥3 supports a diagnosis of carcinoma, whereas 0–2 is consistent with adenoma [50,59,61]. Although widely used, the Weiss system is susceptible to interobserver variability, prompting the development of refined versions.The modified or

simplified Weiss systems place greater emphasis on reproducible parameters, particularly mitotic rate and clear cell proportion, to enhance diagnostic consistency.

For oncocytic variants, which inherently fulfill several Weiss criteria, the Lin–Weiss–Bisceglia system was specifically developed, providing a tailored and more reliable framework to distinguish malignant from borderline lesions [31,47]. The reticulin algorithm provides a reproducible diagnostic approach for conventional, oncocytic, and myxoid ACCs by evaluating the reticulin framework with Gordon-Sweet silver staining. Malignancy is confirmed when structural alterations are accompanied by increased mitoses, necrosis, or vascular invasion [56]. The Helsinki score integrates mitotic count, tumor necrosis, and Ki-67 proliferation index measured in the most proliferative area, offering 100% sensitivity and 99.4% specificity for diagnosing metastatic ACC and predicting metastatic potential. Ki-67 and mitotic rate also correlate strongly with tumor aggressiveness and clinical outcomes [63]. Immunohistochemistry further supports diagnosis and prognostication: SF-1 reliably confirms adrenocortical origin with high specificity and sensitivity, Ki-67 helps differentiate ACC from adenoma and provides prognostic insights. Additional markers, including IGF-II, p53, β-catenin, calretinin, α-inhibin, Melan-A, and synaptophysin, contribute to diagnostic refinement, though with variable specificity [62,64,65]. Despite the robustness of these diagnostic systems, challenges persist in borderline cases, low-grade malignancies, pediatric tumors, and rare subtypes such as myxoid ACC. This underscores the need for an integrated, multiparametric approach that incorporates morphology, proliferative indices, and immunohistochemistry to achieve accurate diagnosis and reliable prognostic stratification [20,66].

3.4 Hormonal evaluation

A comprehensive hormonal evaluation is a cornerstone in the diagnostic workup of ACC, as biochemical evidence of autonomous steroid secretion not only confirms the adrenocortical origin of the tumor but also helps discriminate ACC from other adrenal or extra-adrenal conditions, such as pheochromocytoma or lymphoma [36,47]. Hormone assays frequently reveal a characteristic pattern of co-secretion,typically glucocorticoids, androgens, estrogens, mineralocorticoids, and various steroid precursors, making the hormonal profile highly suggestive of malignancy even before surgery [36,58,64,67]. Because 60–70% of ACCs present with biochemical hypersecretion and approximately half of patients experience clinical symptoms related to cortisol or androgen excess, biochemical testing is essential regardless of clinical

phenotype [47,58]. The pre-operative hormone pattern can also act as a biochemical "fingerprint," serving as an individualized marker for postoperative monitoring and early detection of recurrence [36,47,68]. As recommended by the ESMO–EURACAN guidelines, hormonal evaluation must systematically exclude pheochromocytoma through measurement of plasma-free or urinary-fractionated metanephrines, with additional assessment of methoxytyramine when available, given the potentially life-threatening intraoperative risks associated with unrecognized catecholamine excess [44,58]. In all suspected ACCs, an extensive panel assessing glucocorticoids, mineralocorticoids, sex steroids, and precursor steroids is advised, typically including basal cortisol, ACTH, DHEA-S, 17-hydroxyprogesterone, testosterone, androstenedione, estradiol, urinary free cortisol, and a standard 1-mg overnight dexamethasone suppression test to rule out hypercortisolism, even in the absence of overt Cushingoid features [36,61]. This evaluation is also essential to determine the need for pre-operative cortisol-lowering therapy in cases of severe hypercortisolism, as well as postoperative hydrocortisone replacement in cortisol-producing tumors [47,58,68]. In recent years, significant attention has been directed toward urine steroid metabolomics, which can detect a wide spectrum of steroid precursors and metabolites produced by dedifferentiated malignant cells, reflecting the "disorganized" or incomplete steroidogenesis typical of ACC [58,59,69]. These metabolomic signatures not only differentiate ACC from benign adrenocortical adenomas but also offer a promising tool for prognosis and recurrence monitoring [61,69]. ACCs rarely secrete a single steroid hormone; instead, they typically produce multiple active and inactive steroids simultaneously, a pattern that strongly favors malignancy, although rare cases of aldosterone- or estrogen-producing ACCs have been documented [64,67]. The growing recognition of how altered steroidogenesis affects tumor immunobiology, particularly the potential impact on response to immune checkpoint inhibitors, highlights the expanding clinical relevance of detailed hormonal profiling in ACC. [59]. Overall, hormonal assessment fulfills multiple essential roles: confirming tumor origin, estimating malignancy risk, guiding perioperative management, preventing surgical complications, identifying candidates for steroid-modulating therapy, and serving as a sensitive biomarker for long-term surveillance [44,47,61,68]

3.5 Radiological and morphological diagnosis (Imaging)

Imaging plays a central role in the evaluation and preoperative assessment of adrenocortical carcinoma (ACC), providing crucial information for distinguishing malignant from benign

adrenal lesions and guiding surgical planning. Computed tomography (CT) remains the first-line modality due to its high spatial resolution, ability to assess tumor size and morphology, and capacity to detect invasion into adjacent structures, including the inferior vena cava. Measurement of Hounsfield units (HU) on unenhanced CT is a key criterion, with ≤10 HU indicative of lipid-rich adenomas, while higher values warrant delayed contrast-enhanced CT; an absolute washout >50–60% typically suggests a benign lesion [44,48,58,61]. ACC generally presents as a large (>10 cm median diameter), heterogeneous mass with irregular margins, necrosis, hemorrhage, and sometimes calcifications, features consistently associated with malignancy [48,61,70]. Tumor size is one of the most powerful predictors, with specificity and sensitivity for malignancy increasing from 52% and 96% for lesions ≥4 cm to 80% and 90% for tumors ≥6 cm, and approaching near certainty for lesions >10 cm [68,70].

MRI provides complementary information, particularly for delineating the tumor from surrounding organs and for characterizing tissue composition. ACCs are typically isointense to hypointense on T1-weighted images, hyperintense on T2-weighted sequences, and exhibit heterogeneous signal loss on chemical shift imaging, with contrast-enhanced sequences showing progressive enhancement and slow washoutv[36,58,61]. Functional imaging with 18F-fluorodeoxyglucose positron emission tomography (FDG-PET) adds diagnostic value, as most ACCs demonstrate increased uptake, with an adrenal-to-liver maximum standardized uptake value (SUV) ratio >1.45. In a prospective study of 77 patients, FDG-PET achieved a sensitivity of 100% and specificity of 88% in distinguishing ACC from adenomas [36,61]. FDG-PET is particularly useful for staging and detection of metastatic disease, although sensitivity decreases for lesions <1 cm and false-positive uptake may occur in benign conditions or in the contralateral adrenal after mitotane therapy [47,68].

Molecular imaging with adrenal-specific tracers, such as [11C]metomidate (MTO) for PET and [123I]iodometomidate (IMTO) for SPECT, allows identification of adrenocortical origin by selectively binding CYP11B1 and CYP11B2 enzymes. MTO-PET demonstrates ~90% sensitivity and 96% specificity in differentiating adrenal from non-adrenal lesions, whereas IMTO-SPECT offers high specificity (86–100%) but variable sensitivity (38–83%), particularly in small or necrotic tumors. These tracers may also facilitate selection of patients for targeted radionuclide therapy [36,47,58,70].

Recent advances in quantitative imaging, including radiomics and machine learning applied to contrast-enhanced CT, have improved discrimination between benign and malignant lesions, with diagnostic accuracy reaching 82%, surpassing conventional radiologist interpretation [69]. Overall, a multimodal imaging strategy integrating anatomical, functional, and molecular

techniques is essential for accurate diagnosis, malignancy risk stratification, and optimal preoperative management of ACC [36,44,58,61,69,70].

3.6 ACC Staging

Tumor staging represents a fundamental tool for assessing prognosis in patients with cancer, and for adrenocortical carcinoma (ACC) the tumor–node–metastasis (TNM) classification proposed by the European Network for the Study of Adrenal Tumours (ENSAT) is the recommended system due to its superior prognostic performance compared to earlier classifications [36]. The ENSAT system defines Stage I and Stage II as tumors confined to the adrenal gland with diameters ≤5 cm or >5 cm, respectively, while Stage III encompasses infiltration of surrounding tissues, venous tumor thrombus in the renal vein or vena cava, or regional lymph node involvement; Stage IV is characterized by the presence of distant metastases [71]. This staging framework has been endorsed by the Union for International Cancer Control (UICC) and the WHO, and its use is recommended in major clinical guidelines, which specify that staging should be based on comprehensive imaging, including at minimum CT of the chest, abdomen, and pelvis, or alternatively FDG-PET/CT with diagnostic CT acquisition [44]. ENSAT staging was derived from a large cohort of 1065 patients and is widely accepted worldwide, sharing key features with the American Joint Committee on Cancer classification [68,72]. Importantly, ENSAT staging has demonstrated strong prognostic relevance, with survival decreasing significantly across stages and representing one of the most powerful predictors of outcome in ACC. In clinical practice, ENSAT staging directly influences therapeutic strategies, including the decision to administer adjuvant mitotane therapy, the extent of surgical resection, and the intensity of follow-up, underscoring its central role in the multidisciplinary management of ACC. Although ENSAT more accurately predicts clinical outcomes than previous TNM models, recent evidence suggests that certain features, such as severe vena cava invasion or specific lymph node patterns, may behave biologically like Stage IV disease, indicating that further refinement of the system may still be necessary [67]. Beyond anatomical staging, ENSAT guidelines emphasize the importance of proliferative activity, recommending a Ki-67 cutoff of 10% to differentiate low- and intermediate-grade tumors in completely resected Stage I–II disease, and stressing that Ki-67 assessment should be performed in hotspot areas after thorough specimen review and preferably using digital image analysis. To integrate multiple prognostic variables, the ENSAT group has also proposed the S-GRAS score, which combines stage (S),

tumor grade based on Ki-67 (G), resection margin status (R), age at diagnosis (A), and the presence of symptoms (S), offering a practical and multidimensional stratification tool [59].

ENSAT stage	T	N	M
I	1	0	0
II	2	0	0
III	1, 2	1	0
	3, 4	0, 1	0
IV	1–4	0, 1	1

Table 1. Staging system for ACCs ENSAT, European Network for the Study of Adrenal Tumors. Tumors are classified as follows: T1, tumor ≤5 cm; T2, tumor >5 cm; T3, tumor infiltration into surrounding (fat) tissue; T4, tumor invasion into adjacent organs or venous tumor thrombus in vena cava or renal vein; N0, no spread into nearby lymph nodes; N1, positive lymph node(s); M0, no distant metastasis; M1, presence of distant metastasis. 68.

3.7 Prognosis and clinical relevance

The prognosis for ACC is generally poor but highly heterogeneous, underscoring the need for reliable prognostic tools to guide follow-up, adjuvant treatment, and patient counseling [47,73]. Prognostic classifications fall into two major categories: clinical and molecular. The clinical classification is based primarily on the TNM-ENSAT staging system, which stratifies patients according to tumor extent and remains the backbone of therapeutic decision-making, although survival varies markedly even within the same stage, with reported 5-year survival rates ranging from 13% to 80% across different cohorts [20,36,39,48,73,74]. This variability reflects the biological heterogeneity of ACC: while a minority of patients with metastatic disease may survive over a decade, more than 20% of those with early-stage tumors (I–III) die within three years [75,76]. Surgery represents the only curative treatment, yet recurrence occurs in 60–70% of patients

after apparently radical resection, and survival decreases dramatically from 50–82% in localized disease to 0–28% in metastatic cases [51,77–79]. The completeness of resection is a key determinant of outcome, with 5-year survival falling from 49–65% after R0 resections to 21% after R1 and 10% after R2. Histopathological markers further refine risk assessment, with Ki67 emerging as the single strongest predictor of prognosis, outperforming age, tumor size, and venous invasion (Felix Beuschlein et al.; Michael R. Clay et al.). Additional adverse clinical factors include advanced age, cortisol hypersecretion, associated with systemic immunosuppression and more aggressive disease, high mitotic activity, and the presence of multiple metastases. To overcome the limitations of single prognostic variables, integrated classification systems have been developed. The earlier GRAS classification demonstrated the prognostic value of the GRAS components, that is, grading (G), resection status (R), age (A), and tumour- or hormone-related symptoms (S) [75]. Building on this, the more comprehensive S-GRAS system incorporates these same GRAS elements together with ENSAT stage and the Ki67 index, allowing a more precise stratification of patient risk by combining symptoms, tumor stage, surgical margins, age, and proliferative activity into a single cumulative prognostic score. This approach has gained considerable attention in the literature: [75]. Y S Elhassan et al. first showed that S-GRAS outperforms ENSAT stage alone in predicting overall survival; [77]Anne Jouinot et al**.** subsequently used S-GRAS to stratify patients in a large multicenter analysis, confirming its superior ability to predict both recurrence and mortality; [78] Laura-Sophie Landwehr et al. applied S-GRAS to refine postoperative follow-up strategies; and [80]Marta Araujo-Castro et al. provided external validation demonstrating a clear gradient of 5-year survival probabilities ranging from approximately 70–75% in low S-GRAS classes to below 10% in the highest-risk groups. In parallel with clinical systems, molecular classifications based on recurrent genomic alterations, such as IGF2 overexpression, TP53 mutations, and CTNNB1 activation, have identified biologically distinct tumor subtypes associated with increased aggressiveness and reduced disease-free survival [73,81,82]. Altogether, ACC remains a highly lethal malignancy with a median overall survival of 3-4 years, and accurate prognostic evaluation now requires an integrated approach combining clinical staging, surgical and pathological factors, molecular insights, and robust multi-parameter tools such as S-GRAS, which has emerged as one of the most reliable frameworks for guiding risk stratification, surveillance, and therapeutic decision-making [83–85].

4 ACC therapies

4.1 Localized adrenocortical carcinoma:

4.1.1 Surgery

Surgical resection remains the only potentially curative treatment for adrenocortical carcinoma (ACC), and all patients with adrenal tumors suspected of malignancy should be offered surgery when the tumor is resectable and distant metastases are absent [39,86–89]. A complete R0 resection is essential, and must follow strict oncological principles, including en bloc removal of the adrenal gland with periadrenal fat and preservation of an intact capsule to prevent local spread [33,61,86,87].

In locally advanced tumors, achieving negative margins may require resection of adjacent organs such as the ipsilateral kidney, liver, spleen, pancreas, diaphragm, or stomach, depending on the extent of invasion [39,61,88,89]. When tumor thrombus extends into the renal vein or inferior vena cava, complete resection may necessitate venovenous or cardiopulmonary bypass procedures [88,89].

Open adrenalectomy (OA) is widely regarded as the standard surgical approach for ACC, particularly in infiltrating tumors, those with suspected lymph node involvement, or larger lesions where the risk of tumor spillage is higher [61,86,87,89]. Minimally invasive techniques such as laparoscopic adrenalectomy may be considered only for small (<5–6 cm), non-infiltrating tumors in carefully selected cases and when performed by experienced surgeons [61,86,89]. Although some studies suggest comparable oncologic outcomes between minimally invasive and open surgery for tumors under 10 cm, most experts continue to favor open surgery due to the risk of tumor rupture and peritoneal carcinomatosis [86,87,89].

Lymph node dissection (LND) is important for accurate staging and may offer therapeutic benefit in localized ACC. Removal of periadrenal, perirenal, and renal hilar lymph nodes, and any suspicious nodes, is recommended [33,61,86]. LND appears to reduce local recurrence and may improve overall survival in early-stage disease, although its benefit is less clear in advanced or metastatic ACC [33,86].

Preoperative hormonal evaluation is essential to detect cortisol-producing tumors and to plan for postoperative adrenal insufficiency when necessary [39]. Even after apparently complete resection, recurrence rates can reach 60–80%, justifying routine consideration of adjuvant therapy [89]. Proper preoperative imaging with abdominal MRI and thoracic CT, supplemented

by PET/CT or bone scintigraphy when indicated, is crucial to assess local extension and rule out metastases [88].

4.1.2 ACC Adjuvant therapy

The need for adjuvant therapy in adrenocortical carcinoma (ACC) is determined by the high risk of recurrence after surgery, driven primarily by tumor stage, completeness of resection, and proliferative rate, with more than half of patients relapsing even after seemingly curative surgery, often with distant metastases due to occult micrometastases present at diagnosis; local recurrence rates remain substantial (approximately 19–34% depending on stage), and this aggressive behavior provides the rationale for employing adjuvant strategies, which include mitotane and, in those at particularly high risk of local recurrence, irradiation of the tumor bed. [33,39,44,47,61,88,89].

Mitotane treatment

Mitotane, a derivative of DDT (dichlorodiphenyltrichloroethane) with adrenolytic, cytotoxic, and steroidogenesis-inhibiting properties, mediated through inhibition of CYP11A1 and CYP11B1 (key enzymes in steroid hormone biosynthesis), SOAT1 (sterol O-acyltransferase 1) blockade, mitochondrial dysfunction, endoplasmic reticulum (ER) stress, and induction of CYP3A4 (cytochrome P450 3A4), remains the only approved systemic therapy for adrenocortical carcinoma (ACC) and the historical agent of choice in the adjuvant setting, although its role continues to be debated. [33,39,47,88,90,91]

Evidence from large retrospective cohorts, including the seminal Terzolo study [92], as well as meta-analyses, indicates that adjuvant mitotane can significantly prolong recurrence-free survival (RFS) and, in some analyses, overall survival (OS) after macroscopically complete resection, particularly in patients at high risk of relapse, such as those with stage III disease, R1–Rx (microscopically/macroscopically positive or uncertain resection margins), large or high-grade tumors, or Ki-67 >10% (proliferation index) [33,39,44,47,88]. Conversely, data from the randomized ADIUVO (Adjuvant Mitotane in Low-Intermediate Risk ACC) trial showed no benefit in low–intermediate-risk patients (R0, microscopically complete resection; Ki-67 <10%), supporting the recommendation that mitotane should not be routinely used in this subgroup, where treatment decisions should be individualized [33,39,44,47,88].

When indicated, mitotane should be started as soon as clinically feasible after surgery, with careful therapeutic drug monitoring due to its narrow therapeutic window, highly variable

pharmacokinetics, long half-life, and strong correlation between plasma levels and both efficacy and toxicity [33,39,61,88]. Clinical benefit is most consistently associated with mitotanemia ≥14 mg/L, and possibly >8 mg/L, while toxicity, especially neurological, becomes more frequent at levels >20 mg/L, prompting clinicians to titrate the drug to the highest tolerable concentration [33,39,61,88]. Standard dosing strategies include either high- or low-dose escalation regimens, which appear similarly effective in achieving therapeutic levels, although reaching target concentrations may require months of monitoring [61].

Mitotane's adverse-effect profile is substantial, encompassing gastrointestinal and neurological symptoms, hepatotoxicity, hypercholesterolemia, bone-marrow suppression, and multiple endocrinopathies, most notably universal adrenal insufficiency requiring high-dose glucocorticoid replacement, and sometimes mineralocorticoid, because of its potent adrenolytic effects [33,39,61,88,90,91]. Drug–drug interactions are common due to CYP3A4 induction, necessitating close endocrinological follow-up [33,88,91].

Current ESE–ENSAT (European Society for Endocrinology–European Network for the Study of Adrenal Tumors) and ESMO–EURACAN (European Society for Medical Oncology–European Reference Network for Rare Adult Solid Cancers) guidelines recommend adjuvant mitotane for high-risk patients (stage III, R1–Rx, Ki-67 >10%), while advising individualized discussion for low/moderate-risk cases; therapy is generally suggested for at least 2 years but not beyond 5 years, as most recurrences occur early and late relapses are uncommon [44,88,93]. In very high-risk patients (e.g., Ki-67 ≥20%, extensive vascular invasion, vena cava thrombus), some authors consider adding platinum-based chemotherapy to mitotane, although benefit remains unproven and is under investigation in the ongoing ADIUVO-2 trial, which will clarify whether combining cisplatin/etoposide with mitotane provides superior outcomes [39,47].

Adjuvant radiotherapy

Adjuvant external beam radiotherapy (RT) to the tumor bed is considered a strategy to reduce the risk of local recurrence in adrenocortical carcinoma (ACC), although its use remains debated due to the historical perception of ACC as a radioresistant tumor [39,47,61]. Current expert recommendations converge on offering adjuvant RT primarily to patients at high risk of local relapse, including those with R1 or Rx margins, capsular rupture, stage III disease, locally advanced tumors, or features of biological aggressiveness such as Ki-67 >20%, and to those resected in non-expert centers or through suboptimal surgical approaches [33,36,89,93]. Although RT does not prevent distant metastases and therefore has limited impact on overall survival (OS), growing evidence indicates that modern RT techniques can substantially reduce local

recurrence rates, particularly in patients with positive or uncertain margins. For this reason, concomitant mitotane therapy is often considered in high-risk patients, despite the increased toxicity associated with combined treatment [44]. Case-control studies from the German ACC group and the University of Michigan demonstrated markedly lower local recurrence in irradiated patients compared to matched patients, 14% versus 79% and 5% versus 60% respectively, although without significant differences in recurrence-free survival (RFS) or OS, likely due to limited power; in contrast, a larger subsequent series from the Michigan group, including 78 patients, reported improvements not only in local control but also in RFS and OS in those receiving adjuvant radiotherapy [47]. Nevertheless, the absence of prospective trials mandates cautious interpretation, and practice varies across institutions (potential referral and selection bias) [47]. When administered, adjuvant radiotherapy RT should begin within 3 months after surgery and deliver a total dose of 50 - 60 Gy to the tumor bed with standard fractionation, in 1.8–2.0 Gy fractions, 5 days per week for 5–6 weeks, using CT-based planning and modern high-precision techniques to optimize outcomes and minimize toxicity. [89,93]. Combination with mitotane is often considered in high-risk patients, though at the expense of increased toxicity [44]. Overall, while not recommended routinely for stage I–II R0 disease, adjuvant RT represents a valuable option for selected high-risk cases in experienced multidisciplinary centers). Although RT consistently reduces local recurrence, it does not prevent distant metastases and therefore has limited impact on OS. For this reason, concomitant mitotane therapy is often considered in high-risk patients, despite the increased toxicity associated with combined treatment.

Only patients with histologically proven ACC who have a very low risk of recurrence, such as those with R0 resection, tumor <8 cm, absence of microscopic vascular invasion, and Ki-67 <10%, may be safely observed without adjuvant therapy. In these cases, close follow-up is essential in the early stage, with imaging every 3 months during the first 2 years; the Fassnacht group also performs PET in addition to CT at 6 and 12 months. Because the risk of relapse persists beyond this interval, long-term surveillance for an additional 10 years is recommended [89]. In all patients with recurrent disease, repeat surgery should be considered when complete resection is feasible and the disease-free interval exceeds 4 months; in such cases, adjuvant therapy becomes mandatory. For locoregional recurrence without metastases, adjuvant radiotherapy to the tumor bed is advised, and in patients relapsing despite mitotane, combination therapy with additional agents such as streptozotocin may be considered; when surgery is not possible, management follows protocols for metastatic disease [89]. After adjuvant

radiotherapy, enhanced surveillance is required because most local relapses occur early, with cross-sectional imaging every 3–6 months for at least 2 years and careful assessment of RT-treated fields to differentiate post-treatment changes from true recurrence. Finally, although the role of adjuvant cytotoxic chemotherapy remains uncertain, some centers employ regimens such as cisplatin plus etoposide in patients with very high recurrence risk, a strategy currently under investigation in a randomized clinical trial (NCT03583710) [44].

4.2 Therapies for metastatic ACC

The management of metastatic ACC remains challenging due to the limited efficacy of systemic therapies and the frequent inability to achieve complete surgical resection. Surgical intervention is generally considered only when all known disease sites can be completely removed, particularly in cases of oligometastatic disease to the liver or lungs, or when the disease-free interval from prior surgery exceeds 9–12 months; however, for patients with widespread or rapidly progressive metastases, surgery is rarely feasible [33,94,95]. Surgical resection can improve survival in selected patients, particularly those with a limited number of metastatic organs, slow progression, or severe hormone excess that cannot be otherwise controlled [33].

In patients who are not surgical candidates, mitotane remains the backbone of therapy. It is the only drug approved by the FDA and EMA for ACC, and it may be used as monotherapy in patients with low tumor burden or indolent disease, though objective response rates are modest (13–35%) [47,93]. Mitotane is a potent inducer of CYP3A4, which can significantly reduce plasma levels of concomitant cytotoxic drugs such as etoposide, an effect that must be considered when planning combination therapy [93].

For patients with aggressive disease or those progressing on mitotane monotherapy, combination therapy with cytotoxic chemotherapy is recommended. The FIRM-ACT trial established etoposide, doxorubicin, and cisplatin plus mitotane (EDP-M) as the first-line standard of care, demonstrating superior objective response rates (23–49%) and progression-free survival (5.0 months vs. 2.1 months) compared with mitotane plus streptozocin, although overall survival was not significantly different, likely due to the trial's crossover design [44,61,86–88,90]. In patients unsuitable for full EDP-M, modified regimens such as mitotane plus cisplatin, or etoposide plus cisplatin, may be considered depending on organ function and performance status [93,95]. The administration of EDP-M carries significant toxicity. Common adverse events include asthenia, nausea, vomiting, reversible myelosuppression, liver toxicity (etoposide), cardiotoxicity (doxorubicin), nephrotoxicity, ototoxicity, and peripheral neuropathy [93,95]. Dose

modifications or substitutions (e.g., carboplatin for cisplatin, omission of doxorubicin) may be required in patients with compromised organ function or poor performance status.

After progression on first-line therapy, second- and third-line options remain limited. The most studied regimens include streptozocin plus mitotane and gemcitabine plus capecitabine (with or without mitotane), as well as single agents such as temozolomide, trofosfamide, and thalidomide; however, objective response rates are generally below 10–20%, and progression-free survival rarely exceeds 4–5 months [33,44,47,88]. Mitotane is often continued during second-line therapy, though the optimal timing of discontinuation remains undefined.

Local therapies, including radiotherapy, radiofrequency ablation, cryoablation, microwave ablation, and chemoembolization, may provide symptom palliation and local disease control, especially in patients with limited progressive lesions or oligometastatic disease [44,95]. Integrated palliative care, including fertility counseling for reproductive-age patients and anti-resorptive treatment for bone metastases, is recommended for all patients with advanced ACC.

Overall, the management of metastatic ACC requires an individualized approach balancing disease burden, progression kinetics, and patient performance status against treatment efficacy and toxicity. While EDP-M represents the only first-line regimen with randomized evidence supporting its use, prognosis remains poor, and outcomes after second-line therapy are limited, highlighting the urgent need for novel therapeutic strategies [47,61,86–88].

4.2.1 Molecularly targeted therapy

Molecularly targeted approaches remain a logical strategy for adrenocortical carcinoma (ACC), but their clinical impact has been modest to date because ACC is molecularly heterogeneous and lacks a single, consistently actionable driver alteration [39,86]. Early clinical efforts concentrated on receptor-tyrosine-kinase (RTK) inhibitors: EGFR blockade with agents such as gefitinib or combinations of erlotinib and gemcitabine yielded very low objective response rates, and anti-angiogenic multitarget TKIs (for example sunitinib) produced only occasional, short-lived disease control in small phase II series [88,96].

Similarly, anti-angiogenic agents, including the VEGF-targeted tyrosine kinase inhibitor sunitinib, produced only modest antitumor activity in phase II studies, with limited durability of disease control [33,44]. Because IGF2 overexpression is a near-ubiquitous hallmark of ACC (reported in ~ 80% or more of cases) and signals through IGF1R and the insulin receptor to engage MAPK and PI3K-AKT-mTOR cascades that drive proliferation and survival, the IGF axis was prioritized for therapeutic targeting; preclinical models showed pathway dependence

and early clinical studies of anti-IGF1R antibodies or dual IGF1R/IR inhibitors produced disease stabilizations in subsets of patients, but large randomized trials (e.g., linsitinib) failed to improve progression-free or overall survival in unselected populations [87,88,90,91,96].

Beyond RTKs and the IGF axis, several additional pathways and targets have emerged as relevant to ACC biology and are under active investigation. The Wnt/β-catenin pathway, frequently altered in ACC and implicated in tumor initiation and progression, represents an attractive but challenging target because of pathway complexity and lack of clinically mature inhibitors; its importance in ACC oncogenesis is well documented in recent genomic and review studies [87,91].

The PI3K–AKT–mTOR axis, downstream of multiple RTKs and of IGF signaling, is commonly activated in ACC and provides a rationale for mTOR and PI3K inhibitors, particularly in combination regimens designed to prevent compensatory feedback loops [91,96].

Fibroblast growth factor receptors (FGFRs) and other non-canonical RTKs (PDGFR, FGFR family members) have also been identified as potential targets in molecular profiling studies, and pan-FGFR or selective FGFR inhibitors warrant evaluation in genomically selected subsets [96,97].

Novel cell-cycle and kinase vulnerabilities have likewise been proposed: PLK1 (polo-like kinase 1) is overexpressed in many ACCs and PLK1 inhibitors have shown preclinical activity, supporting early translational work on PLK1 inhibitors for genetically selected tumors [98].

Similarly, inhibition of focal adhesion kinase (FAK) and Src family kinases, for example with defactinib, has demonstrated synergistic anti-tumor activity with mitotane in preclinical ACC models, suggesting that targeting tumor-stroma and adhesion signalling could potentiate current systemic therapy [99].

Epigenetic alterations (including TERT regulation and DNA methylation changes) and other cell-cycle regulators have been highlighted by multi-omics studies as additional actionable nodes that may be exploitable with targeted or synthetic-lethality approaches [91].

These insights have produced two clear translational imperatives: first, single-agent targeted therapy rarely yields durable responses in an unselected ACC population because of pathway redundancy and intra-tumoural heterogeneity; second, rational combination strategies (for example combining IGF-axis or RTK inhibitors with mTOR/PI3K inhibitors, FAK/mitotane combinations, or agents targeting cell-cycle kinases) and biomarker-driven patient selection are required to convert biological vulnerability into clinically meaningful benefit [91,96,99]. Consequently, contemporary development in ACC is moving toward multi-modal, genomics-

informed trials that pair targeted agents with mitotane, cytotoxic chemotherapy or other targeted drugs, and that stratify patients by molecular subtype to maximize the chance of response [39,86]. In short, molecular targeting in ACC has validated multiple biologic vulnerabilities (IGF axis, Wnt/β-catenin, PI3K–mTOR, FGFR/PDGFR, PLK1, FAK/Src and epigenetic regulators), but translating these into practice requires combination regimens, predictive biomarkers and carefully designed trials that address compensatory signalling and tumour heterogeneity [91,96,98].

4.2.2 ACC tumor microenvironment

The tumor microenvironment (TME) of ACC is increasingly recognized as a central determinant of tumor progression and therapeutic resistance, defined by marked cellular heterogeneity, profound immunosuppression, and complex metabolic and endocrine interactions. ACC has long been described as an "immune-cold" or immune-depleted malignancy, exhibiting scarce lymphocytic infiltration and limited activation of anti-tumor immunity features largely attributed to dysregulated intratumoral glucocorticoid production and heightened glucocorticoid receptor (GR) signaling, which suppress both innate and adaptive immune responses [100–103].

High-resolution single-nucleus transcriptomic analyses have mapped the intricate architecture of the ACC TME, revealing mixtures of steroidogenic tumor cells, stromal components, and diverse immune populations whose relative abundance and functional states underpin clinically relevant heterogeneity [103,104]. Importantly, integrative transcriptomic and immunogenomic studies demonstrate that ACC is not uniformly immune-cold: distinct immune microenvironment subtypes exist, most prominently the low-infiltrated "Immunity-L" subtype, representing the classical immune-cold phenotype, and the more inflamed "Immunity-H" subtype, characterized by increased leukocyte infiltration, enhanced antigen-presentation pathways, and higher expression of immune checkpoint molecules [104–106]. These immune subtypes possess strong prognostic significance and correlate with differential likelihood of responding to immunotherapy. Additional TME-shaping forces, including hypoxia and pyroptosis-related gene programs, contribute further layers of heterogeneity, and their associated molecular signatures can refine prognostic stratification and illuminate mechanisms of immune exclusion [85,107]. Collectively, the emerging evidence indicates that overcoming ACC's dominant immune-cold phenotype will require therapeutic strategies capable of modulating steroidogenic signaling, reprogramming suppressive stromal and myeloid

compartments identified by single-cell profiling, and leveraging molecular and immune subtyping, alongside hypoxia- and pyroptosis-related signatures, to optimize and personalize immunotherapeutic interventions [101–104].

4.2.3 ACC Immunotherapy

Immunotherapies, encompassing a diverse spectrum of immune-stimulating and immune-modulating anticancer strategies, have demonstrated meaningful clinical benefit across a wide range of solid and hematologic malignancies. Their broad applicability has naturally prompted growing interest in evaluating these agents in rare tumors such as ACC. In recent years, multiple clinical trials have explored the therapeutic potential of immunotherapy in ACC, and many more are ongoing or planned, with immune checkpoint inhibitors such as pembrolizumab, nivolumab, and avelumab representing the most frequently investigated modalities [101,108]. Immunotherapy has therefore emerged as a promising yet challenging avenue for adrenocortical carcinoma (ACC), a rare and aggressive malignancy traditionally associated with limited treatment options and poor prognosis. Despite the enthusiasm generated by the success of immune checkpoint inhibitors (ICIs) in other solid tumors, clinical evidence indicates that ACC displays only modest and heterogeneous responses to agents targeting PD-1, PD-L1, or CTLA-4 [80,108–110]. Early trials evaluating PD-1 blockade with pembrolizumab demonstrated partial responses and durable disease stabilization in a subset of heavily pretreated patients, although overall efficacy remained modest [80,111]. Combination strategies, such as nivolumab plus ipilimumab, have shown somewhat improved activity, supporting the idea that dual checkpoint inhibition may mitigate intrinsic resistance mechanisms [108,112]. Nevertheless, the immunologically “cold” phenotype of ACC, marked by low tumor mutational burden, scarce T-cell infiltration, and the immunosuppressive influence of glucocorticoid excess, presents substantial barriers to effective antitumor immunity [101,108,113]. Recent studies emphasize the need to integrate genomic and molecular insights to refine patient selection and identify predictive biomarkers, including mismatch repair deficiency, steroidogenic patterns, and immune-inhibitory ligand expression [80,91,108]. Moreover, elucidating mechanisms of primary and acquired resistance, such as upregulation of alternative immune checkpoints, impaired antigen presentation, and metabolically hostile tumor microenvironments, may guide the development of rational combination regimens [80,114]. Although ICIs are generally manageable in terms of toxicity, immune-related adverse events remain a relevant clinical concern,

particularly in endocrine malignancies where baseline hormonal dysregulation is common [115,116]. Overall, current evidence supports a cautiously expanding role for immunotherapy in ACC, underscoring the importance of multimodal strategies that integrate ICIs with targeted agents, hormonal modulation, or microenvironment-directed therapies to enhance clinical efficacy [108,110,113].

5 Preclinical models

Current preclinical models of ACC encompass a broad range of systems, including traditional 2D cell lines, advanced 3D culture platforms, patient-derived models, and in-vivo mouse approaches, that together capture complementary aspects of tumor biology. The steroidogenic NCI-H295R line remains the most widely adopted in-vitro model, preserving adrenal hormone production and key molecular features of ACC, while lines such as MUC-1, HAC15, CU-ACC1, and CU-ACC2 offer additional biological diversity [117–119]. In contrast, the historically used SW-13 line is now considered of questionable adrenocortical origin and is increasingly avoided due to its limited relevance [117,119]. Although valuable for mechanistic studies, 2D systems fail to replicate the tumor's three-dimensional architecture, stromal context, and gradient-dependent behavior.

To address these limitations, several 3D models have been developed using established ACC lines and patient-derived materials. Spheroids and organoids generated from NCI-H295R, MUC-1, and HAC15 better preserve spatial organization, functional steroidogenesis, and more physiological drug-response patterns [118,120,121]. Even more advanced are biomimetic 3D platforms integrating collagen I matrices and functional biosensors for matrix metalloproteinase activity, which enable the study of invasion, extracellular matrix remodeling, and treatment resistance in controlled microenvironments [120,122]. These models provide a bridge between simplified monolayer cultures and the complex structure of human tumors.

In vivo, patient-derived xenografts (PDXs) offer highly relevant systems that maintain the architectural and genomic heterogeneity of primary tumors. Newly established models such as CU-ACC1 and CU-ACC2, originating from perinephric and hepatic metastases and carrying clinically relevant mutations including CTNNB1, TP53, and MSH2 loss, have demonstrated faithful reproduction of tumor histology, gene expression programs, and hormone-secreting capabilities when engrafted in immunodeficient mice [117,118]. Pediatric PDX models such as SJ-

ACC3 further expand the diversity of available systems [123]. Additional xenograft models, including the MUC-1 xenograft, have been shown to recapitulate the high vascularization, SF-1 positivity, and drug-resistance patterns observed in the corresponding patients, particularly resistance to the EDP-M regimen used clinically [117,119,124]. More recently, humanized mouse models, such as a CU-ACC2-based platform incorporating functional human immune components, have begun to offer opportunities to study immune-oncology approaches, including checkpoint inhibition, which cannot be adequately assessed in standard immunodeficient PDX systems [124].

Together, the currently available preclinical ACC models, ranging from established cell lines to sophisticated 3D constructs, patient-derived organoids, xenografts, and emerging humanized mouse systems, form a complementary and expanding toolkit for dissecting ACC biology. While no single model fully captures the tumor's molecular, endocrine, and microenvironmental complexity, their combined use provides the most comprehensive foundation to date for mechanistic studies and preclinical therapeutic development [117,119,123].

Purpose of the study

Adrenocortical carcinoma (ACC) is a rare malignancy, with an estimated incidence of approximately 0.7 cases per million inhabitants in Western countries, and it meets the criteria for rare cancers according to both the U.S. Orphan Drug Act and the RARECARE definition adopted in Europe. The ACC is associated with pronounced biological, molecular, and histological heterogeneity, as well as with highly variable clinical behavior and responses to therapy. This heterogeneity, along with the low incidence, represents a major obstacle to the comprehensive understanding of its biology and natural history. Therapeutic responses are often evaluated in individual cases or small, heterogeneous cohorts, limiting the possibility of drawing robust conclusions regarding prognosis and treatment efficacy. Consequently, the biological variability and clinical course of ACC remain only partially characterized.

Within this context, the primary objective of this PhD thesis was to achieve an in-depth characterization of a primary ACC and its metastatic lesions. To this end, integrated genomic, immunohistochemical, and spatial proteomic analyses were performed with the aim of identifying key genetic alterations, defining the main biological pathways involved in ACC pathogenesis and metastasis, and preserving information on the spatial organization of protein expression within the tumor microenvironment. Particular emphasis was placed on molecular determinants potentially associated with tumor aggressiveness and therapeutic response.

As a second objective, this study aimed to develop and establish patient-derived experimental models both *in vitro* and *in vivo*, directly derived from the primary tumor and the secondary lesion, that faithfully recapitulate the biological and molecular features of the original malignancy. Patient-derived *in vitro* models were generated through the isolation and stabilization of primary tumor cells and the optimization of culture conditions to ensure long-term viability and proliferative capacity. In parallel, *in vivo* models were established using xenograft-based approaches, including patient-derived xenografts (PDX) and cell-derived xenografts (CDX). Once established, these *in vitro* and *in vivo* models were extensively characterized through morphological, functional, and immunohistochemical analyses to confirm the resemblance of the original genetic background and tumor phenotype, with particular attention to ACC-specific markers and proteins involved in cell proliferation and tumor progression.

Finally, the development of these preclinical models was conceived as a strategic platform for translational research, providing the basis for the generation and functional testing of chimeric

antigen receptor (CAR) T cells. In this framework, the models were intended to support the exploration of innovative immunotherapeutic strategies for ACC and to facilitate the translation of experimental findings toward personalized therapeutic approaches.

Collectively, these objectives were directed toward the generation of robust and representative patient-derived *in vitro* and *in vivo* models of ACC, aimed at advancing the understanding of metastatic ACC biology and supporting translational and personalized therapeutic strategies, including preclinical pharmacological and cell-based immunotherapy evaluations.

Materials and Methods

Ethics Statement

The study was approved by the Ethics Committee of S. Andrea Hospital, Rome, Italy, and the patient provided informed consent for the collection and use of biological samples The xenograft procedures were authorized by the Italian Ministry of Health (no. 67/2022-PR).

Sample collection and processing

Blood and tumor samples were retrieved intraoperatively.

Tumor tissues were sampled within 5 minutes of surgical resection. To maintain sterility and ensure sample quality, representative sections of primary and metastatic tumors were selected, while necrotic or electrocoagulated areas were carefully removed with a sterile scalpel. Xenografts and murine thoracic and abdominal organ blocks were collected immediately after euthanasia. The samples were then washed in sterile phosphate buffered saline (PBS) supplemented with antibiotics and then stored in: 10% buffered formalin for immunohistochemistry, IHC); liquid nitrogen, for genetic analysis; high-glucose DMEM (Dulbecco's Modified Eagle Medium) with penicillin, streptomycin and fungizone for cell cultures and xenotransplantation; 2% glutaraldehyde in PBS at 4 °C for transmission electron microscopy, TEM.

All samples were taken in macroscopically well-preserved areas. Maximum sample thickness was 0.5 cm, while TEM samples were reduced to ~3×3 mm pieces before fixation.

Genetic characterization

The genetic characterization included two key analyses: 1) detection of mutations and copy number vatiations (CNV) across a 81-gene panel through next-generation sequencing, which identifies changes in genes implicated in cancer; 2) assessment of microsatellite instability (MSI), which indicates a defect in the DNA mismatch repair (MMR) system, normally responsible for correcting post-replicative base-pairing errors;

Next-Generation Sequencing (NGS) and Comparative Genomic Hybridization – Single Nucleotide Polymorphism array (CGH-SNP)

Genomic DNAs were extracted with standard procedures from peripheral blood, considered germline reference DNA, (gDNA), skin, liquid nitrogen-frozen individual samples of primary tumor (p-tDNA) and a single hepatic metastasis (m-tDNA). Targeted NGS was performed using a proprietary custom-built gene panel (total target region = 0.287 Mb) covering the coding exons and flanking intronic regions of 81 genes implicated in cancer syndromes (Table 2). Targeted enrichment was conducted using the QIAseq FX DNA Library Kit (Qiagen), xGen Custom Hybridization Capture Panels and xGen Hybridization Capture Core Reagents (Integrated DNA Technologies Inc, IDT). Massive parallel sequencing and variant calling were executed on an Illumina MiSeq platform (average coverage >500x) using Sophia DDM software (Sophia Genetics), that ensured 99.48% sensitivity and 99.99% specificity. Relevant variants were confirmed with Sanger sequencing. Variant interpretation followed the ACMG [125] and the AMP/ASCO/CAP guidelines [126] and was cross-referenced with the ClinVar, COSMIC, gnomAD v4.1.0 and UK Biobank population frequency datasets. In parallel, to investigate chromosomal imbalances and allelic alterations such as copy-neutral losses of heterozygosity (CNNLOHs), high-resolution structural profiling was performed using a custom-designed comparative genomic hybridization–single nucleotide polymorphism (CGH–SNP) array.

The array, based on the Agilent SurePrint G3 8×60K platform, was scanned using the Agilent SureScan Dx system. The custom design included three key components: a dense tiling of CGH probes covering the exonic regions of the 81 NGS-targeted genes, allowing high-resolution detection of focal copy number variations; a concentrated set of SNP probes within these genes and across the entire chromosome 11, enabling allelic discrimination and assessment of losses of heterozygosity (LOHs) or CNNLOHs in this genomically-relevant chromosome; and a genome-wide CGH backbone with evenly-spaced probes across all chromosomes to detect large-scale chromosomal gains and losses.

This dual-resolution design enabled integrated detection of both focal and broad CNVs, along with allelic imbalances and uniparental disomies, providing a comprehensive overview of genome architecture in the analyzed primary and metastatic tumor samples.

Tumor type/syndrome	Test level	Genes
ENDOCRINE		
Pituitary adenoma / Familial acromegaly	I	*AIP, MEN1, CDKN1B*
	II	*CDKN1A, CDKN2B, CDKN2C, PRKAR1A, SDHA, SDHAF2, SDHB, SDHC, SDHD*
Adrenal carcinoma	I	*TP53, MLH1, MSH2, EPCAM, MSH6, PMS2*
	II	*PRKAR1A, MEN1, APC, NF1, FLCN*
Medullary thyroid carcinoma, Multiple endocrine neoplasia type 2	I	*RET*
	II	*ESR2*
Carney complex		*PRKAR1A, PRKACA*
Pheochromocytoma / Paraganglioma	I	*FH, MAX, NF1, RET*✕*, SDHA, SDHAF2, SDHB, SDHC, SDHD, TMEM127, VHL, BRK1*
	II	*DNMT3A, EGLN1, EGLN2, EPAS1, MDH2, MEN1, SLC25A11, DLST, REXO2, MYO5B, GOT2, IDH3B*
Hyperparathyroidism (familial hypocalciuric hypercalcemia)	I	*CASR, AP2S1, GNA11*
	II	*CDC73, CDKN1A, CDKN1B, CDKN2B, CDKN2C, GCM2, MEN1, RET*
Primary hyperparathyroidism	I	*MEN1, RET, CDC73, CDKN1B, GCM2*
	II	*CASR, AP2S1, GNA11, CDKN1A, CDKN2B, CDKN2C*
Macro- and micro-nodular adrenal hyperplasia	I	*ARMC5, PRKAR1A, PRKACA*
	II	*MEN1, PDE11A, PDE8B*
Von Hippel-Lindau disease	I	*VHL, BRK1*
Multiple endocrine neoplasia types 1 and 4	I	*MEN1, CDKN1B*
	II	*CDKN1A, CDKN2B, CDKN2C*
Head and neck paraganglioma	I	*SDHA, SDHAF2, SDHB, SDHC, SDHD, FH, TMEM127*
	II	*DNMT3A, MAX, MDH2, VHL, BRK1, RET*
GASTRO-INTESTINAL		
Lynch syndrome	I	*MLH1, MSH2, EPCAM, MSH6, PMS2*
	II	*EXO1, MLH3, POLD1, POLE, TGFBR2, FAN1, RPS20*
Hereditary polyposis syndromes	I	*APC, BMPR1A, GREM1, SCG5, MUTYH, NTHL1, POLD1, POLE, PTEN, SMAD4, STK11*
	II	*AXIN2, ENG, RNF43, MSH3*
Diffuse gastric cancer	I	*CDH1*
	II	*CTNNA1*
GIST	I	*KIT, PDGFRA, SDHA, SDHAF2, SDHB, SDHC, SDHD*
Other hereditary forms	I	*GALNT12*
RENAL		
Hereditary papillary renal cell carcinoma	I	*MET*
Angiomyolipoma	I	*TSC1, TSC2, FLCN*
Renal carcinoma (all histologies)	I	*VHL, BRK1, PTEN, MET, FH, FLCN*
	II	*BAP1, PBMR1, SDHA, SDHAF2, SDHB, SDHC, SDHD, TMEM127*

Hereditary leiomyomatosis and renal cell carcinoma	I	*FH*
OTHER SYNDROMES		
Hereditary breast-ovarian cancer	I	*ATM, BRCA1, BRCA2, CHEK2*
Cowden syndrome	I	*PTEN*
Tuberous sclerosis	I	*TSC1, TSC2*
Birt-Hogg-Dubè syndrome	I	*FLCN*
Li-Fraumeni syndrome	I	*P53*

Table 2. List of first- and second-generation cancer-predisposition genes included in the custom TE-ERGI v.2.0 panel, developed and validated by the Familial Cancer Unit at the IOV-IRCSS (Padua, Italy). This 81-gene panel was utilized for targeted next-generation sequencing (NGS) of DNA derived from the patient's peripheral blood, primary tumor, and hepatic metastasis. The sequencing analysis encompassed all exonic sequences along with their respective intronic flanking regions.

Microsatellite Instability Analysis

Microsatellite instability (MSI) status was evaluated on gDNA, p-tDNA and m-tDNA. The analysis was carried out using the MSI Analysis System Version 1.2 kit (Promega), which is specifically designed to identify MSI by comparing microsatellite allele profiles between matched normal and tumor DNA samples. The system simultaneously amplified seven microsatellite markers: five mononucleotide repeats (BAT-26, NR-24, NR-21, BAT-25, MONO-27), used to determine MSI, and two pentanucleotide repeats (Penta C, Penta D), included to detect potential sample contamination. PCR products were separated by capillary electrophoresis on a 3500Dx Genetic Analyzer (Applied Biosystems) equipped with a POP7 polymer and a 50-cm capillary array. The GeneScan 500 LIZ Dye Size Standard (Applied Biosystems) was added to each PCR reaction to enable accurate fragment sizing and compensate for run-to-run variation. Allele calling and fragment-size interpretation were performed using GeneMapper 5.0 software (Applied Biosystems).

Primary cell culture establishment

Primary adrenocortical carcinoma (ACC) tumor tissue was obtained from the operating room immersed in high-glucose Dulbecco's Modified Eagle Medium (DMEM HG) and maintained under sterile and refrigerated conditions until processing. At the time of preparation, the

specimen was transferred to a Petri dish containing fresh, sterile Dulbecco's Phosphate-Buffered Saline (DPBS) and thoroughly rinsed to remove blood residues and unwanted material. The tissue was then moved to a second Petri dish, where adipose tissue and necrotic areas were carefully removed by dissection. The cleaned tissue was subsequently minced into small fragments of approximately 1 mm using two crossed scalpels or, alternatively, a scalpel and forceps.

The resulting fragments were transferred into a sterile 15 or 50 mL conical tube containing fresh, sterile DPBS, allowed to settle, and then washed. The supernatant was carefully aspirated, and the washing step was repeated twice to ensure the removal of cellular debris and impurities. The washed fragments were then transferred to a new Petri dish and covered with an adequate volume of Accumax solution to ensure uniform contact between the reagent and the tissue. Samples were incubated at room temperature on an orbital shaker for 5 to 60 minutes, until the appearance of a visible "smear" at the bottom of the dish, indicative of effective tissue dissociation.

Following incubation, the cell suspension was filtered through a cell strainer to remove undigested tissue remnants. Filtration was facilitated using the plunger of a syringe, applying gentle pressure to preserve cell integrity. The filtered suspension was collected in a sterile tube and centrifuged at 300 × g to obtain a cell pellet and, if necessary, to further eliminate residual debris. The supernatant was carefully discarded, and the pellet was resuspended in 5 mL of ACC medium suitable for adrenocortical carcinoma cell growth. Isolated cells were seeded into T25 flasks and incubated under standard culture conditions (37 °C, 5% CO_2). After 48 hours, the culture medium was replaced to remove non-adherent cells and residual tissue fragments. The cell line derived from this isolation procedure and subsequently stabilized in culture was designated ID7ACC.

ID7 adrenocortical carcinoma (ACC) cells were routinely cultured under standard conditions in a humidified incubator at 37 °C and 5% CO_2. Cells were maintained as adherent cultures in tissue culture-treated plates (Corning®) using Advanced DMEM without B27 supplementation. The culture medium was replaced every 2–3 days, and cells were passaged upon reaching 70–80% confluence using TrypLE™ Express (Gibco®).

Additional adrenocortical carcinoma (ACC) cell lines were established These cell lines were derived from a metastatic lesion, a xenograft, and a cell line–derived xenograft (CDX), respectively. In addition, two commercially available ACC cell lines, H295R and SW13, were included in this study.

All ACC cell lines were cultured in complete GBM medium consisting of DMEM High Glucose supplemented with 5% fetal bovine serum (FBS), penicillin/streptomycin, L-glutamine, sodium pyruvate, sodium bicarbonate, N2 supplement, heparin, MEM non-essential amino acids (NEAA), and cytokines.

Determination of hormone production in ID7ACC cell culture

The concentrations of androstenedione, corticosterone, cortisol, 11-deoxycortisol, progesterone, 17-hydroxyprogesterone, and testosterone in cell culture supernatants were quantified using high-performance liquid chromatography coupled with electrospray ionization tandem mass spectrometry (HPLC–ESI–MS/MS). Analyses were performed using a commercially available kit (PerkinElmer).

For sample preparation, 100 µL aliquots of culture medium, calibrators, and quality control samples were transferred into 1.5 mL polypropylene tubes and mixed with 400 µL of acetonitrile containing isotopically labeled internal standards corresponding to each analyte. Samples were vortex-mixed for 1 min and centrifuged at 12,100 × g for 5 min. The resulting supernatants were transferred to new tubes and supplemented with sodium chloride to achieve supersaturated conditions.

Following an additional mixing and centrifugation step, the upper organic phases were collected, transferred to clean tubes, and evaporated to dryness under vacuum using a concentrator.

The dried residues were reconstituted in 100 µL of mobile phase consisting of 65% H_2O with 0.025% formic acid and 35% methanol with 0.025% formic acid, and subsequently transferred into vials for HPLC–ESI–MS/MS analysis.

Analysis was performed by injecting 20 µL of each sample into a liquid chromatography–tandem mass spectrometry (LC–MS/MS) system consisting of an ACQUITY UPLC I-Class HPLC (Waters) coupled via electrospray ionization to a Xevo TQ-S Micro triple quadrupole mass spectrometer (Waters). Chromatographic separation was carried out using an ACQUITY UPLC HSS T3 column (1.8 µm, 2.1 × 50 mm; Waters) maintained at 60 °C.

The mobile phase consisted of a mixture of water (65%) and methanol (35%), both acidified with 0.025% formic acid. Analytes were eluted using a gradient program at a flow rate of 0.25 mL/min, with a total run time of 12 min.

Steroids and their corresponding internal standards were monitored in positive Multiple Reaction Monitoring (MRM) mode. Quantification was performed using calibration curves generated by plotting the concentrations of the calibrators on the x-axis and the ratios of the chromatographic peak areas of each analyte to those of the corresponding internal standards on the y-axis. Instrument control, data acquisition, and data analysis were carried out using MassLynx software version 4.2 (Waters). Statistical analyses were performed using one-way analysis of variance (one-way ANOVA) to compare experimental groups. All analyses were conducted using GraphPad Prism software, version 10.0.0 (GraphPad Software, Boston, MA, USA).

Flow Cytometry Immunophenotyping

After detachment and cell counting, cells were aliquoted into flow cytometry tubes (100,000 cells per tube). Cell suspensions were washed with 1 mL of FACS buffer and centrifuged at 400 × g for 5 min. After removal of the supernatant, the cell pellet was resuspended and incubated with the antibody specific for each experimental condition.

For each antibody, the corresponding isotype control was used to assess non-specific binding. Samples were incubated for 40 min at 4 °C. Cells were then washed twice with 1 mL of FACS buffer, followed by centrifugation at 400 × g for 5 min and removal of the supernatant. Cell pellets were resuspended in 200 µL of FACS buffer and subsequently analyzed.

Flow cytometry analysis was performed by our collaborators in Würzburg on cell lines they had previously established. Data acquisition was carried out using a FACS Canto II flow cytometer (BD Biosciences). Acquired data were exported and analyzed using FlowLogic software, and graphs were generated using GraphPad Prism.

Test amount (µl)	Antibody	Fluorochrome	Brand	Cat#	Isotype (a-mouse)
2,5	B7-H3	PE	R&D	FAB1027P	IgG1-PE
2	CD56	FITC	BD	557699	IgG1-FITC
2	CD73	FITC	BD	561254	IgG1-FITC
5	CD9	APC	BD	341648	IgG1-APC
2	Epha2	PE	Biolegend	356802	IgG2b-PE
2	GD2	PE	Biolegend	357304	IgG2a-PE
10	CD81	PE	BD	555676	IgG1-PE
10	HER-3	VioBright	Miltenyi	130-107-965	REA-FITC/VioBright
2	HER-2	APC	Miltenyi	130-124-467	REA-APC
2	Melanoma (MCSP)	APC	Miltenyi	130-117-468	REA-APC
2	NKp46	PE	Miltenyi	130-112-121	REA-PE
2	EGFR	APC	Miltenyi	130-110-587	REA-APC
2	FGFR4	FITC	Miltenyi	130-126-533	IgG1-FITC
2	DLL3	Coralite Plus 647	Proteintech	CL647-25535	Rabbit IgG-APC

Table 3. Antibody panel used for flow cytometry–based phenotypic characterization of ACC cell line models. The table summarizes all monoclonal antibodies employed to evaluate surface marker expression in established adrenocortical carcinoma (ACC) cell lines, including the corresponding fluorochromes, suppliers, catalog numbers, test amounts, and matched isotype controls.

In vitro CAR T cell co-culture

Coculture experiments were performed using four adrenocortical carcinoma (ACC) cell lines: H295, SW13, a primary tumor–derived ACC cell line, and ACC XENO. For each cell line, CAR T cells were obtained from six independent donors. Tumor cell lines were cultured in complete GBM medium supplemented with 10% FBS, penicillin/streptomycin, L-glutamine, N2 supplement, MEM non-essential amino acids, sodium pyruvate, sodium bicarbonate, and cytokines. CAR T cells were generated by collaborators in the laboratory of Prof. Caruana at the University Hospital of Würzburg (Germany) according to the protocol described by Bocca et. al[127], with minor modificaitons. CAR T cells were expanded in Optimizer medium supplemented with IL-7 and IL-15 to preserve a naïve phenotype, for up to 11–15 days after retronectin removal.

On the day of coculture, 100,000 tumor cells per well were seeded in 24-well plates in 1 mL of RPMI medium and allowed to adhere for approximately 6 h. CAR T cells were then added at a 1:1 effector-to-target ratio (100,000 cells) in 1 mL of RPMI, resulting in a final volume of 2 mL per well. Cocultures were maintained for 72 h.

After 72 h, supernatants were collected into FACS tubes. Each well was washed with 500 µL of PBS to remove residual FBS, and the wash was combined with the corresponding supernatant. Adherent cells were then detached using 200 µL of trypsin, which was neutralized with 800 µL of complete RPMI, and pooled into the same FACS tube. Samples were centrifuged at 400 × g for 5 min and washed with 1 mL of FACS buffer.

Cell pellets were stained with anti-B7H3, Viobility (Miltenyi), and anti-CD45 antibodies. B7H3 and Viobility were used to identify viable tumor cells, while CD45 was used to exclude T lymphocytes. Data acquisition was performed using a FACS Canto II flow cytometer (BD Biosciences). Data were subsequently exported and plotted using GraphPad Prism.

Generation of Patient- and Cell-Derived Xenograft models

To preserve the sex background of the samples, patient-derived and cell-derived xenografts (PDXs and CDXs) were generated in 8-week-old female NOD.Cg-*Prkdc*^{scid} *Il2rg*^{tm1Wjl}/SzJ (NSG) immunodeficient mice. For PDX generation, selected 3×3 mm³ fragments of the primary tumor (F0 ACC) were were inplanted bilaterally subcutaneously in the upper flank. of two mice (four F1 PDXs). At harvest, set at 1.5 cm of maximum diameter for at least one of the tumors formed in each mouse, the F1 PDXs were measured in situ, photographed, assessed for infiltration of murine tissues, dissected, and partitioned for either downstream pathological studies or bilateral re-implantation into four recipient mice (eight F2 PDXs). One F2 PDX was dissected, and four fragments were transplanted bilaterally into two additional mice (four F3 PDXs), the other F2 PDXs were analyzed pathologically. Experimental procedures were restricted to F1–F3 passages, as these better preserve the histopathological, immunohistochemical, and genomic characteristics of the parental tumor [126].

To obtain CDXs, one F1 PDX was dissociated and, after one in vitro passage (P1), 2 × 10⁶ cells resuspended in sterile PBS (200 µL) were injected subcutaneously into each side of the dermal fat of the thoracic flanks of a single mouse (total injected cells = 4 × 10⁶). Similarly, the CDX ID7 was generated by injecting the same number of cells obtained directly from the primary ID7ACC culture, ensuring consistency with the other CDXs derived from PDX material. PDXs, CDXs, mouse organs and any identified metastasis were dissected, fixed in 10% buffered formalin for 12 hrs at 4°C, and embedded in paraffin.

Histopathology and immunohistochemical procedures

Serial sections 5 µm thick were cut from formalin-fixed, paraffin-embedded (FFPE) blocks representing the primary tumor, four liver metastases, an IVC tumor thrombus, 16 sequential PDX samples (F1: 4; F2: 8; F3: 4), and one CDX. Prior to immunostaining, sections were dewaxed, rehydrated, subjected to antigen retrieval in microwave-heated sodium citrate buffer (pH 6.0) for 10 minutes, and treated with 3% H_2O_2 to block endogenous peroxidase activity. Immunohistochemistry (IHC) for neuroendocrine and adrenal markers, including synaptophysin (SYP, antibody M7315, Agilent-Dako), calbindin 2 (CALB2, antibody HPA007305, Merck), alpha-inhibin (INH, antibody HPA019141, Merck), and MELAN-A (antibody HPA048662, Merck), as well as for $p16^{INK4a}$ (antibody PA0016, Leica Biosystems) and Ki-67 (antibody M7240, Agilent-Dako) was performed using the streptavidin–biotin–peroxidase Ab93677 kit (Abcam). Following hematoxylin counterstaining (Bio-Optica), slides were dehydrated, coverslipped, digitally scanned using a Nanozoomer (Hamamatsu Photonics), and evaluated with the NDP.view2 software (Hamamatsu Photonics, U12388-01).

Digitally scanned $p16^{INK4a}$ -stained sections were visually evaluated to estimate the percentage of positive cells. Regions of interest (ROIs) containing preserved tumor areas with well-defined and homogeneous $p16^{INK4a}$ staining patterns, either diffusely positive or diffusely negative, were delineated and mapped onto corresponding Ki-67- and H&E-stained serial sections to enable correlation analyses. Sections showing complete absence of p16INK4a staining were considered single surface regions. For each $p16^{INK4a}$ -positive and $p16^{INK4a}$ -negative ROI, Ki-67 indexes, mitotic indexes (MIs), and mitotic aberration burdens (MABs) were determined across five 1 mm² fields composed exclusively of viable tumor cells; these fields were matched in consecutive Ki-67 and H&E sections. Ki-67 indexes, expressed as the percentage of Ki-67-positive nuclei relative to total tumor nuclei, were quantified by automated digital analysis. MIs, defined as the average number of mitotic figures across the same five fields, and MABs, representing the proportion of aberrant mitoses over total mitotic figures, were visually scored according to published guidelines [128,129].

Comparisons of Ki-67 indexes between $p16^{INK4a}$ -positive and $p16^{INK4a}$ -negative ROIs were performed using contingency tables and the χ^2 test (significance threshold: $p < 0.05$). Differences in MIs across $p16^{INK4a}$ -positive and -negative regions of the primary tumor, metastases, and xenografts were evaluated with the non-parametric Kruskal–Wallis test followed by Dunn's post-hoc correction ($p < 0.05$ considered significant). Statistical analyses were conducted using GraphPad Prism, version 10.0.0 (Boston, Massachusetts, USA).

Transmission Electron Microscopy

Fresh specimens (approximately 3 mm in diameter) from the primary tumor, one hepatic metastasis, and 16 PDXs were first fixed in 2% glutaraldehyde in PBS (24 hours at 4 °C), then post-fixed in 1% osmium tetroxide (for 2 hours at room temperature), followed by staining in 1% aqueous uranyl acetate (1 hour, room temperature). Samples were subsequently dehydrated through a graded acetone series and embedded in Epon-812 resin (Electron Microscopy Sciences). Semithin sections (200 nm), stained with 1% methylene blue (Bio-Optica), were used to identify areas suitable for TEM analysis. Ultrathin sections (60 nm), contrasted with uranyl acetate and lead citrate, were examined using a Philips CM10 transmission electron microscope (FEI, Thermo Fisher Scientific).

MACSima Imaging Cyclic Staining (MICS)

Formalin-fixed paraffin-embedded (FFPE) tissue sections were prepared according to the *MACSima™ Imaging Cyclic Staining (MICS) Sample Preparation Protocol for FFPE Tissue* (Miltenyi Biotec). Following deparaffinization and rehydratation through a graded ethanol series (100%, 95%, 80%, 70%, 50%), samples were immediately mounted onto the appropriate MACSwell™ Imaging Frame (Four, cat. no. 139-124-676). Tissue sections were covered with MACSima™ Running Buffer to maintain hydration until the start of the imaging procedure.
Initial nuclear staining was performed using 4',6-diamidino-2-phenylindole (DAPI). Immediately prior to the experiment, the Running Buffer was removed and replaced with DAPI diluted 1:10 in MACSima™ Running Buffer. A volume of 250 µL of the diluted DAPI solution was added to each well, following the manufacturer's instructions. After 10 minutes of incubation in the dark at room temperature, the sections were washed three times with MACSima™ Running Buffer and covered with the final sample volume until further processing. MACSwell™ Imaging Frames were sealed with MACSwell™ Sealing Foil (130-126-865 Miltenyi Biotec) to prevent evaporation and protect samples from contaminants.

Antibody staining and MICS setup

Fluorochrome-conjugated primary antibodies (FITC, PE, and APC) were used for cyclic immunofluorescence imaging with the MACSima™ Imaging System. Details regarding antibody are provided in Table 4. Antibody mastermixes were prepared in the MACSwell™ Deepwell Plate (cat. no. 130-126-865, Miltenyi Biotec) using MACSima™ Running Buffer, according to the working volumes specified for the two-well MACSwell™ Imaging Frame. Prior to use, all antibodies were centrifuged to remove any potential sedimentation.

For wells requiring additional reagents during the MACSima™ cycling protocol, DAPI (every 7 cycles) and FcR Blocking Reagent were included as appropriate. After preparation, the antibody plate was sealed using MACSwell™ Sealing Foil to prevent evaporation and contamination during the automated staining process.

MACSima Imaging Cycling Staining

The MACSima platform is an easy-to use fully automated spatial biology solution that bridges the gap between cells phenotyping and tissue imaging. The system works through iterative staining, imaging and signal removal cycles (photobleaching or enzymatic digest). All images from different cycles are computationally merged to generate a high-dimensional protein expression profile. The racks containing the sample slides, as well as the MACSwell Deepwell Plate were placed on the sample and reagent holder. Antibodies incubation was performed according to the Milteyi's standard setting (10 mins for each antibody).

Before the iterative cycles were started, ROIs were defined for each sample based on the DAPI signal detected in the overview scan. The focus was set primarily using the autofocus, then adjusted manually for each ROI. Acquired images were processed and analyzed with MACS iQ View Imaging Software (Miltenyi Biotec, version 1.2.4). Advanced cell segmentation was performed based on nuclear (DAPI) and cytoplasmic markers, adjusting the correspective parameters (Min/Max Diameter, Separation Force, Detection Sensitivity and Smoothing Filter Sigma).

Marker expression was assigned to the segmented cells and used for the gating of cell populations and subsequent cell type annotation. Sub-gating was adjusted according to ROI- and cell type–specific expression patterns, which were visualized as scatter plots and histograms using MACS iQ View.

The obtained data were exported and graphs were produced using GraphPad Prism (Version 10.5.0)

Antigen	Order No.	Fluorochrome	Company
MelanA / MART1	130-118-608	FITC	Miltenyi Biotec
Synaptophysin	130-119-347	PE	Miltenyi Biotec
Vimentin	130-118-361	APC	Miltenyi Biotec
p16	68401S	FITC	Cell Signaling
Inhibin	HPA019141	PE	Sigma-Aldrich
Calbindin 2	HPA007305	APC	Sigma-Aldrich
CD56	130-128-467	FITC	Miltenyi Biotec
Ki67	130-119-357	APC	Miltenyi Biotec
Actin (Smooth Muscle)	130-123-363	FITC	Miltenyi Biotec
CD31	130-128-769	PE	Miltenyi Biotec
Collagen I	130-127-017	APC	Miltenyi Biotec
CD45	NBP2-34528AF647	APC	NovusBio
CD4	130-127-906	PE	Miltenyi Biotec
CD8	130-117-202	APC	Miltenyi Biotec
CD16	130-128-774	PE	Miltenyi Biotec
CD11c	130-133-325	PE	Miltenyi Biotec
CD68	130-131-521	PE	Miltenyi Biotec
CD206	PA5-82136	APC	ThermoFisher
CD20cyto	130-126-166	PE	Miltenyi Biotec
CD11b	130-128-773	PE	Miltenyi Biotec
CD90	130-124-176	PE	Miltenyi Biotec
IL13Ra	BS-2461R	FITC	Bioss Antibodies
B7-H3	130-137-219	PE	Miltenyi Biotec
GD2	554272	FITC	BD Biosciences
EphA2	LS-B1794-50	FITC	LSBio
Her2	130-127-979	PE	Miltenyi Biotec
Her3	sc-415 Pe	PE	Santa Cruz Biotechnology
AN2 (CSPG4)	130-116-441	APC	Miltenyi Biotec
EGFR	BS-0165R-APC	APC	Bioss Antibodies
Podoplanin	130-126-165	APC	Miltenyi Biotec
CD334	130-126-533	FITC	Miltenyi Biotec
DLL3	CL647-25535	APC	Proteintech
WGA	29022-1	FITC	Biozol

Table 4. MACSima Antibody Panel for Multiplexed Immunophenotyping of ACC. High-content antibody panel comprising 33 markers aimed at identifying the main immune, stromal, and tumor cell populations of the primary tumor and the hepatic metastasis.

Results

Clinicopathological presentation

A 60-year-old woman was admitted to the emergency department of St. Andrew's University Hospital because of acute abdominal pain. The Eastern Cooperative Oncology Group (ECOG) and World Health Organization (WHO) performance grade corresponded to 0 (fully active patient, able to perform all pre-disease activities without restriction). The patient reported no smoking or exposure to tobacco smoke, and no personal or family history of cancer or chronic disease.

Routine laboratory tests were within normal limits, and the physical examination did not reveal any signs or symptoms suggestive of adrenal hormone excess. Consequently, a hormonal workup was performed (Table 1, preoperative values column) to evaluate potential adrenal hormone overproduction. This assessment demonstrated autonomous cortisol secretion, evident from the 1 mg dexamethasone suppression test, as well as mild hyperandrogenism, indicated by elevated serum levels of dehydroepiandrosterone sulfate and 17-hydroxyprogesterone (Table 1, with abnormal preoperative values highlighted in bold).

Parameter	Pre-operative	Post-operative	Normal range
DHEA-S	**272.4 ug/dl**	**487.0 ug/dl**	30-182 ug/dl
17-OHP	**4.3 ng/ml**	**388.5 ng/ml**	0.08-1.3 ng/ml
TT	0.3 ng/ml	**9.9 ng/ml**	0.1-0.57 ng/ml
ANST	2.10 ng/ml	**18.2 ng/ml**	0.3-10 ng/ml
CORT	298.5 nmol/l	**696.2 nmol/l**	101-536 nmol/l
ACTH	17.3 pg/ml	6.8 pg/ml	4.7-48.8 pg/ml
UFC	49.96 ug/24 h	**432.0 ug/24 h**	4.30-176 ug/24 h
ALD	13.8 pg/ml	-	17.6-232 pg/ml
PRA	0.05 ng/ml/h	-	0.06-4.69 ng/ml/h
UFM	0.14 mg/24 h	-	0.05-0.34 mg/24 h
NMN	0.18 mg/24 h	-	0.08-0.45 mg/24 h
DST 1mg	**183.9 nmol/l**	-	<50 nmol/l

Table 5. Hormonal assessment (pre- and post-operative values)

Pre-operative testing showed mild hyperandrogenism, evidenced by increased serum DHEA-S and 17-OHP levels, and autonomous cortisol secretion, as demonstrated by the 1-mg overnight DST. Following surgery, metastatic progression was associated with further elevations in serum glucocorticoids, urinary free cortisol, and circulating androgens. Abbreviations: DHEA-S, serum dehydroepiandrosterone sulphate; 17-OHP, serum 17-hydroxyprogesterone; TT, total serum testosterone; ANST, serum androstenedione; CORT, morning serum cortisol; ACTH, serum adrenocorticotropic hormone; UFC, urinary free cortisol; ALD, serum aldosterone; PRA, plasma renin activity; UFM, 24-hour urinary fractionated metanephrines; NMN, 24-hour urinary fractionated normetanephrines; DST, overnight 1-mg dexamethasone suppression test. Post-operatively, ALD, PRA, UFM, and DST were not assessed. Abnormal values in bold.

On admission, abdominal magnetic resonance imaging (MRI) revealed a large, well-defined mass (10.3 × 5.5 × 9.0 cm) in the right adrenal region, exhibiting heterogeneous internal characteristics suggestive of calcified and necrotic areas. (Figure 1 A, B)

MRI of the liver identified three putatively metastatic nodules of 1.3 cm, 1.0 cm, and 2.8 cm in the IV, V and VI hepatic segments, respectively, and a 6.3 cm likely sub-occlusive thrombus in the inferior vena cava (IVC) (Figure 1A, 1B, and data not shown). Chest computed tomography (CT) showed no abnormalities (Figure 1C). The initial therapeutic strategy consisted of cytoreductive surgery, including right adrenalectomy, inferior vena cava (IVC) thrombectomy, and multiple liver metastasectomies, proposed in light of the patient's good ECOG performance status and the anticipated clinical benefit. The procedure was completed without complications and ensured effective control of locoregional pain and hormonal hypersecretion. High-dose mitotane therapy (6 g/day) was initiated immediately after surgery, with the goal of reaching the therapeutic plasma concentration range (14–20 mg/L) before considering a transition to the EDP-M regimen. One month after surgery, whole-body CT revealed extensive disease progression, with metastatic lymphadenopathy in the mediastinal, para-aortic, and peri-renal regions, along with multiple hepatic and pulmonary metastases and bilateral invasive pleural implants consistent with transcoelomic spread (Figure 1D–F). This radiologic worsening was paralleled by a marked endocrinologic imbalance, including elevated serum glucocorticoids and androgens, high urinary free cortisol, and the onset of respiratory and hormonal symptoms (Table 2, postoperative values column, outliers highlighted in bold), while albumin and hepatic transaminases remained within normal limits. The clinical course rapidly deteriorated, with progressive respiratory compromise leading to death from respiratory failure 40 days after surgery, before therapeutic steady-state mitotane levels could be achieved.

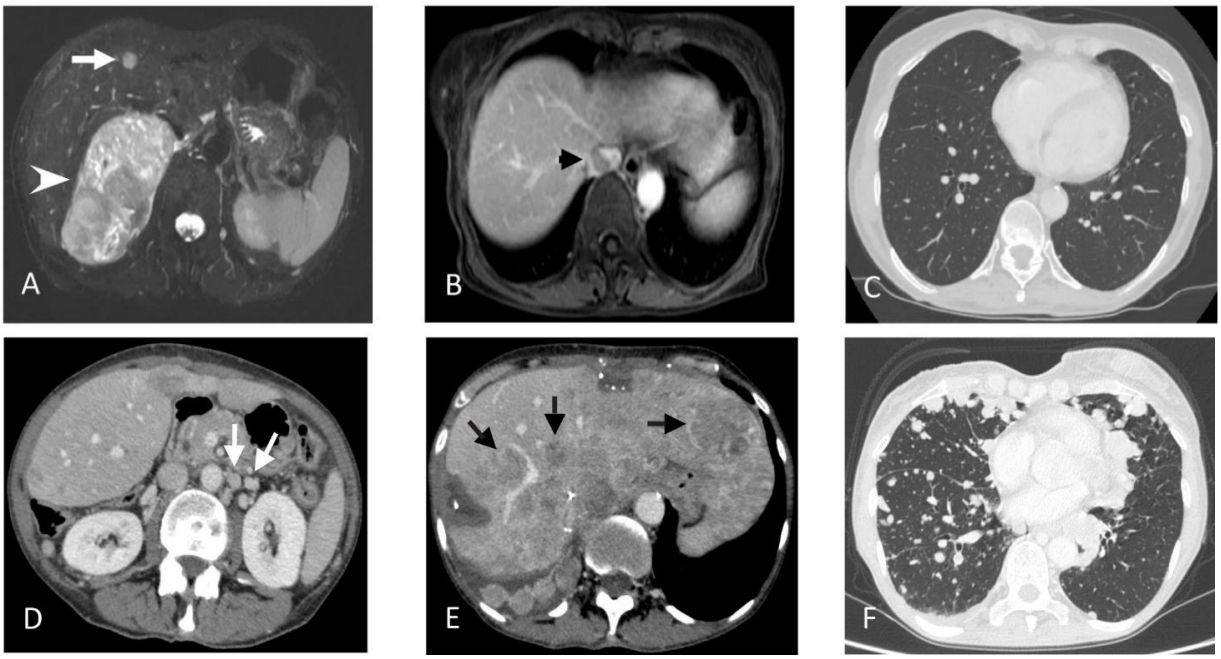


Fig.1 Preoperative multi-modal imaging assessment (A-C). (A) Axial T2-weighted MRI with fat saturation (L2 level): A large, heterogeneous solid mass is identified in the right adrenal lodge (10.34 x 5.54 cm), positioned lateral to the liver's right lobe and anterior to the inferior vena cava (IVC). The lesion displays hyperintense foci consistent with necrosis and internal calcifications. A 1.0 cm metastatic nodule is visible in hepatic segment V (white arrow), representing one of three lesions identified during the scan. (B) Contrast-enhanced T1-weighted MRI (VIBE sequence, portal venous phase at L1 level):* Visualization of the inferior vena cava reveals a significant sub-occlusive tumor thrombus (black arrow). (C) Contrast-enhanced lung CT (D10 level): No evidence of pulmonary pathological findings or metastases. *VIBE: Volumetric Interpolated Breath-hold Examination.

Follow-up imaging assessment one-month post-surgery (D-F). (D) Contrast-enhanced abdominal CT (L3 level): Prominent lymphadenopathy is observed, characterized by multiple enlarged para-aortic and peri-renal lymph nodes (white arrows). (E) Contrast-enhanced abdominal CT (D12 level): Assessment confirms hepatomegaly associated with the presence of several hypodense metastatic nodules (black arrows). (F) Contrast-enhanced thoracic CT (D9 level): Imaging reveals extensive pulmonary involvement with numerous bilateral metastatic foci, appearing both as isolated and confluent lesions. Findings also include massive mediastinal lymphadenopathy, bilateral pleural thickening, and discrete neoplastic pleural implants.

Integrated histopathological, immunophenotypic, and ultrastructural characterization of the tumor

Representative samples of the primary tumor, hepatic metastatic lesions, and caval thrombosis were received for analysis. Pathological diagnosis was high-grade conventional ACC stage IVa (pT4, pN2, pM1), indicating a primary tumor with extensive local invasion (pT4), significant regional lymph-node involvement (pN2), and confirmed distant metastases (pM1), according to the modified ENS@T (mENS@T) criteria. The Weiss score was 7/9, based on diffuse growth, high nuclear grade, high mitotic count, frequent mitotic aberrations, infarct-type necrosis, vascular and capsular invasion, and periadrenal adipose-tissue infiltration. Histological examination of the hepatic nodules confirmed the presence of three distinct metastatic lesions. Although the surgical margins of both the adrenal mass and the liver metastases were free of residual tumor (R0 resection), the subocclusive thrombus in the IVC showed superficial colonization by friable neoplastic protrusions extending into the venous lumen, demonstrating that tumor cells had gained access to the central venous circulation.

Immunohistochemical evaluation revealed a heterogeneous immunopositivity (<30% of tumor cells) for synaptophysin (SYP), a synaptic-vesicle glycoprotein expressed in normal and neoplastic neuroendocrine cells and commonly associated with pheochromocytomas as well as cortisol-producing adrenocortical tumors [130]. The tumor also showed expression of calbindin 2 (calretinin), a calcium-binding protein, and alpha-inhibin (INH), a member of the TGF-β family involved in the feedback regulation of pituitary FSH production; together, these markers help distinguish cortical from medullary adrenal neoplasms[131]. In addition, staining was positive for MELAN-A, a melanoma-associated antigen that is likewise valuable in differentiating primary adrenocortical carcinomas from metastatic lesions (Figure 2 A-B). The combined expression pattern of these markers thus provides strong diagnostic support for a primary adrenocortical origin of the tumor, helping to exclude other neuroendocrine or metastatic neoplasms that could involve the adrenal gland.4

The metastatic liver nodules displayed histological and immunohistochemical characteristics consistent with those of the primary tumor, although generally less pronounced, except for a more evident papillary growth pattern. Immunoreactivity for SYP, CALB2, and INH was predominantly confined to the vascularized regions at the periphery of the metastases and along blood vessels. In contrast, MELAN-A expression was largely absent, detectable only weakly in a few scattered cells (Figure 2 A–B).

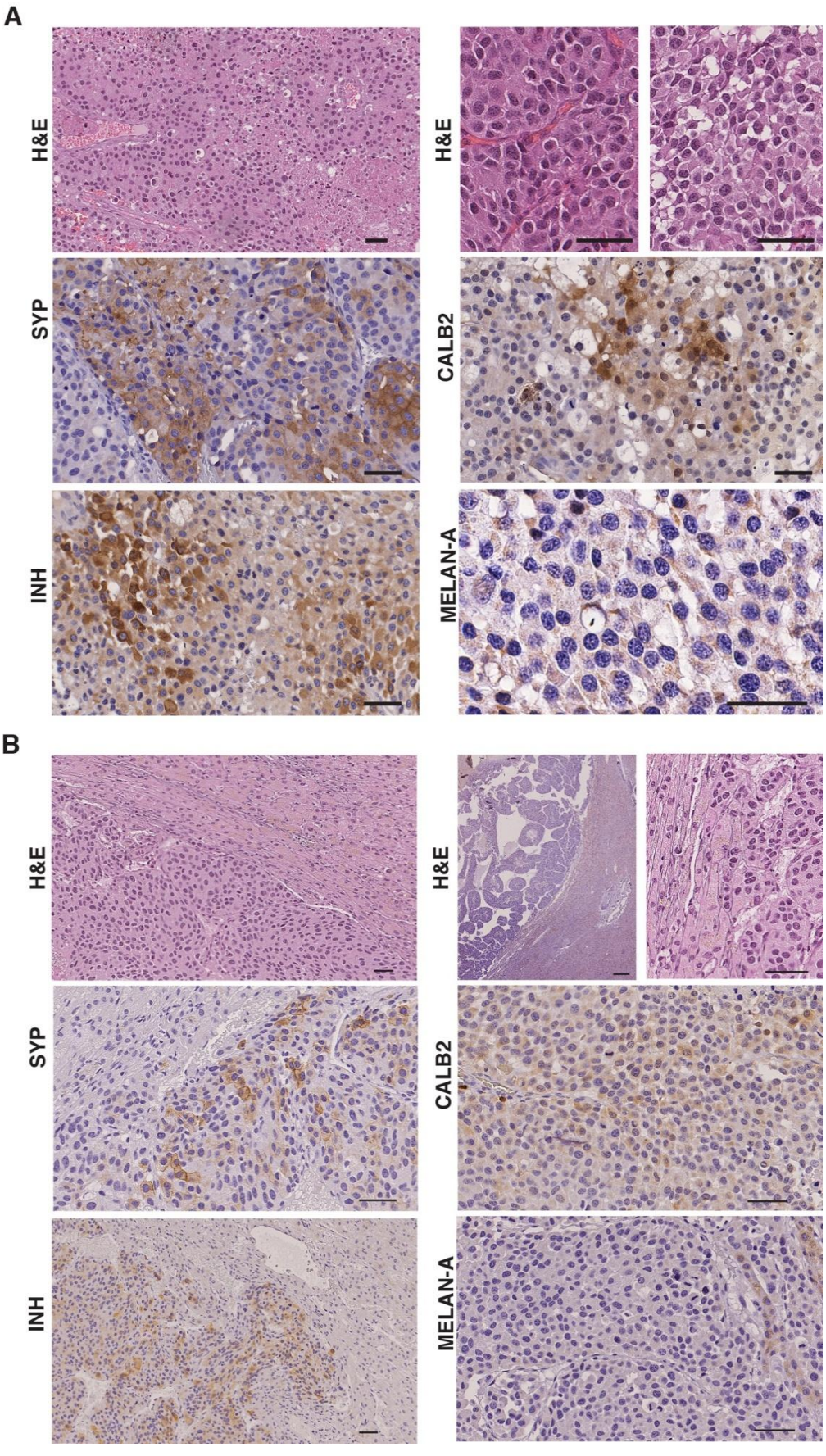

A
H&E
SYP
INH
H&E
CALB2
MELAN-A
B
H&E
SYP
INH
H&E
CALB2
MELAN-A

Fig. 2. Histopathological and immunohistochemical characterization of resected primary and metastatic lesions. (A) Primary Tumor: H&E staining (top row) reveals expansive sheets of large polygonal cells divided by delicate fibrovascular septa. Extensive coagulative necrosis and hemorrhage are observed, particularly in regions distal to vasculature. Cellular morphology includes spherical-to-ovoid nuclei and eosinophilic "ground-glass" cytoplasm; notably, certain areas exhibit significant lipid accumulation characterized by large, clear cytoplasmic vacuolations. The primary lesion demonstrates well-defined focal immunoreactivity for synaptophysin (SYP), calbindin 2 (CALB2), and alpha-inhibin (INH), alongside a mosaic expression pattern for MELAN-A. All scale bars in panel A represent 50 μm.
(B) Hepatic Metastasis: Representative analysis of one of three liver lesions. H&E images show interlacing nests of polygonal tumor cells supported by thin septa, exhibiting a papillary growth pattern within areas of pseudocystic degeneration. At the tumor margin, neoplastic cells directly abut hepatocyte cords (arrows) without an intervening fibrotic capsule, indicative of rapid expansion. Immunohistochemistry shows focal positivity for SYP and INH (predominantly peripheral) and CALB2 (perivascular), while MELAN-A expression is restricted to rare, isolated cells. Scale bars represent 50 μm, except for the initial H&E image in the right column (1 mm).

Light and electron microscopy of both the primary tumor and a liver metastasis revealed the presence of two distinct cellular morphotypes. The predominant population, accounting for approximately 70% of the cells, consisted of large polygonal or ovoid clear cells characterized by fine-grained, sometimes focally clumped nuclei and prominent nucleoli. The second, less represented population (<30%) comprised smaller, darker, and strongly eosinophilic cells with coarse chromatin, dense cytoplasm, and elongated peripheral filopodia that extended between adjacent clear cells. Ultrastructurally, both morphotypes displayed abundant mitochondria, with lamelliform or vesicular cristae and extensive contacts with both rough and smooth endoplasmic reticulum (ER). Numerous mitochondria appeared swollen, with disrupted or degraded cristae (cristolysis) and an electron-lucent matrix, a phenotype suggestive of oxidative stress and acidification of the intracristal space (Figure 3A–B) [132–135]. Prominent ER and scattered lipid droplets were also evident, consistent with active steroidogenesis and mitochondrial dysfunction (Figure 3 A,B).

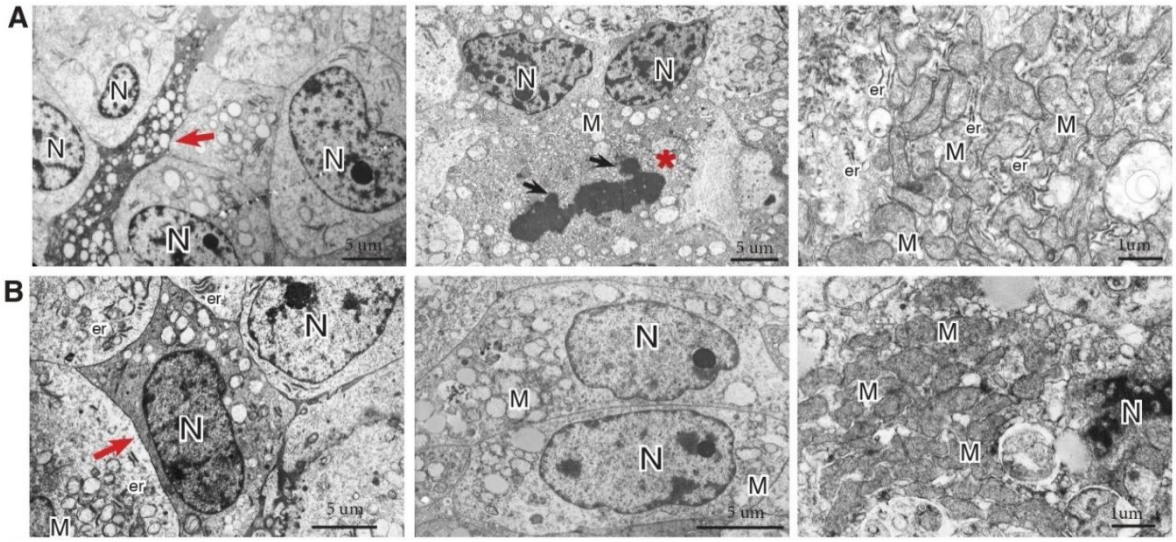


Fig. 3. Ultrastructural analysis of primary and metastatic lesions via Transmission Electron Microscopy (TEM). Both the primary (A) and the metastatic (B) samples appeared as a mosaic of two ultrastructural morphotypes, the predominant one presenting large, clear cytoplasm and fine-grained, focally-clumped ovoid nuclei (N) with prominent nucleoli; the less abundant (<30%, left panels in A and B, red arrows) with coarser chromatin, electron-dense nucleoplasm and cytoplasm (indicating affinity for osmium tetroxide, a characteristic linked to lipogenesis), and thin cytoplasmic projections (filopodia) insinuating between adjacent clear cells (red arrow in B). A mitotic metaphase is visible in the lower portion of the central micrograph in panel A. Both cell morphotypes showed very abundant, often swollen mitochondria (M), with expanded vesicular cristae (mainly in A, right panel) or diffuse cristolysis exposing electron-lucent matrix (mainly in B, right panel). Prominent endoplasmic reticulum (er), and extensive er-mitochondria contacts were also evident. Bars = 5mm in all micrographs.

Mutational and structural genetic landscape

Second-generation sequencing (NGS), which enables simultaneous analysis of extensive SNVs and CNVs including noncoding regions, represents an integrated and highly informative approach for detecting both point mutations and structural genomic alterations with potential clinical relevance. In this case, targeted NGS was performed using a predefined panel of 81 cancer-related genes, including flanking regions (Table 2).

At the germline level, no pathogenic or likely pathogenic variants and no copy-number alterations were detected, consistent with the patient's negative family history and supporting

the sporadic origin of the tumor. Somatic variant calling, on the other hand, identified a single relevant alteration: a missense mutation in TP53 [NM_000546.6:c.843C>A p.(Asp281Glu)], located in exon 8. (*This substitution replaces cytosine with adenine at nucleotide 843 resulting in the replacement of the conserved aspartic acid residue at codon 281, located within the DNA-binding domain, with glutamic acid,)* causing a structural change predicted to impair transcriptional transactivation activity. The mutation was detected at a variant allele frequency (VAF) of approximately 27% in both the primary adrenal tumor (p-tDNA) and liver metastasis (m-tDNA), as reflected by the reduced height of the variant peak in sequencing chromatograms.



Fig. 4. Sanger Validation of the TP53 (NM_000546.6) c.843C>A p.(Asp281Glu) variant. Sanger sequencing chromatograms and Binary Alignment Map (BAM) file visualizations compare the partial TP53 sequence across DNA derived from peripheral blood, the primary tumor, and a hepatic metastasis. The red line highlights the c.843C>A substitution. Analysis of the germline DNA (blood) reveals only the wild-type Cytosine at position 843, confirmed by both Sanger and NGS (100% of reads; depth: 1537). Conversely, both the primary tumor and the liver metastasis exhibit a minor Adenine peak on Sanger sequencing, which NGS identifies as unbalanced heterozygosity, with the variant represented in 27% of reads (depths: 792 and 1206, respectively).

According to ACMG/AMP guidelines and the ClinGen TP53 Expert Panel specifications (Version 2.3.0), it is classified as likely pathogenic (Tier II, likely oncogenic) [76,136–138]. Notably, several heterozygous SNPs within the TP53 locus showed a consistent allelic imbalance of approximately 70:30 in both tumor samples, mirroring the VAF of the TP53 mutation (Table 6).

TP53 genomic locus (NC_000017.10)	gDNA		p-tDNA		m-tDNA		TP53 SNPs (NM_000546.5)
	Allele 1	Allele 2	Allele 1	Allele 2	Allele 1	Allele 2	
g.7577095	C	C	C	**A***	C	**A***	c.843C>A p.(Asp281Glu)
g.7578115	G	A	G	A	G	A	c.672+62A>G
g.7578645	A	G	A	G	A	G	c.376-91G>A
g.7579472	G	C	G	C	G	C	c.215C>G p.(Pro72Arg)
g.7579801	G	C	G	C	G	C	c.74+38C>G
Heterozygosity	50%	50%	70%	30%	70%	30%	

Table 6. Comparison of five informative SNPs spanning the TP53 locus on chromosome 17 (positions 7577095 to 7579801, hg19) in DNAs from blood (gDNA), primary tumor (ptDNA), and one hepatic metastasis (metDNA). The SNPs show balanced heterozygosity (50:50) in gDNA and similar allelic skewings (≈70:30) in ptDNA and metDNA. The somatic TP53 variant A* mirrors the minor allele fraction. This consistent tumor-associated allelic imbalance at the TP53 locus could be explained by a complex chromosomal rearrangement.

Although neither targeted NGS-based CNV analysis nor CGH–SNP array detected copy-number changes involving TP53, this recurrent allelic skew suggests the presence of an undetermined complex chromosomal rearrangement affecting the TP53 region. No additional clinically relevant somatic alterations were identified.

DNA extracted from blood, skin, the adrenal tumor, and a liver metastasis was analyzed using the MSI Analysis System kit, Version 1.2, a fluorescent PCR-based assay designed to assess the microsatellite instability (MSI) status of human cells and tissues. The kit co-amplifies seven markers: five quasi-monomorphic mononucleotide repeats (BAT-25, BAT-26, NR-21, NR-24, and MONO-27), which are informative for determining MSI status, and two pentanucleotide markers (Penta C and Penta D), used to verify sample identity and exclude contamination. As shown in Figure 5, the electropherograms for all five mononucleotide markers indicated a stable

microsatellite phenotype, consistent with a microsatellite-stable status (MSS). The pentanucleotide markers confirmed the absence of sample contamination or cross-sample confounding.

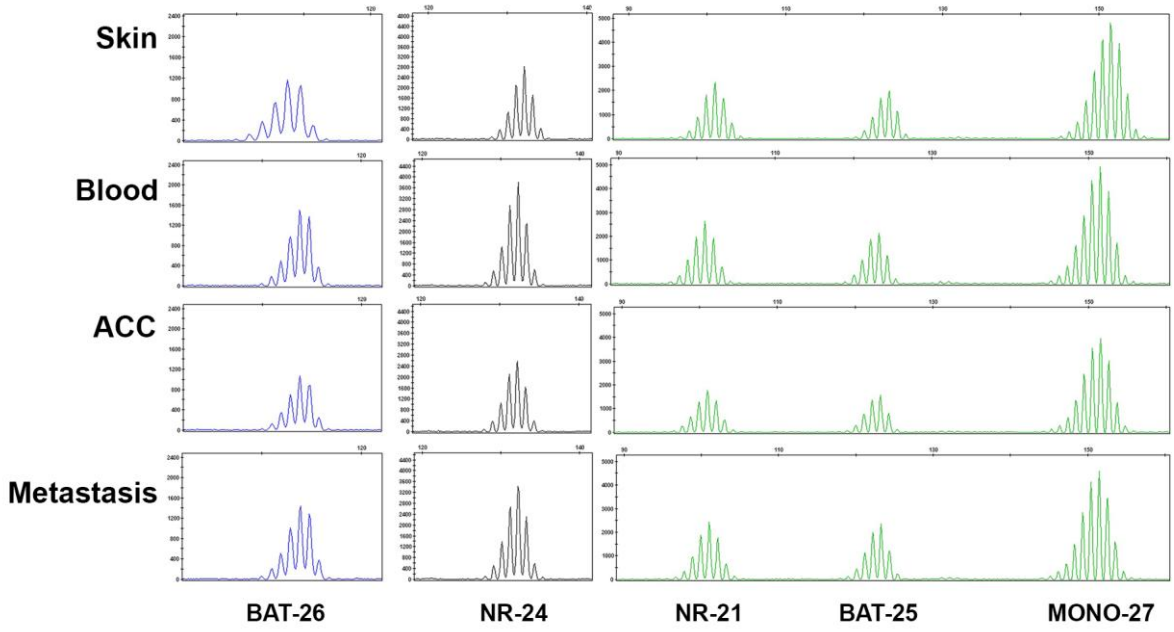


Fig. 5. Assessment of Microsatellite Instability (MSI) status across somatic and germline samples. Electropherograms display the results for five quasi-monomorphic mononucleotide repeat markers (BAT-26, NR-24, NR-21, BAT-25, and MONO-27) analyzed in DNA derived from skin, blood, the primary adrenocortical carcinoma (ACC), and a surgically resected hepatic metastasis. All samples demonstrate a microsatellite-stable (MSS) phenotype. The analysis included two pentanucleotide repeats (Penta C and Penta D) to verify the absence of sample contamination (data not shown).

In contrast to the low mutational burden and the MSS phenotype, array-based structural analysis revealed an intricate landscape of somatic copy-number alterations and allelic imbalances. Both the primary lesion and the liver metastasis exhibited wide chromosomal gains and losses, as detailed in Figure 6. A striking feature shared by both p-tDNA and m-tDNA was the presence of extensive copy-neutral loss-of-heterozygosity (CN-LOH) regions on chromosomes 6, 7, 8, 11, and 22, findings compatible with mitotic recombination and indicative of underlying chromosomal instability (CIN) (Figure 6). The CGH–SNP profiles of the primary tumor and

the metastasis showed a highly concordant pattern of chromosomal alterations, supporting their derivation from a common clonal origin. (Figure 6).

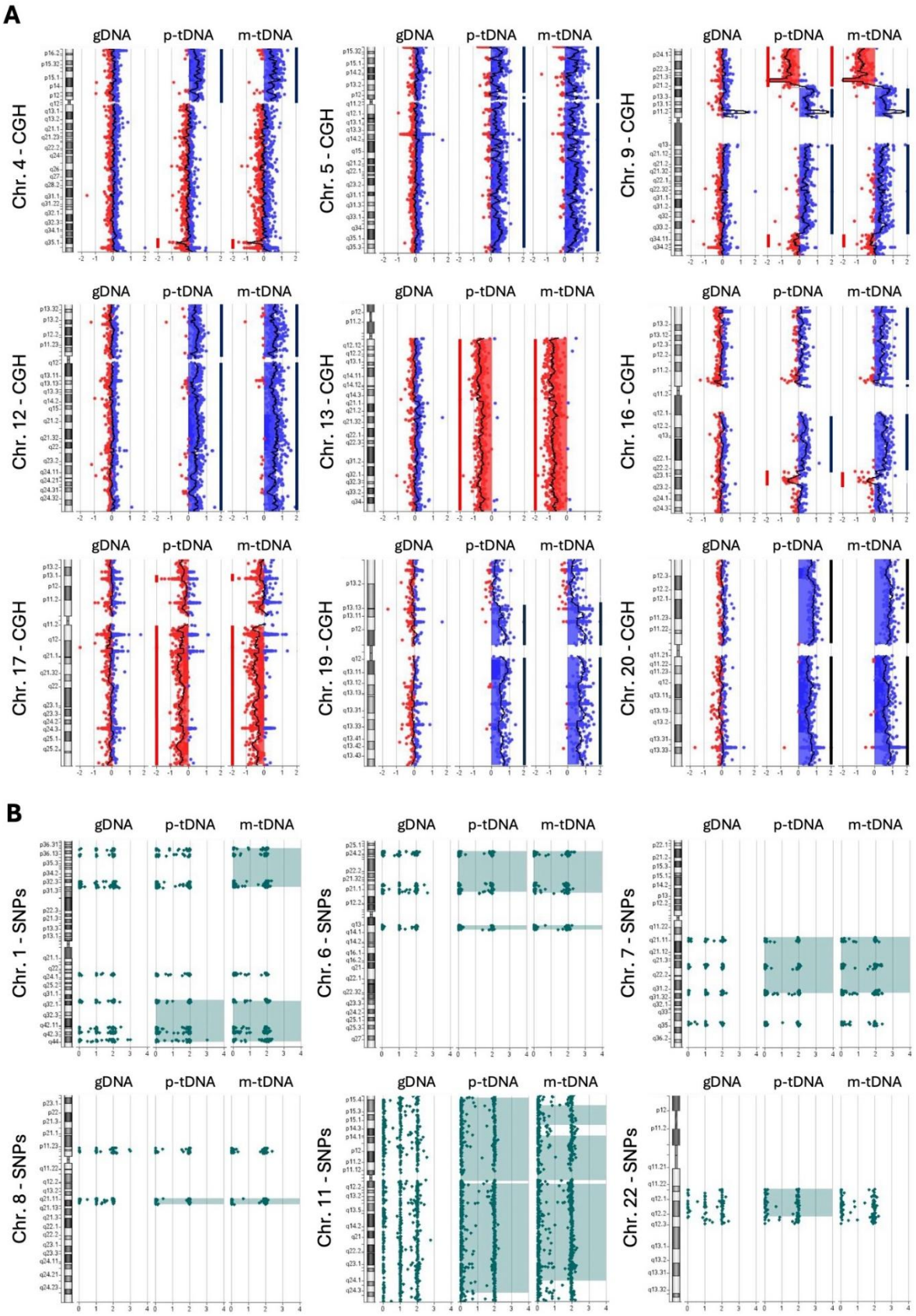


Fig.6.). CGH–SNP array profiling of DNAs from blood (germline, gDNA) primary tumor (p-tDNA), and a liver metastasis (m-tDNA A) CGH profiles of chromosomes 4, 5, 9, 12, 13, 16, 17, 19, and 20 showing large copy number (CN) alterations in gDNA, p-tDNA and m-tDNA. Log2 ratio values are shown relative to a diploid

reference (log2 = 0), with blue and red segmented profiles indicating copy number gains and losses, respectively. Both p-tDNA and m-tDNA exhibit large-scale chromosomal gains involving chromosomes 4 (p11–p16.3), 5 (p15.33–p12 and q11.1–q35.2), 9 (p13–q33), 12 (p13.33–p11.1 and q12–q24.33), 16 (p13.3–p11.1 and q12.1–q22.2), 19 (p13.2–p11 and q13.43–q11), and 20 (entire chromosome), as well as losses affecting chromosomes 4 (q34.3–q35.1), 9 (p24–p21), 13 (q11–q34), 16 (q23.1), and 17 (p13.1 and q11.2–q25.3). Smaller copy number alterations detected on chromosomes 1, 2, 3, 6, 7, 11, 14, 15, and 22 are not shown. Notably, losses at chromosome 9p included a homozygous deletion at 9p21.3.

B) SNP analysis of chromosomes 1, 6, 7, 8, 11 and 22 in gDNA, p-tDNA and m-tDNA. Green dots signify copy number states of the allele (0 = AA, 1 = AB, 2 = BB). Exclusively homozygous allelic states (AA or BB) indicate copy-neutral LOHs (CNNLOHs). Segments of chromosomes 1, 6, 7, 8, 11, and 22 affected by LOH or CNNLOH in p-tDNA and m-tDNA are shaded in light green.

A distinct focal alteration, absent in germline DNA but present in both p-tDNA and m-tDNA, consisted of a homozygous deletion at chromosome 9p21.3 involving the CDKN2A/B locus, an event recurrently observed in approximately 15% of human cancers and associated with tumor progression and poor prognosis [66,72] (Figure 7). In line with this finding, comparison with blood-derived DNA showed that both tumor samples exhibited a marked loss of nucleotide polymorphisms across the 9p21.3 region [139,140], confirming biallelic deletion of the CDKN2A/p16^{INK4a}/p14ARF and CDKN2B/p15INK4B tumor-suppressor genes. These genes encode key regulators of cell-cycle arrest activated in response to genomic injury, including oxidative stress [141,142]. Notably, the same homozygous 9p21.3 deletion pattern was also identified in DNA derived from primary tumor cultures, as well as in PDX and CDX models, indicating that this alteration is an early and clonally preserved event in the tumor's evolution.

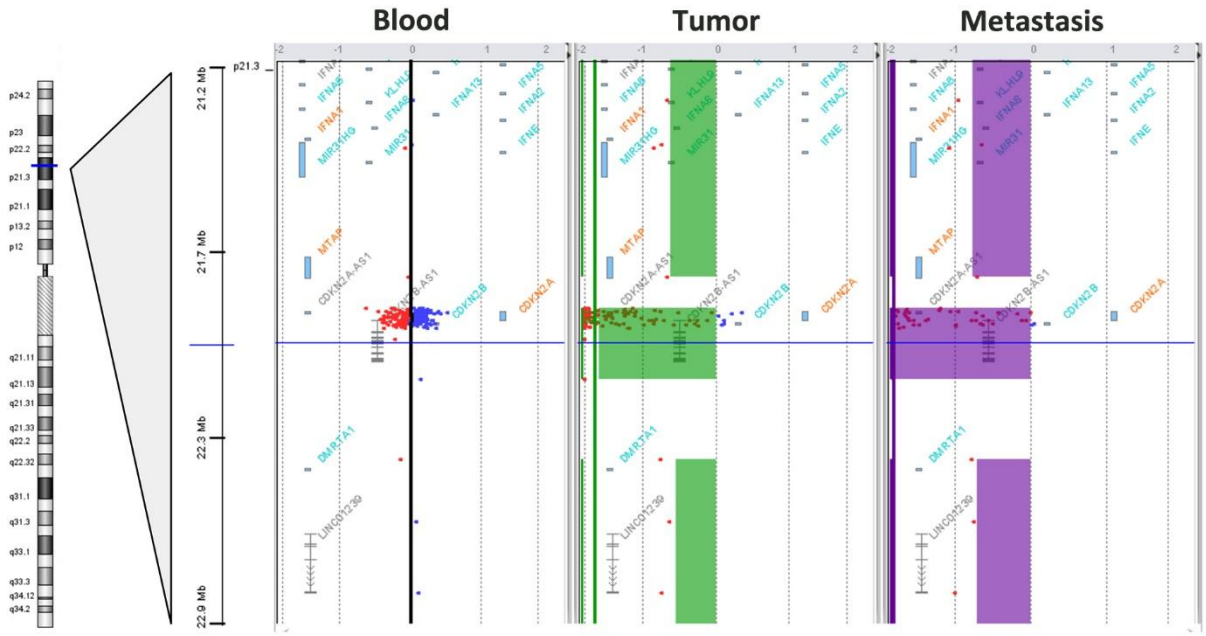


Figure 7. Chromosome 9 map with magnified array CGH profiles of the 9p21.3 region in DNAs from blood (not highlighted), primary tumor (highlighted in green) and a hepatic metastasis (highlighted in purple). The CGH profiles show log2 probe ratios (colored dots) plotted in relation to chromosomal position (vertical axis) and copy number (horizontal axis, from -2 to +2). A log2 ratio close to zero signifies normal diploid copy number, while increased or decreased log2 ratios indicate copy number gains (blue dots) or losses (red dots). The CGH profiles of the primary tumor and paired hepatic metastasis share a homozygous deletion of the region harboring the CDKN2A/B locus, signified by copy number shifts towards -2. The deletion does not involve relevant adjacent telomeric and centromeric genes (e.g., MTAP and DMRTA1). The observed deletion likely represents a driver alteration selected during tumor expansion. Due to potential intra-tumor heterogeneity, single-cell sequencing would be essential to resolve subclonal structure and confirm the extent of the selection.

Correlation of $p16^{INK4a}$ status with tumor proliferation and mitotic instability

We validated the homozygous 9p21.3 deletion using IHC for $p16^{INK4a}$, a protein encoded by *CDKN2A* whose loss is independently associated with metastatic behavior and poor survival in several cancers, including ACC.

Digital image analysis of $p16^{INK4a}$ immunostaining was performed on sections from all three FFPE blocks of the primary tumor, revealing heterogeneous labeling patterns with two main regions of interest (ROIs): one predominantly $p16^{INK4a}$ -positive and another predominantly $p16^{INK4a}$ -negative (Figure 8). In contrast, all sections from the four liver metastases, each analyzed as a separate ROI, and the IVC tumor thrombus were completely negative for tumor-associated $p16^{INK4a}$. The low cellularity of the IVC thrombus precluded quantitative assessment.

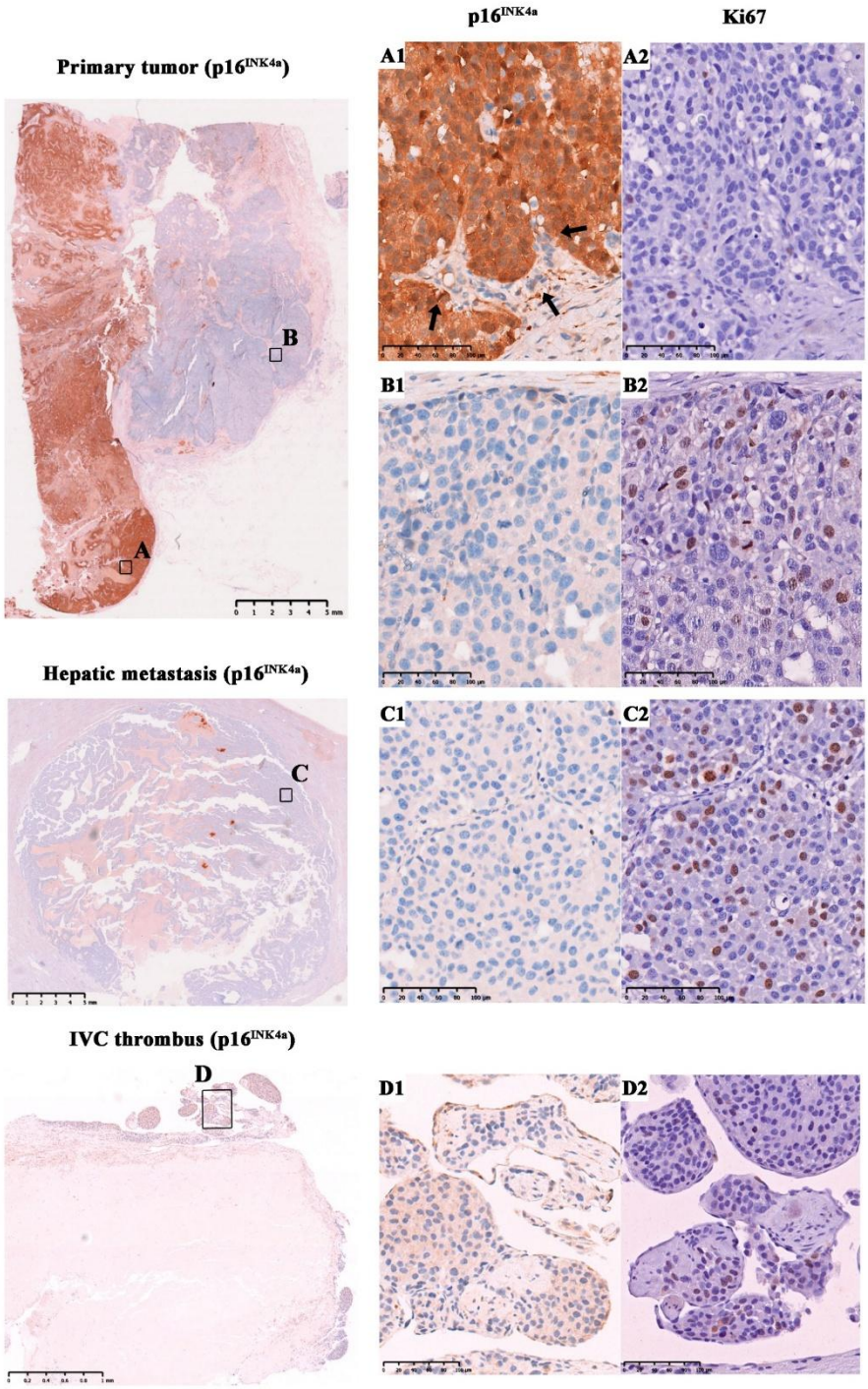


Fig.8. Loss of p16INK4a expression and increased Ki67 index in metastatic sites. Left panels: Immunostaining for p16INK4a in the primary tumor revealed a heterogeneous pattern with sharply demarcated positive and negative areas (upper left), whereas both the hepatic metastases (middle left) and the inferior vena cava (IVC) tumor thrombus (lower left) were uniformly negative for p16INK4a. Regions labeled A, B, C, and D are shown at higher magnification (20×) on the right, illustrating p16INK4a (A1–D1) and Ki67 (A2–D2) staining. Ki67 immunostaining demonstrated a higher proliferative index in the analyzed hepatic metastases.

The p16INK4a+ regions of the primary tumor always contained rare pINK4a- cancer cells, single or in clusters, suggesting independent development of CDKN2A/B-deleted cell clones, which sometimes showed infiltrative arrangement at the pushing margins of p16INK4a + neoplastic cell clusters (A1). On the other hand, clusters of p16INK4a + cells persisted in the p16INK4a- primary tumor regions, particularly along blood vessels (B1), contrasting with the total lack of p16INK4a+ cells in the metastases and in the neoplastic vegetations along the residual lumen of the IVC thrombus (C1, D1).

Given that $p16^{INK4a}$ specifically inhibits the cyclin-dependent kinases CDK4 and CDK6, key drivers of the G1-S phase transition [143], we evaluated the relationship between p16INK4a status and tumor proliferative activity by analyzing both Ki67 proliferation indexes and mitotic counts. Digital image analysis of five 1 mm² fields containing only viable tumor cells revealed average Ki67 indexes ranging from 6.31 to 12.6 in $p16^{INK4a}$ -positive regions and from 10.2 to 24.3 in $p16^{INK4a}$ -negative regions of the primary tumor. Hepatic metastases, all $p16^{INK4a}$ -negative, showed broader proliferation, with Ki67 indexes spanning 4.9 to 33.2 (Table 7).

FFPE SECTION	$P16^{INK4a}$		Ki67 index#	MI*	MAB°
	%-	%+			
PT 1.2	100	0	24.3	26.8	23,9
PT 1.3	5	95	12.6	17.0	43,5
PT 1.4-area 1	5	95	6.3	11.0	49,1
PT 1.4-area 2	100	0	10.2	9.4	31,9
HM 1.7	95	5	4.9	12.4	27,4
HM 1.9	100	0	22.1	24.0	29,2
HM 1.13	100	0	33.2	19.2	13,5
HM 1.15	100	0	23.4	28.6	25,2
IVC 1.22	100	0	Na	Na	Na
PDX F1a	90	10	26.2	34.2	24,6
PDX F1b	100	0	9.0	47.4	16,5
PDX F2a	90	10	25.6	25.8	34,9
PDX F2b	95	5	24.0	34.4	39,5
PDX F3a	95	5	25.9	37.4	13,4
PDX F3b	90-95	05-ott	34.0	41.0	28,8
CDX	90	10	27.3	36.2	11,6
CDX HM	100	0	29.3	39.4	40,1

Table 7. Quantitation of Ki-67 immunostaining, mitotic indexes (MIs), and mitotic aberration burdens (MABs) in regions of interest (ROIs) with positive or negative p16INK4a immunostaining of the patient's tumor and its solid tumor-derived and tumor cell-suspension-derived xenograft models (PDXs and CDXs).
#: Ki67 positivity is expressed as the percentage of Ki67-positive cells out of the total number of cells in five areas of 1 mm² each.
*: Mitoses are reported as both the mean and total count of mitotic figures across five areas of 1 mm² each. PT: Primary tumor; HM: Hepatic metastasis; IVC: Inferior vena cava (thrombus); PDX: Patient-derived xenograft; CDX: Cell line-derived xenograft.

In the primary tumor, Ki67 was significantly higher in $p16^{INK4a}$ -negative versus $p16^{INK4a}$ -positive regions ($P < 0.0001$), while the metastases exhibited significantly higher Ki67 levels compared to both regions of the primary tumor ($P < 0.0001$) (Figure 9A). The IVC thrombus, due to its low tumor cellularity, was unsuitable for quantitative analysis.

Mitotic counts and fractions of aberrant mitoses, determined by high-magnification visual analysis of corresponding H&E-stained digital sections, showed a similar pattern. In the primary tumor, average mitotic counts ranged from 11 to 17 in $p16^{INK4a}$ -positive regions and

from 9.4 to 26.8 in $p16^{INK4a}$ -negative regions. Hepatic metastases, again all $p16^{INK4a}$ -negative, displayed elevated mitotic counts ranging from 12.4 to 28.6 (Table 4, Figure 9B).

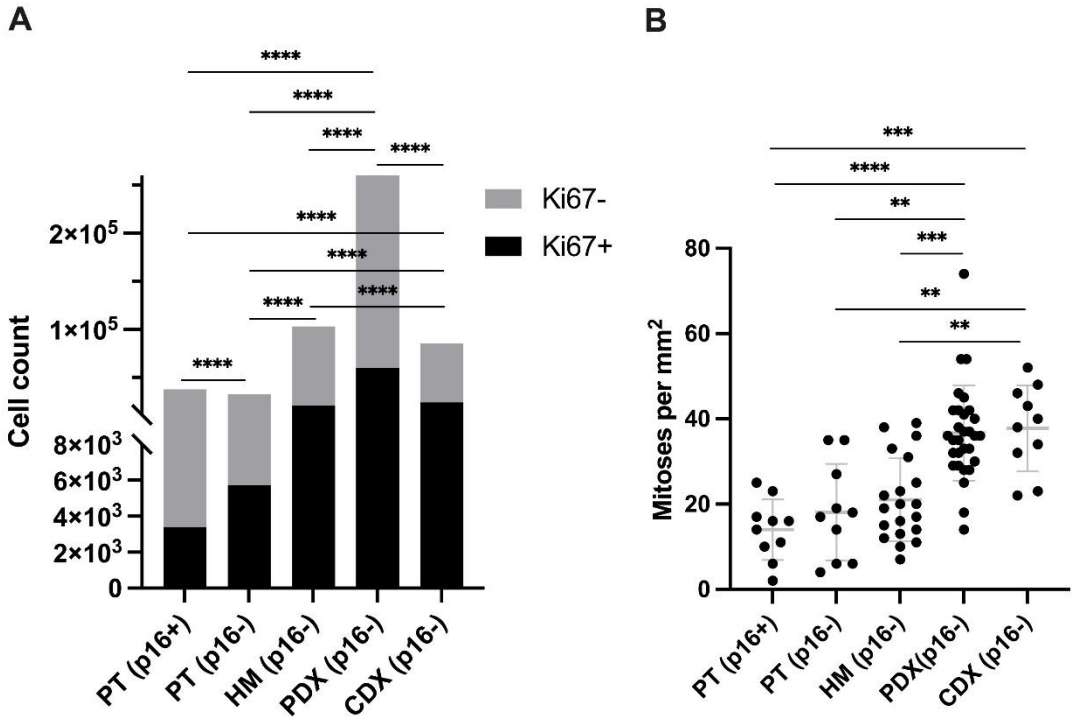


Fig.9. Loss of p16INK4a correlates with increased Ki67 expression and mitotic activity. Ki67 expression (A) and mitotic (B) count are compared among primary tumor (PT) regions demarcated as $p16^{INK4a}$ + and $p16^{INK4a}$ -, hepatic metastases (HM; $p16^{INK4a}$ wholly negative), and patient-derived xenografts (PDX; $p16^{INK4a}$ wholly negative). Values for Ki67 expression and mitotic count were calculated as the mean across sets of five 1 mm² tissue areas. Differences in Ki67 expression were assessed using contingency tables and the χ^2 test, while differences in mitotic count were evaluated using the non-parametric Kruskal–Wallis test followed by post-hoc Dunn's correction. A p value < 0.05 was considered statistically significant.

Although mitotic indexes were generally higher in $p16^{INK4a}$ -negative regions, the differences did not reach statistical significance.

Numerous mitotic figures exhibited aberrations indicative of defective kinetochore–microtubule attachments, including misaligned chromosomes on the metaphase plate, lagging, mal-oriented, bridging, or fragmented chromosomes, as well as mitotic asymmetries. The presence of tri- or tetrapolar spindles further suggested supernumerary centrosomes (Figure 10).

The mitotic aberration burden (MAB) ranged from 43.5 to 49.1 in $p16^{INK4a}$ -positive regions and from 23.9 to 31.9 in $p16^{INK4a}$ -negative regions of the primary tumor, and from 13.5 to 29.2 in hepatic metastases (Table 7).

The absence of a significant correlation between MAB and either primary versus metastatic tumor location or p16^INK4a status indicates that mitotic instability likely represents an early event in tumor initiation, in line with genomic profiling data revealing few small-scale mutations but extensive structural alterations.

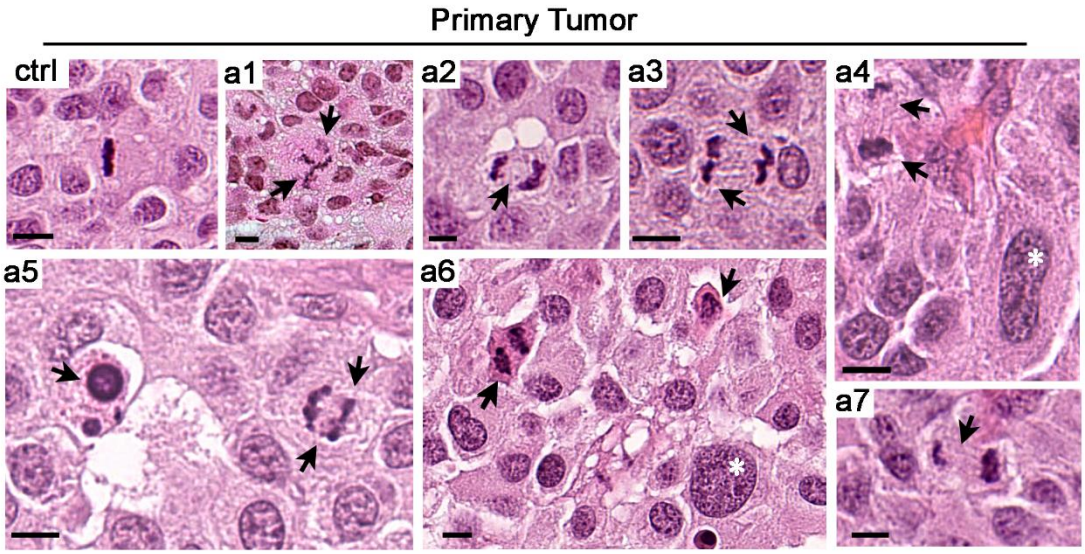


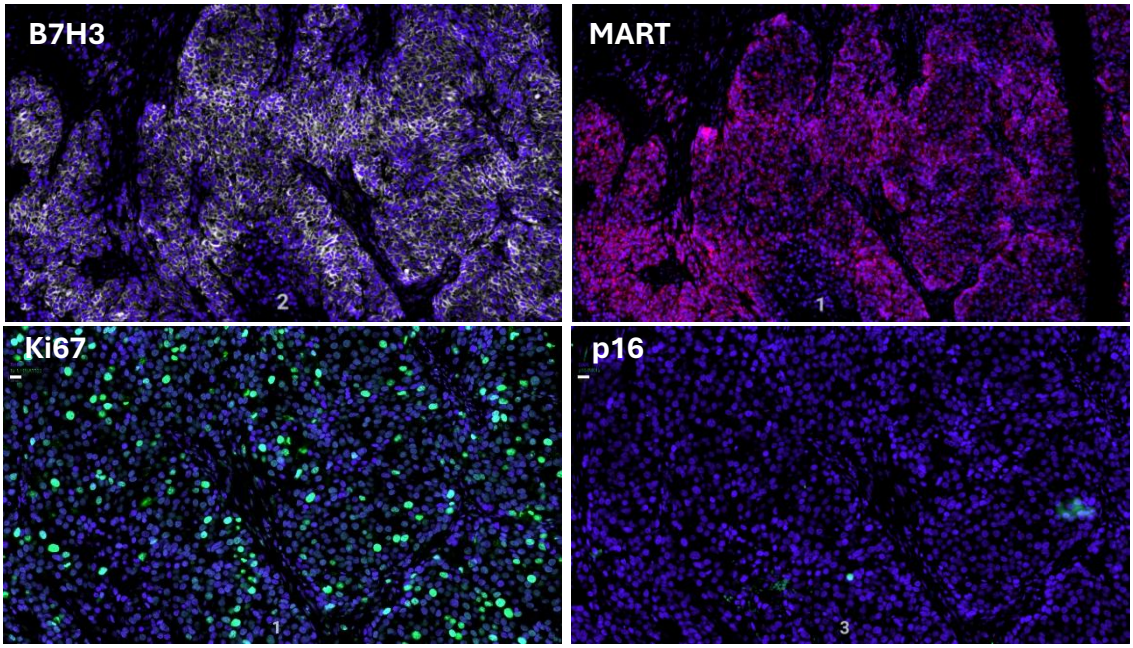
Fig.10. Mitotic figures of the primary tumor displayed aberrations pointing to impaired kinetochore–microtubule attachment probably due to SAC defect(s), such as misaligned chromosomes on the metaphase plate, lagging, mal-oriented, bridging or fragmented chromosomes, and mitotic asymmetries, as well as tri- or tetrapolar spindles. Bars correspond to 5 μm.

MACSima characterization of ACC primary tumor and hepatic metastasis

Multiplex analysis performed using the MACSima platform enabled a detailed phenotypic profiling and spatial characterization of both the p16-negative primary tumor area (PT 1.4.2, Table 7) and the metastatic lesion (HM 1.13, Table 7). In support of this objective, we developed a high-content antibody panel including 33 markers and implemented a tailored analytical workflow to identify the principal immune, stromal, and tumor cell populations**,** revealing differences in tissue organization and tumor microenvironment composition. In particular, the combined use of tumor and immunological markers allowed high-resolution identification of the spatial distribution of cellular populations across distinct tumor regions, distinguishing areas enriched in neoplastic cells from regions characterized by immune infiltrates and stromal components.

Multiplex immunofluorescence analysis revealed distinct expression patterns across tumor regions. Shown here are representative markers investigated in this study. Both the primary tumor and the hepatic metastasis (Figure 11) showed widespread expression of B7 homolog 3 (B7-H3, also known as CD276), an immune checkpoint molecule involved in the regulation of T cell-mediated immune respones, and Melanoma Antigen Recognized by T cells (MART1), a melanocytic differentiation antigen commonly expressed in adrenocortical carcinoma and used as a diagnostic marker, predominantly localized within tumor cell–rich areas and outlining the neoplastic architecture. Ki67 staining identified a high proportion of proliferating cells, indicating marked proliferative activity in both tissues, whereas p16 expression was absent in both lesions, in agreement with the immunohistochemical characterization. Overall, this marker panel enabled the simultaneous evaluation of tumor identity, proliferative status, and immune-related features within the same tissue context.

A-



B

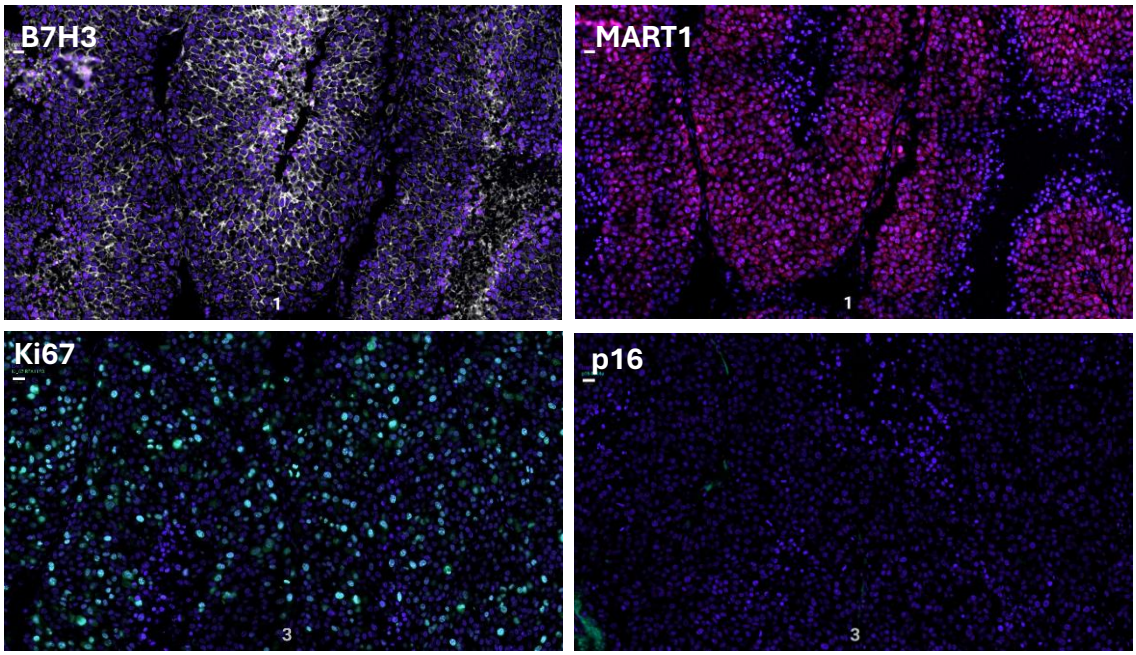


Fig.11. Representative marker expression assessed by MACSima imaging. Representative immunofluorescence images showing the expression of selected markers in p16INK4a- negative primary tumor (PT 1.4.2) and metastatic lesions (HM 1.13). B7-H3; MART1; Ki67; p16. Nuclei are counterstained with DAPI. A: Primary tumor. B: Hepatic metastasis.

In the analyzed samples, the expression profiles of the selected markers are largely maintained in both the primary tumor and the hepatic metastases (Figure 12). In the primary tumors, markers of proliferation and cellular aggressiveness, such as Ki67 and B7-H3, show high expression, while markers associated with epithelial–mesenchymal transition (EMT), such as Vimentin and CD56, and proteins related to epithelial differentiation, here represented by ErbB2/ErbB3, display moderate or variable levels. In hepatic metastases, this general pattern is preserved, with proliferative and differentiation markers expressed at similar or slightly higher levels, whereas some factors linked to cellular plasticity and apoptosis resistance, such as Vimentin, are more intensely expressed. Markers associated with adrenocortical origin as Inhibin, DLL3 and MART1, also show comparable or slightly increased levels. Overall, these findings suggest that metastases retain many features of the primary tumor while exhibiting a slightly more plastic and invasive phenotype, consistent with their role in metastatic progression.

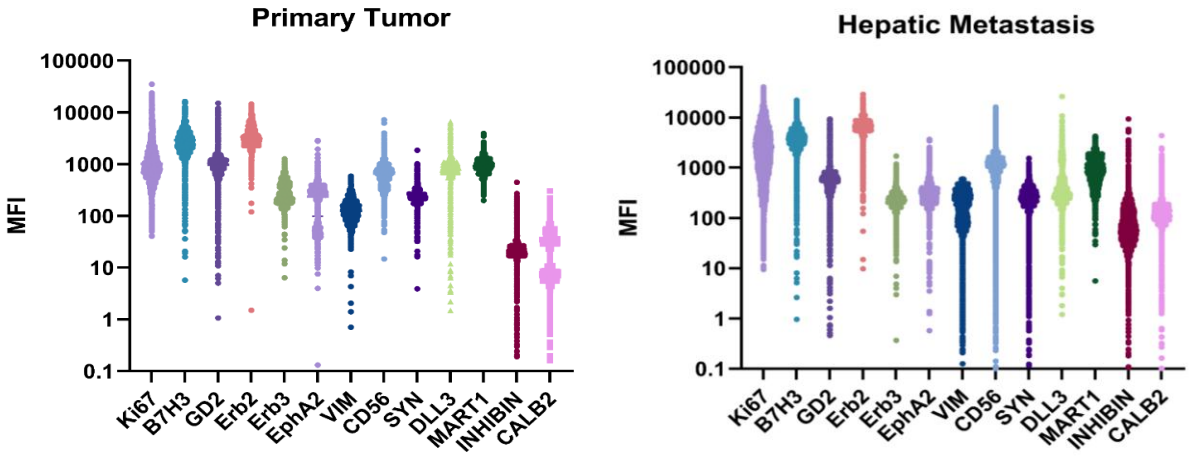
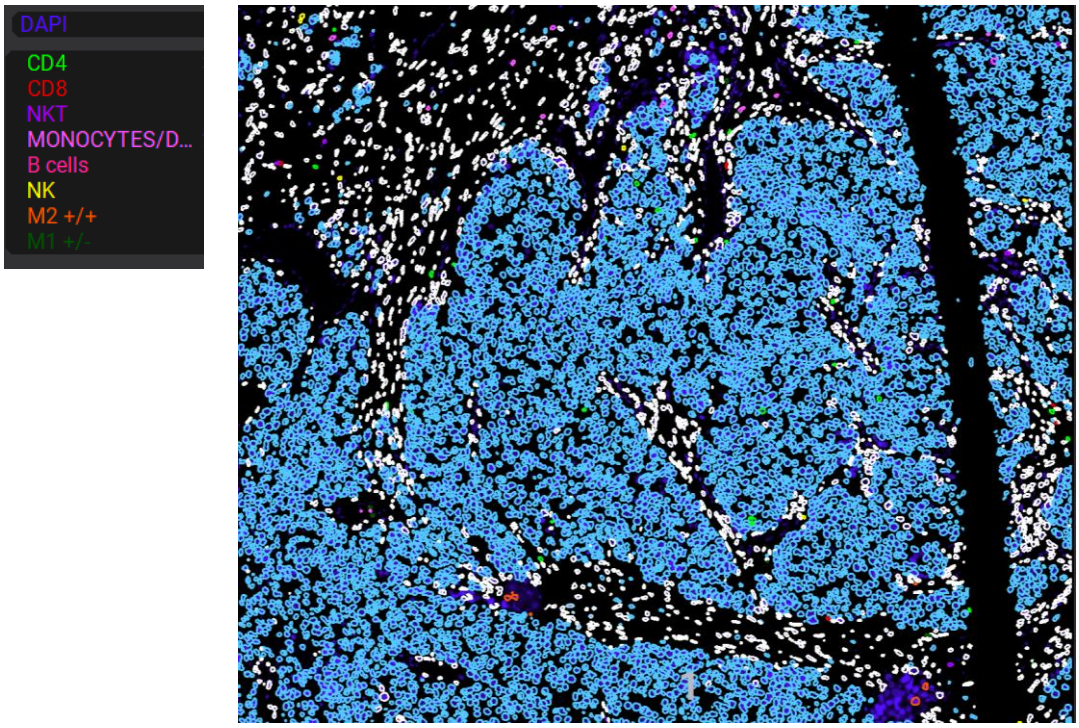


Fig.12. Expression profiles of selected markers in primary tumors and hepatic metastases analyzed by MACSima platform. The graphs show the expression levels of selected markers (Ki67, B7-H3, VIM, CD56, INH, DLL3, MART1) measured as Mean Fluorescence Intensity (MFI) in the primary tumor (left) and hepatic metastasis (right), analyzed by MACSima.

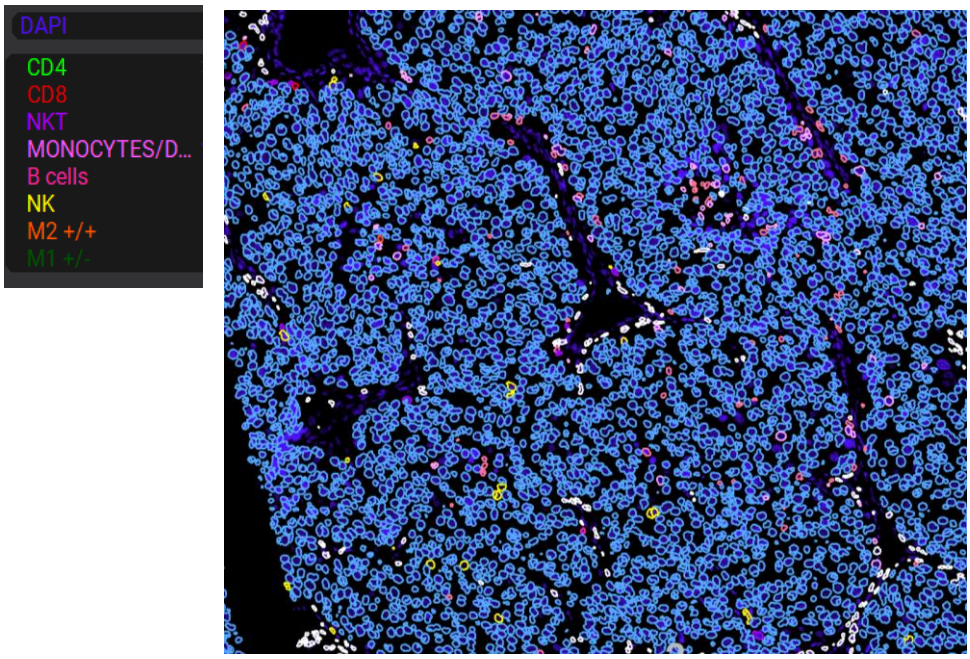
The images shown in figure 13, reveal a clear and well-defined spatial organization of the different cellular populations in both tissues. The tumor compartment is highlighted in light blue, the stromal compartment in white, and, where present, the immune compartment, which includes CD4 and CD8 T lymphocytes, natural killer T (NKT) cells, natural killer (NK) cells,

M1 and M2 macrophages, monocytes, and B cells. The tumor microenvironment of the primary tumor is characterized by a sparse, if not absent, immune infiltrate, with immune cells selectively localized near the invasive front, reflecting the “cold tumor” nature of ACC. In contrast, the metastatic lesion displays a richer immune component, with differences in cell density and spatial distribution and a probable presence of immunosuppressive niches. In this context, immune cells are observed to localize within and around tumor regions, indicating lymphocytic infiltration and active recruitment toward tumor foci. Overall, these findings suggest a slightly more immunologically active tumor microenvironment in the metastasis, while the primary tumor appears to be largely devoid of immune cell infiltration.

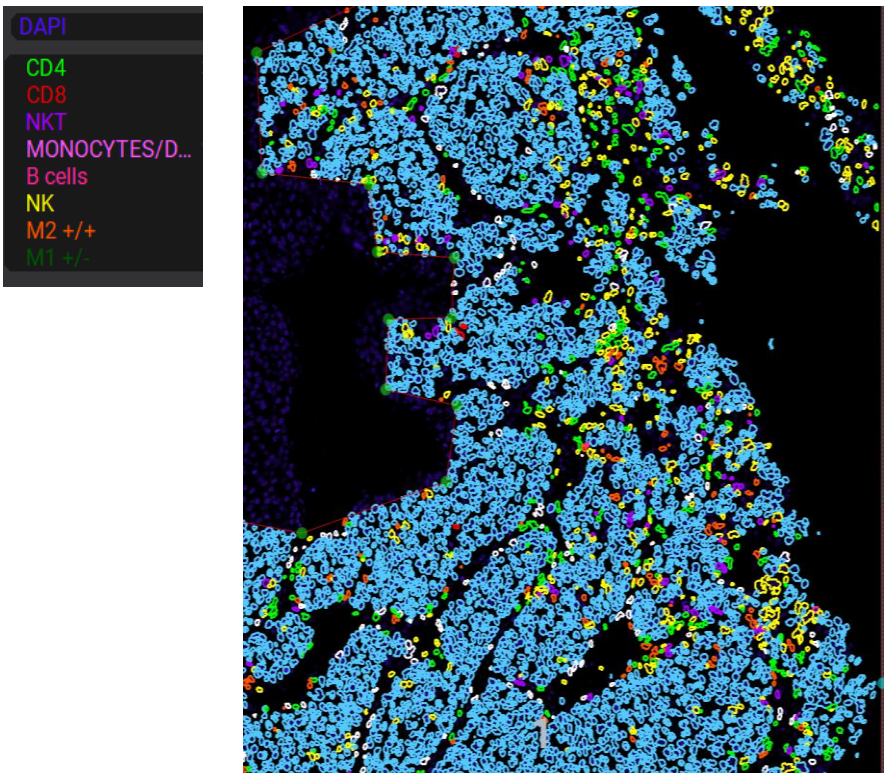
A- Primary tumor



B- Primary tumor



C- Hepatic metastasis



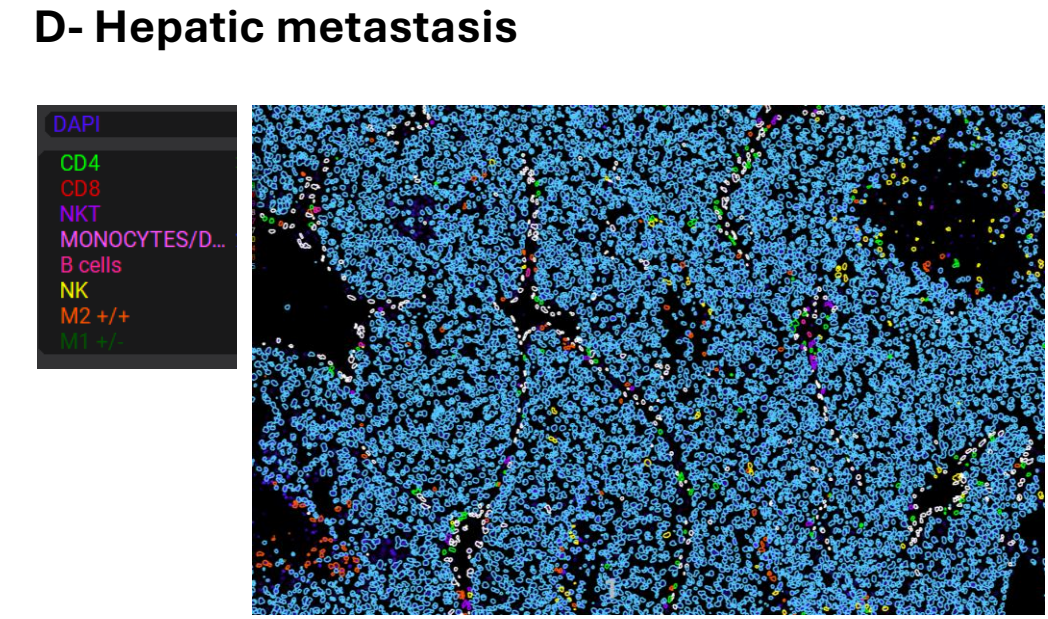


Fig.13. Distribution and organization of the tumor microenvironment (TME) in ACC primary tumor and hepatic metastasis samples. Representative multiplex images show regions of tumor compartment Immune populations, including $CD8^+$ T cells, $CD4^+$ T cells, NKT cells, M1 and M2 macrophages, B cells and NK cells as well as stromal components, are also highlighted. A,B: primary tumor. C, D: hepatic metastasis.

The relative abundance of the main immune cell populations was quantified in the primary tumor (PT) and in the corresponding liver metastasis (Met) (Figure 14). Overall, immune populations were present at low frequencies in both samples, with notable differences between PT and Met. T cells were detected at a low percentage in the primary tumor and showed a modest increase in the metastatic sample. B cells were nearly absent in both PT and Met. NKT cells were present at very low levels, with a slight enrichment in the metastasis compared to the primary tumor. NK cells were minimally represented in the primary tumor but displayed a clear increase in the metastatic lesion. Among all populations, myeloid cells constituted the most abundant compartment, showing a marked enrichment in the metastasis relative to the primary tumor. Overall, the low abundance of lymphoid populations observed in both tissues indicates a poorly immune-infiltrated tumor microenvironment, consistent with the cold tumor phenotype typically associated with adrenocortical carcinoma.

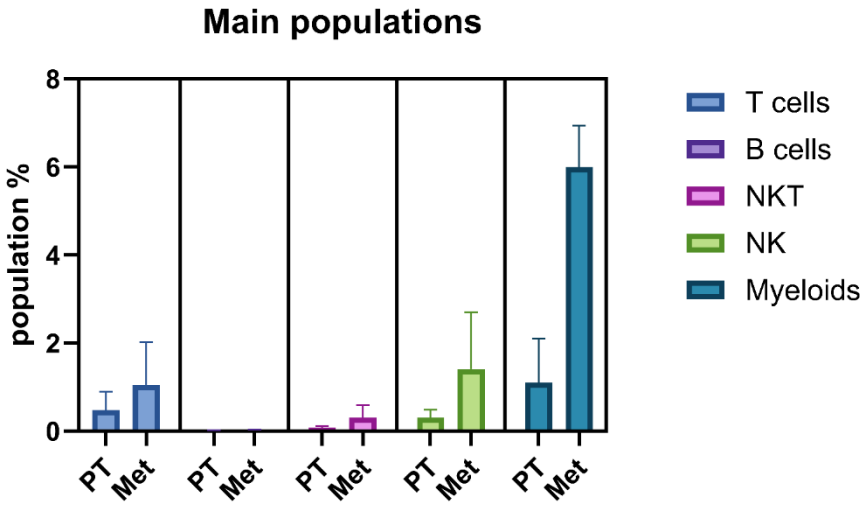


Fig. 14. percentage distribution of the main cellular populations across the analyzed samples. PT: Primary Tumor. Met: Hepatic metastasis. The legend relative to the immune populations is shown on the right.

Data analysis carried out with the MACSima Analyzer allowed an in-depth assessment of tumor spatial architecture and yielded insights into the unique characteristics of the ACC tumor microenvironment.

Establishment and characterization of in vitro and in vivo models

Two million cells derived from the primary ID7ACC culture were used to generate cell line–derived xenografts (CDXs ID7) in female NSG mice via subcutaneous injection into the upper flank region. Early-passage patient-derived xenografts (PDXs) established in female NSG mice were employed as faithful experimental models to study the evolution of $p16^{INK4a}$ + and $p16^{INK4a}$ – primary tumor subpopulations derived from the parental tumor. Subcutaneous xenografts were successfully generated from all serial transplantations across subsequent generations (16/16, 100%; F1: 4/4; F2: 8/8; F3: 4/4) (Figure 15), with an average of 38 days required to reach the predefined harvest diameter of 15 mm. Additional adrenocortical carcinoma (ACC) cell lines were derived from metastatic lesion, PDXs and CDX. These cell

lines were derived from a primary tumor, a metastatic lesion, a xenograft, and a cell line–derived xenograft (CDX), respectively

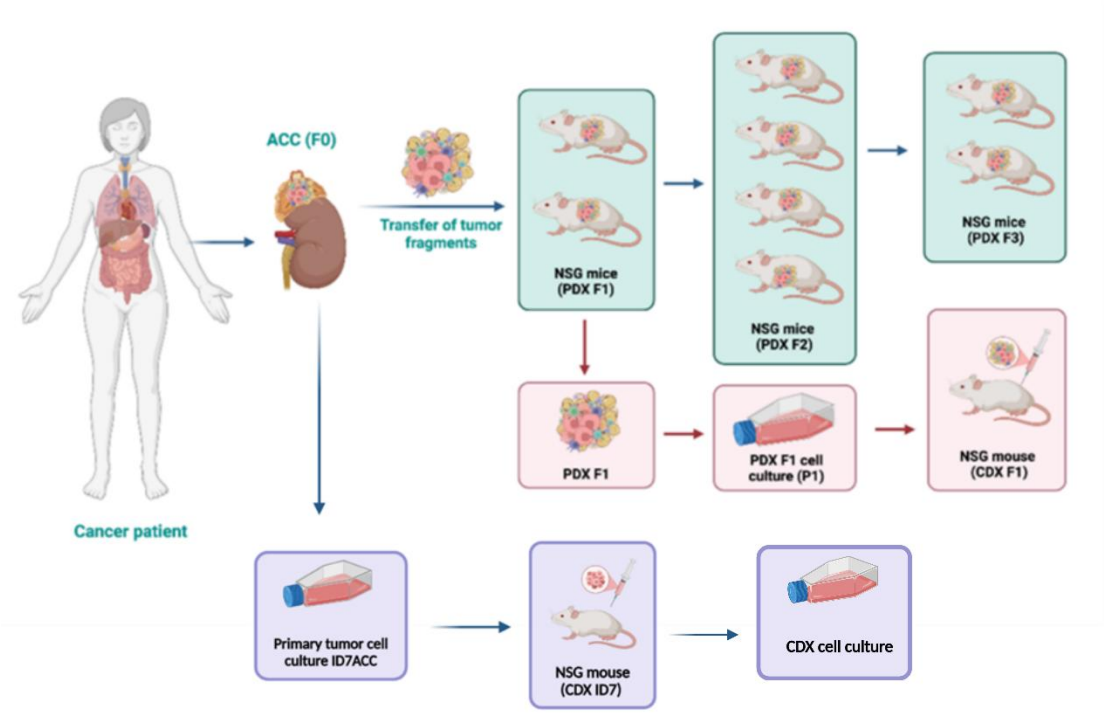


Fig.15 Schematic workflow for the generation of xenografts. Patient-derived (PDX) and cell-derived (CDX) ACC xenografts were generated and serially propagated across early passages (F1–F3), preserving key characteristics of the parental tumors. PDXs were used for downstream pathological analyses or for the generation of CDXs. Procedure details are described in Materials and Method section.

Morphological and proliferative stability of ID7 ACC cell model

Throughout the experimental work, the ID7ACC cell line was maintained in continuous culture up to passage 50 in order to monitor cell viability, morphological stability, and proliferative capacity over time. Cells were cultured in Advanced DMEM supplemented with specific growth factors under standard incubation conditions (37 °C, 5% CO_2, controlled humidity).

Across successive passages, the cell line exhibited regular and sustained growth, with no evidence of proliferative slowdown or alterations in confluence rate. In parallel, cells preserved

a stable morphology characterized by a high degree of homogeneity across the observed fields. The persistence of the original morphological features over multiple passages suggests a stable adaptation to the culture conditions.

Notably, the ID7ACC cell line continued to proliferate well beyond the number of passages typically compatible with a primary cell culture, without displaying signs of senescence or loss of adhesion. This behavior is indicative of a potential spontaneous immortalization process, a hypothesis further supported by the maintenance of both morphological characteristics and proliferative capacity following numerous subculturing cycles.

Evaluation of Hormone Secretion Profiles of ID7ACC cell model

In this study, hormone production by the ID7ACC cell line was evaluated under the established culture conditions, with HeLa cells included as a negative control. Although widely used in experimental research, HeLa cells lack steroidogenic capacity and are unable to produce steroid hormones. The inclusion of this negative control was essential to confirm that the hormone levels detected in the experimental setup originated specifically from the ID7 ACC cells. This approach allowed the exclusion of any potential background contributions from the culture medium or methodological artifacts, ensuring that the observed steroidogenesis could be reliably attributed to the intrinsic tumoral activity of the ID7 ACC cell line.

Analysis of ID7ACC cultures grown in DMEM Advanced revealed measurable hormone production across multiple classes involved in steroidogenesis (Figure 16). The cells exhibited robust androgen secretion, with androstenedione showing particularly high levels, while testosterone was present at lower, yet detectable concentrations.

Regarding progestins, progesterone production was undetectable; however, 17-hydroxyprogesterone (17-OHP) was synthesized by the cells, albeit at lower levels than androstenedione. This reduced production may reflect limitations in precursor availability or suboptimal culture conditions insufficient to fully support progestin steroidogenesis.

Mineralocorticoid synthesis appeared markedly impaired, as corticosterone was undetectable under these culture conditions. This suggests a limited capacity of ID7ACC cells to produce

mineralocorticoids in DMEM Advanced, potentially due to insufficient stimulation or inadequate supply of necessary precursors and nutrients.

In contrast, glucocorticoid production was appreciable: both 11-deoxycortisol and cortisol were detected at measurable concentrations, confirming active glucocorticoid synthesis. Control experiments using cell-free medium confirmed that these hormones were produced by the cells rather than being present in the culture medium.

Overall, these results indicate that ID7ACC cells retain active steroidogenic capacity, with a preference for androgen and glucocorticoid production, while progestin and mineralocorticoid synthesis appears constrained under the current culture conditions.

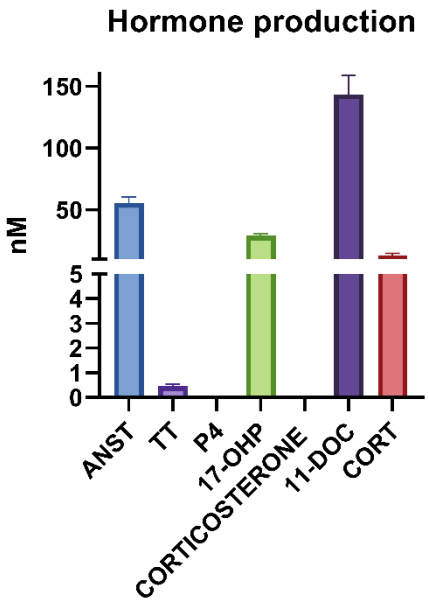


Fig. 16. Quantification of hormone concentrations (nM) under experimental conditions (Advanced DMEM). The x-axis indicates: ANST, androstenedione; TT, testosterone; P4, progesterone; 17-OHP, 17-hydroxyprogesterone; Corticosterone; 11-DOC, 11-Deoxyicortisol; CORT, Cortisol.

To assess whether the experimental model recapitulates the characteristics of the original tumor, including steroid hormone production, a comparison was performed between the patient's plasma hormone profile and the hormone secretion of the ID7 cell line. The patient presented with a functioning adrenocortical carcinoma, characterized by hypersecretion of glucocorticoids and androgens: elevated cortisol and Urinary Free Cortisol (UFC) levels, lack of suppression in the dexamethasone test, and decreased Adrenocorticotropic hormone (ACTH) indicated autonomous, ACTH-independent hormone production. Concurrently, increased 17-

hydroxyprogesterone (17-OHP), Dehydroepiandrosterone sulfate (DHEA-S), androstenedione, and testosterone levels reflected co-secretion of androgens and steroid precursors. The ID7 cell line reproduced this phenotype, displaying active steroidogenesis with simultaneous production of androgens (androstenedione, testosterone), progestins (17-OHP), and glucocorticoids (cortisol), consistent with the patient's hormone profile (Table 8).

HORMONES	PRE- SURGERY	POST- SURGERY	PLASMA REFERENCE RANGE	CELL LINE
DHEA-S	**272.4 ug/dl**	**487.0 ug/dl**	30-182 ug/dl	-
17-OHP	**4.3 ng/ml**	**388.5 ng/ml**	0.08-1.3 ng/ml	**Secreting**
TT	0.3 ng/ml	**9.9 ng/ml**	0.1-0.57 ng/ml	**Secreting**
ANST	2.10 ng/ml	**18.2 ng/ml**	0.3-10 ng/ml	**Secreting**
CORT	298.5 nmol/l	**696.2 nmol/l**	101-536 nmol/l	**Secreting**
ACTH	17.3 pg/ml	6.8 pg/ml	4.7-48.8 pg/ml	-
UFC	49.96 ug/24 h	**432.0 ug/24 h**	4.30-176 ug/24 h	-
ALD	13.8 pg/ml	-	17.6-232 pg/ml	-
PRA	0.05 ng/ml/h	-	0.06-4.69 ng/ml/h	-
UFM	0.14 mg/24 h	-	0.05-0.34 mg/24 h	-
NMN	0.18 mg/24 h	-	0.08-0.45 mg/24 h	-
DST 1MG	**183.9 nmol/l**	-	<50 nmol/l	-
PROGESTERONE	-	-	-	-
CORTICOSTERONE	-	-	-	-
11-DOC	-	-	-	**Secreting**

Table 8. Comparative overview of key hormone parameters measured before and after surgery, including reference ranges and values observed in the model cell line. DHEA-S: Dehydroepiandrosterone sulfate, 17-OHP: 17-hydroxyprogesterone, TT: Total testosterone, ANST: Androstenedione, CORT: Cortisol, ACTH: Adrenocorticotropic hormone, UFC: Urinary free cortisol, ALD: Aldosterone, PRA: Plasma renin activity, UFM: Urinary free metanephrines, NMN: Normetanephrine, 11-DOC: 11-deoxycorticosterone.

Flow cytometric phenotypic characterization of ACC cell lines

To phenotypically characterize adrenocortical carcinoma (ACC) cell lines, a panel of markers was analyzed to assess immune modulation, differentiation status, membrane organization, and activation of proliferative signaling pathways. The analysis was performed on cell lines derived from primary ACC tumors, metastases, xenografts, CDX models, as well as the H295R and SW13 cell lines (Fig. 17). Across all analyzed cell lines, high expression of B7-H3 was consistently observed, representing the most uniformly and highly expressed marker among all models. DLL3 and CD81 were identified as the next most highly expressed markers, although at lower levels compared to B7-H3. In contrast, CD56 displayed variable expression across the different cell lines. CD73, GD2, EGFR, and FGFR were expressed at low levels in all analyzed models. Similarly, the remaining markers included in the panel were generally low or negative, with an MFI ratio below 2, which was defined as the threshold to discriminate between marker positivity and negativity, with the exception of a limited number of cases and the SW13 cell line, in which these markers were highly expressed.

Given the consistently high expression of B7-H3 across all ACC cellular models analyzed, this marker was selected as the target for subsequent CAR T cell generation and functional killing assays.

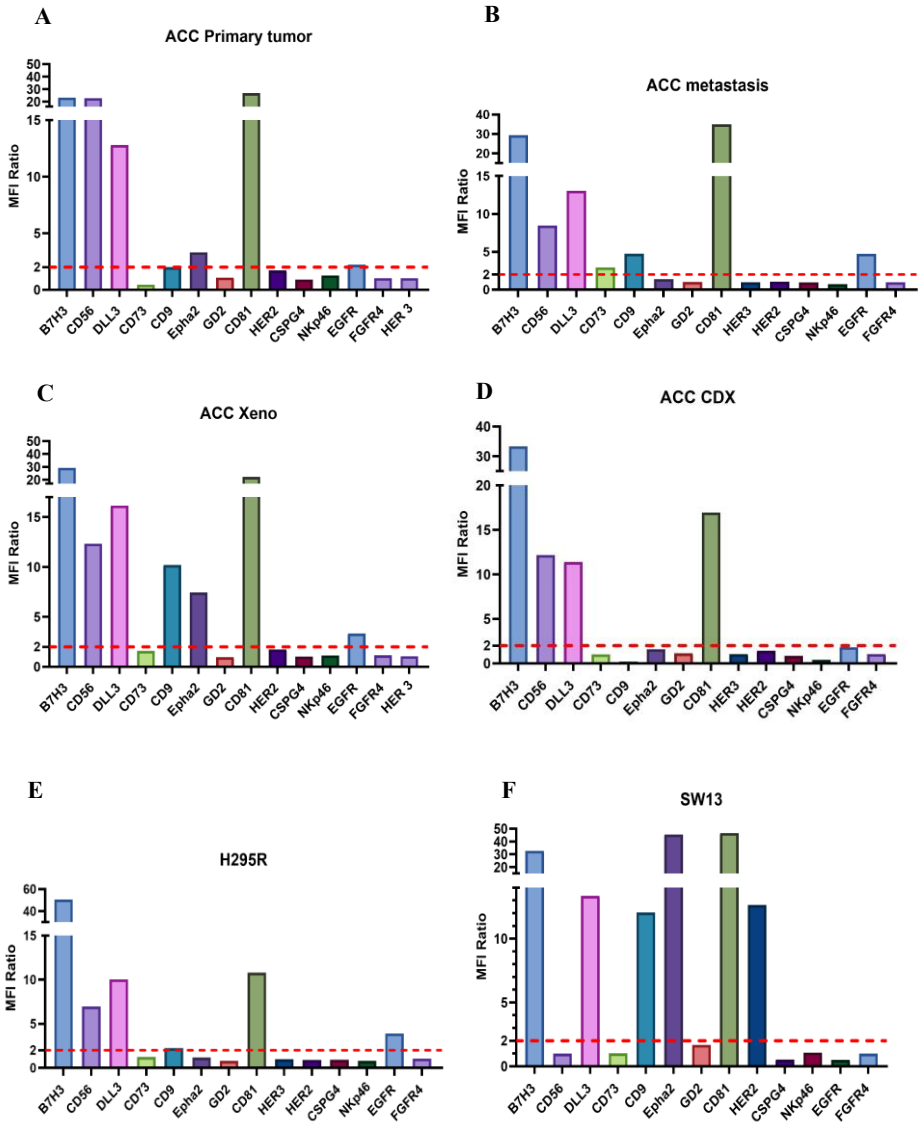


Fig. 17. Immunophenotypic characterization of ACC cell lines by flow cytometry. Quantitative analysis of immune marker expression in established ACC cell lines. The red dashed line indicates the MFI threshold, with values < 2 considered negative and values > 2 considered positive.

Integrated histopathological and immunophenotypic characterization of the ID7 CDX model

The CDX model generated from the ID7ACC cell line exhibited heterogeneous and overall reduced synaptophysin (SYP) and inhibin (INH) immunopositivity compared to the primary tumor. In contrast, a strong immunoreactivity was observed for markers such as calbindin-2 and Melan-A, recapitulating an immunophenotypic profile consistent with that of the primary tumor. Notably, Melan-A expression, which plays a key role in distinguishing primary adrenocortical carcinoma from metastatic lesions, was robustly maintained in the CDX model (Fig. 19).

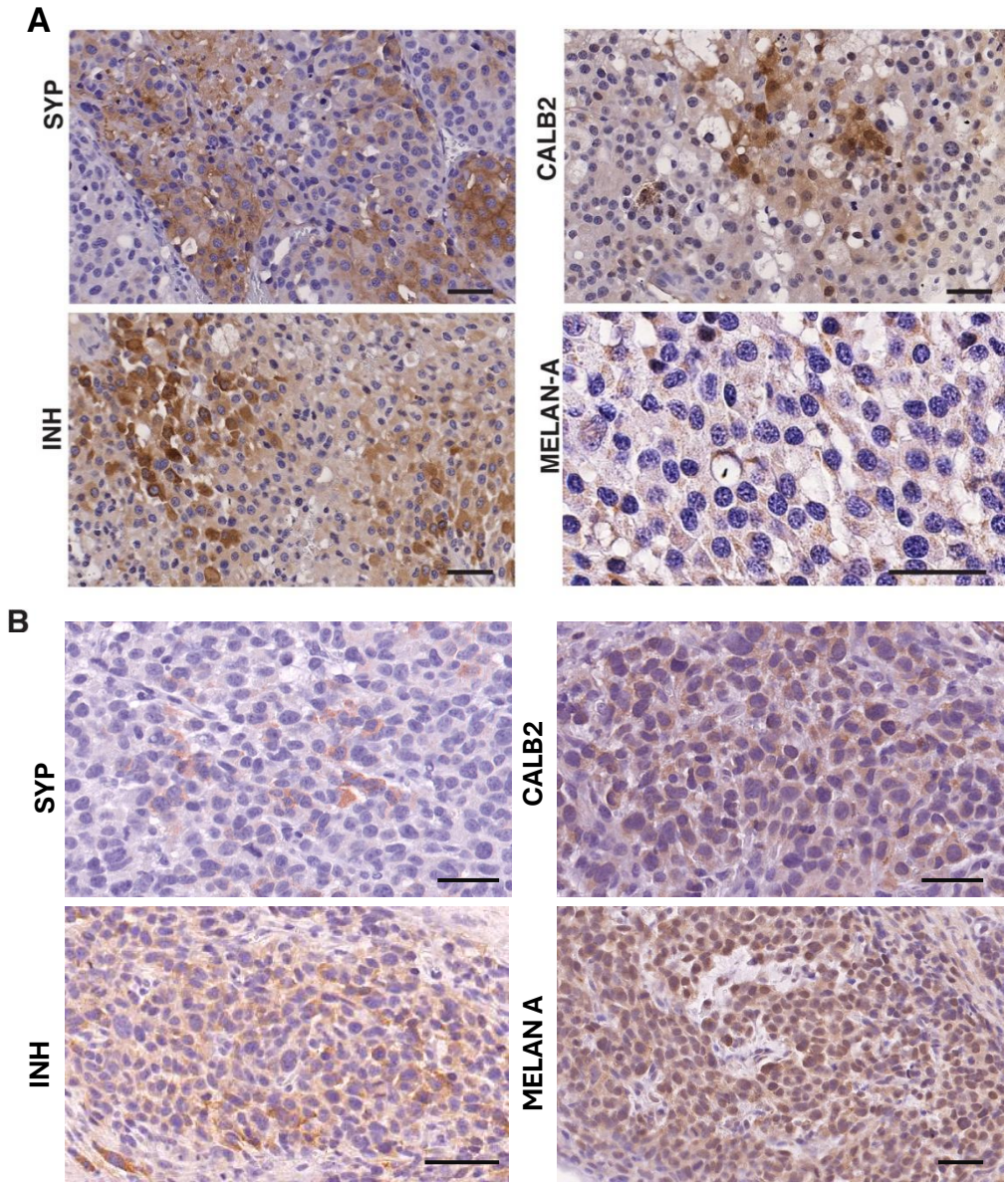


Fig. 19. Histopathological and immunohistochemical comparison of resected primary tumor and CDX from ID7 Cell line model. (A) Primary Tumor: The primary lesion demonstrates well-defined focal immunoreactivity for synaptophysin (SYP), calbindin 2 (CALB2), and alpha-inhibin (INH), alongside a mosaic expression pattern for MELAN-A. All scale bars in panel A represent 50 μm.
(B) CDX model from ID7 cell line model: Immunohistochemistry shows focal and light positivity for SYP and INH; it exhibits stronger immunopositivity for CALB2 and MELAN-A.

Digital image analysis of $p16^{INK4a}$ immunostaining was performed on FFPE sections of the CDX model generated from the ID7ACC cell line. This analysis revealed a predominantly $p16^{INK4a}$ -negative tumor cell population, while Ki67 immunoreactivity was preserved. Overall,

these findings indicate that the CDX model retains an immunophenotypic profile comparable to that of the corresponding primary tumor (Figure 20).

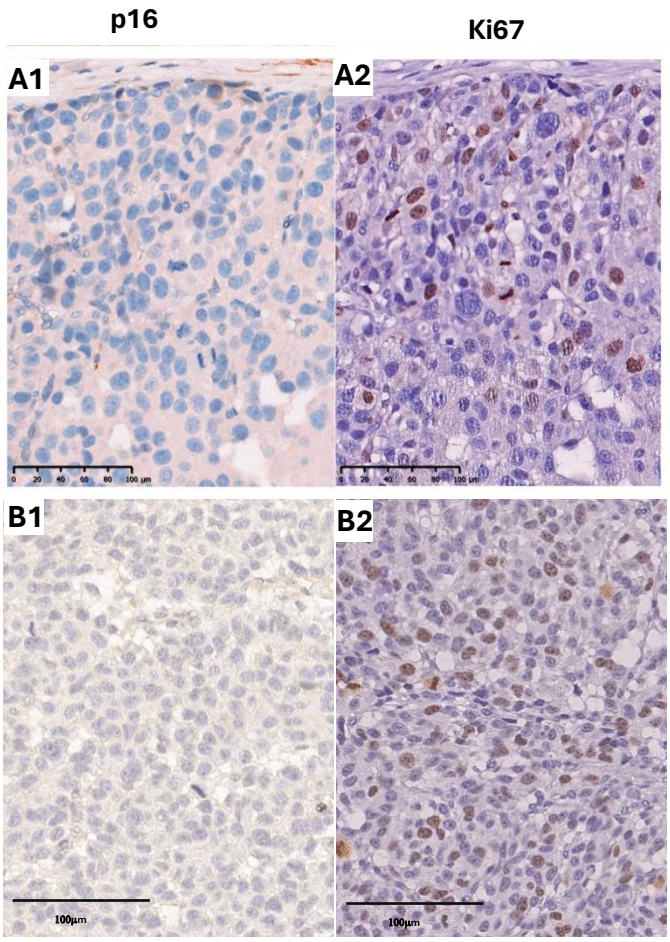


Fig.20. Digital Image Analysis of p16INK4a and Ki67 Immunostaining.
(A) Representative FFPE sections of the primary tumor showing a p16^INK4a-negative area (A1) and Ki67 positivity (A2). (B) Sections from the CDX model display a complete absence of tumor-associated $p16^{INK4a}$ expression (B1), while Ki67 immunoreactivity is preserved (B2). All scale bars in panel A represent 100 µm.

Histopathological and ultrastructural characterization of PDX and CDX models

A passage 1 culture derived from an F1 PDX was used to generate CDXs in female NSG mice by subcutaneous injection of 2×10^6 cells into each upper flank region (total of 4×10^6 cells. It

resulted in the rapid growth of one CDX, which reached the predefined harvest diameter of 1.5 cm within 41 days. In all cases, both the PDXs and the derived CDXs faithfully recapitulated the histological, immunohistochemical, and ultrastructural features of the parental tumor (Figure 21).

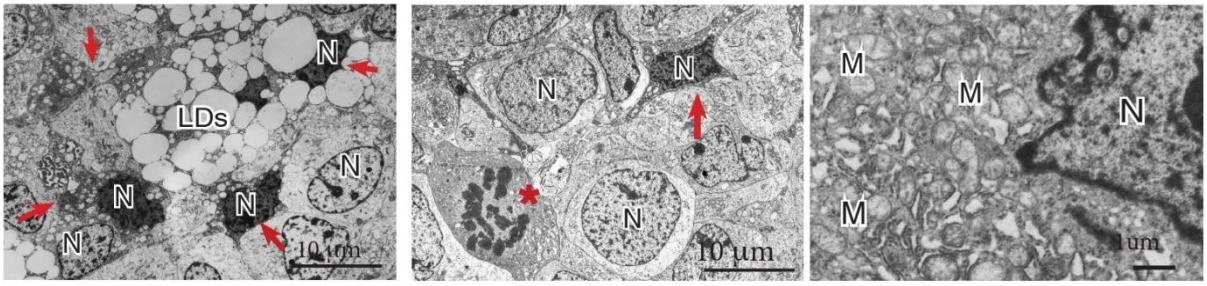


Fig. 21. Ultrastructural analysis of patient-derived xenograft (PDX) via Transmission Electron Microscopy (TEM). The PDXs faithfully replicated ultrastructural features of the parental tumor. Diffuse growth, high nuclear grade, prominent nucleoli, and incorporation of two ultrastructural cell morphotypes, i.e., larger clear cells (~70%) and thinner, electron-dense cells with filopodia (<30%). As in the parental tumor, the cells contained prominent endoplasmic reticulum and abundant swollen mitochondria. A prometaphase, distinguished by the breakdown of the nuclear envelope, which allows spindle microtubules to access the nuclear area, is evident (central image, cell marked with red asterisk).

Macroscopic examination and necropsy, corroborated by histological analysis of FFPE organ sections, revealed no evidence of metastatic dissemination in any of the 16 PDX-bearing mice, while the CDX-bearing mouse exhibited extensive metastatic involvement of the abdominal and thoracic compartments. The lesions comprised a large liver metastasis occupying the majority of the left hepatic lobe, indicative of hematogenous spread; multiple peritoneal tumor nodules attributable to secondary transcoelomic dissemination, including two attached to the Glisson's capsule and one to the splenic capsule; and metastatic infiltrates of the visceral pleura of the left lung, consistent with transdiaphragmatic lymphatic spread. The sizable intrahepatic metastasis likely represented the primary source of tumor cell shedding into the peritoneal cavity via the Glisson's capsule, thus contributing to the observed pattern of peritoneal spread (Figure 22).

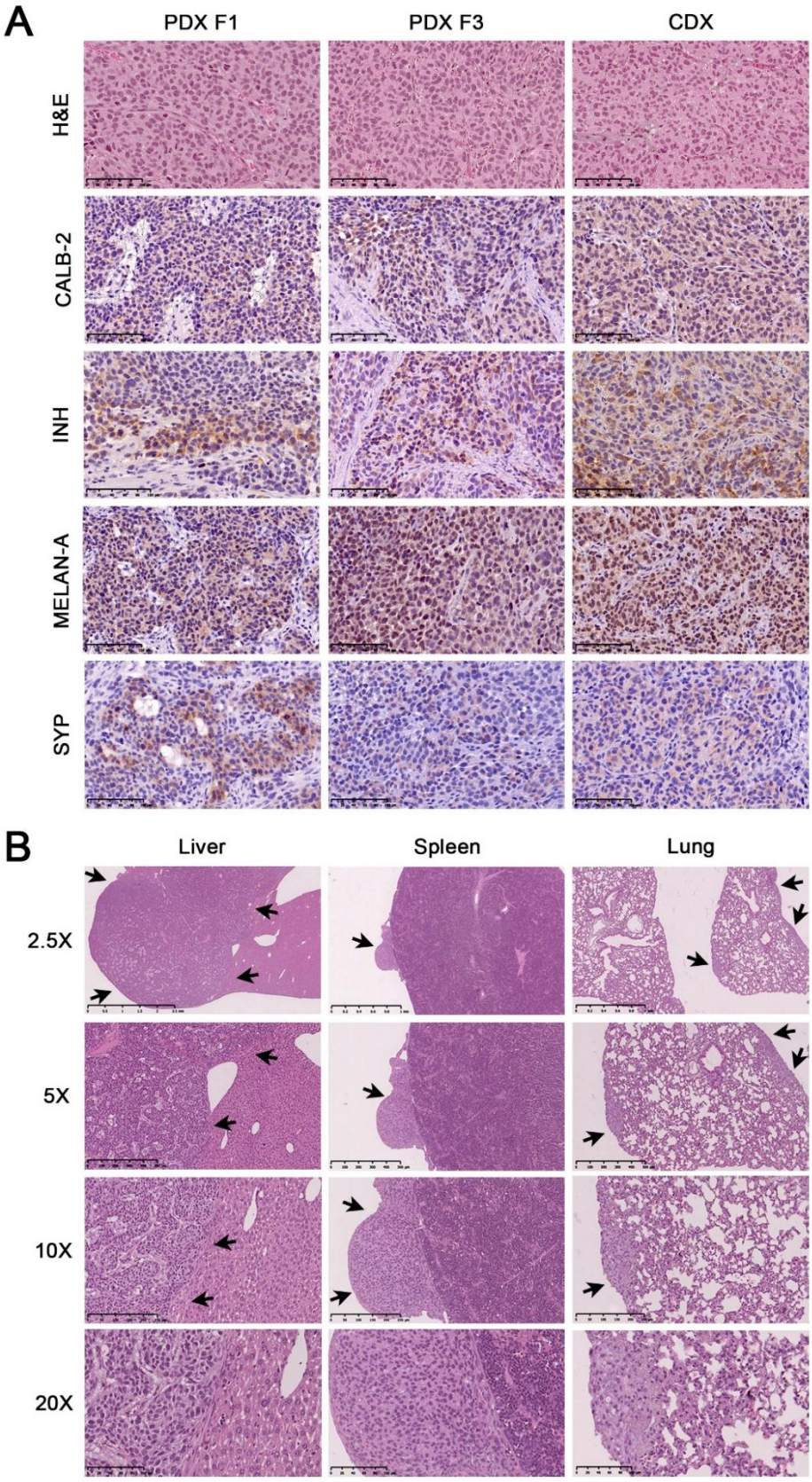


Fig. 22. Xenografts (patient and cell-derived, PDXs and CDX) and metastases from the CDX-bearing mouse.

A: Comparative histology and immunohistochemistry of first (F1) and third (F3) generation PDXs and of a CDX. Invariably, hematoxylin and eosin (H&E) staining shows sheets of large cohesive cancer cells supported by abundant and relatively thin fibrovascular septa, as found in the primary and metastatic lesions resected from the patient. As the parent (patient) tumor, the F1 and F3 PDXs and the CDX show immunoreactivity for calbindin 2 (CALB2), inhibin A (INH), and Melan-A (MELAN-A), while synaptophysin (SYP) is mainly evident in the F1 PDX. Scale bars: 100 µm.
B: progressive magnifications of hematoxylin and eosin (H&E)-stained sections of metastases from the CDX-bearing mouse. Liver: intrahepatic metastasis. Most of the left lobe of the liver is replaced by a tumor mass composed of cells like those found in the CDX, except for wider supporting fibrovascular septa. Spleen: metastatic implant on the splenic capsule after transcoelomic seeding. There is no evidence of supportive fibrovascular septa. Lungs: At least three areas of thickening are visible on the pleura of the left lung in this section plane (arrows). Higher magnifications reveal poorly vascularized cancer cells infiltrating underlying lung tissue. Scale bars: first row, 1 mm; second row: 500 µm; third row: 250 µm; fourth row: 100 µm.

Sections from all PDXs and the CDX, as well as from the abdominal and pleural metastases of the CDX-bearing mouse, were stained for $p16^{INK4a}$ and evaluated by digital image analysis. Both PDXs and the CDX were predominantly $p16^{INK4a}$- (approximately 90% of tumor cells); however, in all cases, discrete tumor cell subpopulations with strong nuclear p16^INK4a positivity were consistently observed, preferentially localized at the tumor periphery or in perivascular regions. No appreciable differences in the extent or distribution of $p16^{INK4a}$ expression were detected across passages (F1–F3) or between PDXs and the CDX (Figure 23 A, B). In contrast, all abdominal and pleural metastases identified in the CDX-bearing mouse were entirely negative for $p16^{INK4a}$ expression (Figure 23 B).

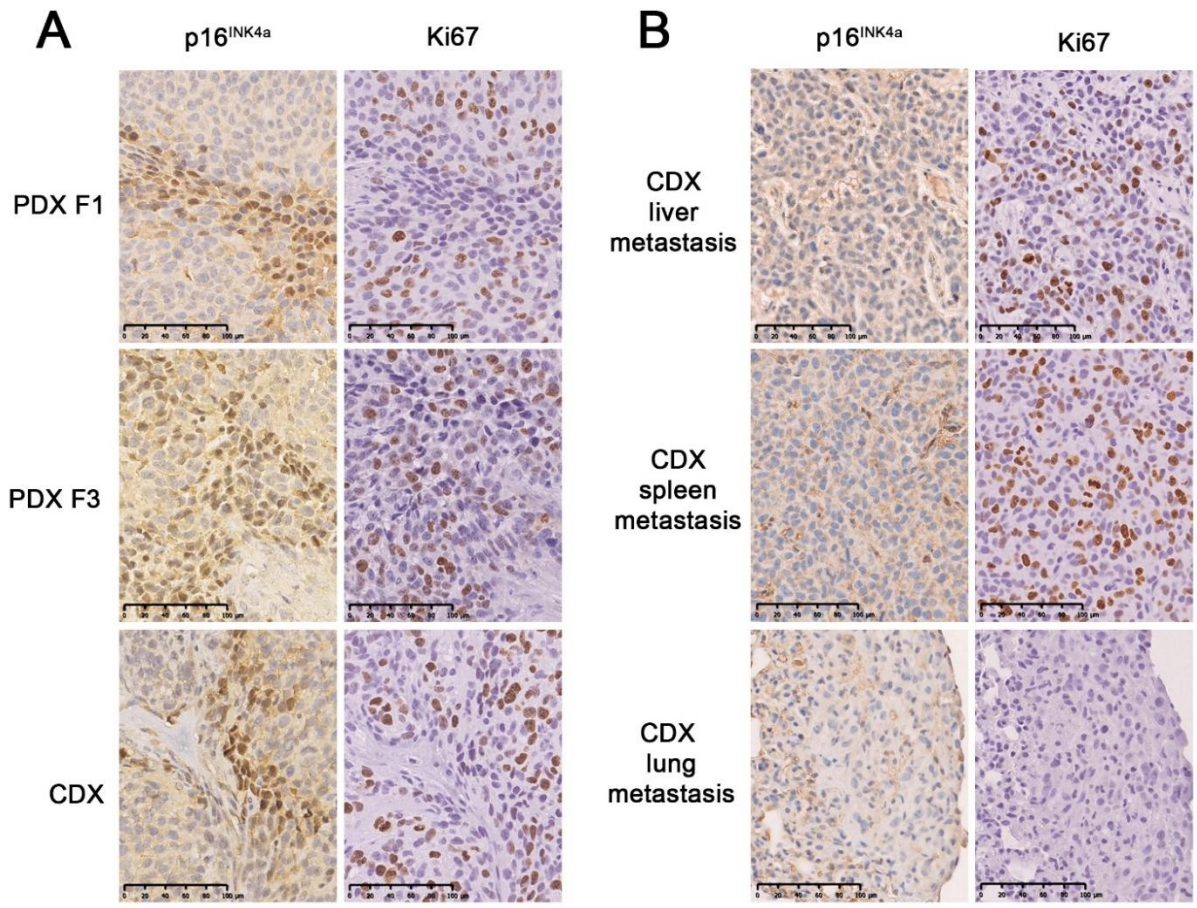


Fig.23. Comparative p16INK4a and Ki67 immunostaining in first (F1) and third (F3) generation PDXs and in the CDXs. A: in the PDXs and CDXs $p16^{INK4a}$ nuclear labeling is mainly evident in tumor cells adjacent to fibrovascular septa, while strong Ki67 positivity is evident in most tumor cells distant from septa. B: Sections of liver, spleen and pleural metastases from the CDXs-bearing mouse do not show $p16^{INK4a}$ nuclear labeling, excepting rare stromal cells of likely murine origin. Ki67 labeling is very strong and diffuse, except for the pleural metastasis, where low proliferative activity could reflect early and poorly vascularized metastatic colonization. Bars: 100 µm.

.

Ki67 labeling indexes, mitotic indexes (MIs), and mitotic aberration burdens (MABs) were quantified as previously described in sets of five 1 mm² regions of interest selected exclusively from the $p16^{INK4a}$ -negative areas of each xenograft due to the scarcity of $p16^{INK4a}$ -positive regions. The mean Ki67 indexes ranged from 9.03 to 34.0, while mitotic indexes varied from 25.8 to 47.4 across the analyzed samples (Table 7). No statistically significant differences were detected among the F1, F2, and F3 passages, nor between PDXs and the CDX.

Overall, xenografts (PDXs and CDX) exhibited significantly higher Ki67 labeling indexes than both $p16^{INK4a}$ -positive and $p16^{INK4a}$ -negative regions of the primary tumor ($P < 0.0001$ for both comparisons), as well as than metastatic lesions ($P < 0.0001$) (Figure 9A, Table 7). Consistently, mitotic indexes were markedly increased in xenografts compared with $p16^{INK4a}$ -positive and $p16^{INK4a}$ -negative areas of the primary tumor ($P < 0.0001$ and $P = 0.0008$, respectively) and with $p16^{INK4a}$ -negative liver metastases ($P = 0.0002$) (Figure 9B, Table 7).

In the metastatic lesions identified in the CDX-bearing mouse, quantitative evaluation of Ki67 labeling was as high as that observed in the patient's hepatic metastases, consistent with their shared p16INK4a-negative status (29.3 vs 20.0). Notably, the pleural lesions lacked detectable Ki67 immunoreactivity, indicating low proliferative activity consistent with early-stage, poorly vascularized metastatic growth (Figure 23 B). Mitotic aberration burdens (MABs) were highest in the xenografts, including both PDXs and the CDX (Figure 24). However, no statistically significant differences were observed when comparing MAB values across $p16^{INK4a}$ -positive and $p16^{INK4a}$ -negative regions of the primary tumor (ranges: 43.5–49.1 and 23.9–31.9, respectively), hepatic metastases (range: 13.5–29.2), PDXs (range: 13.4–39.5), and the CDX (11.6-40.1) (Table 7).

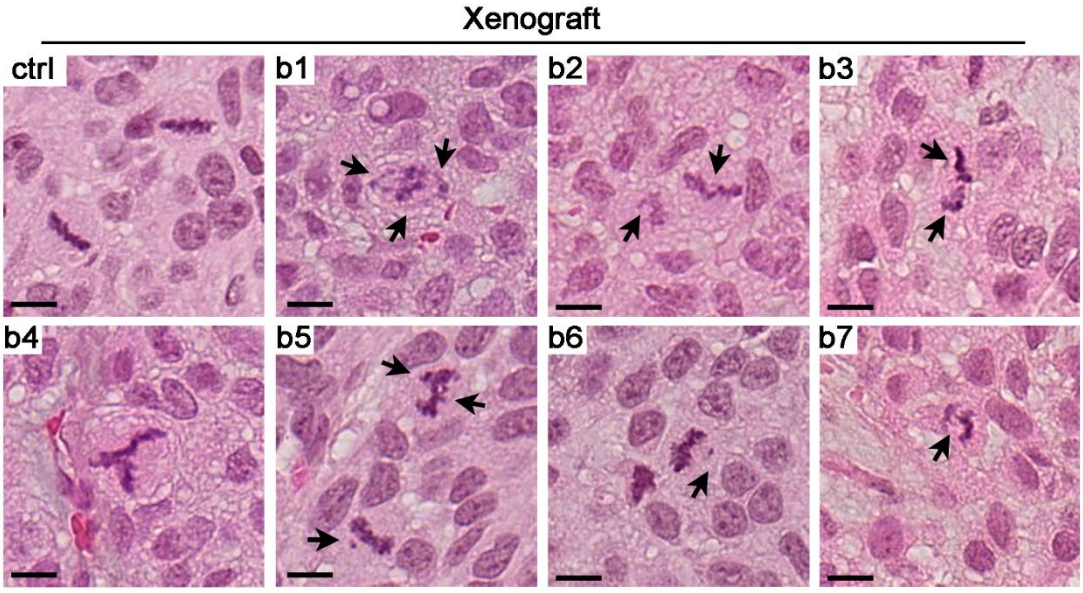


Fig. 24. Mitotic figures of the patient-derived xenograft (PDX) displayed aberrations pointing to impaired kinetochore–microtubule attachment probably due to SAC defect(s), such as misaligned chromosomes on the metaphase plate, lagging, mal-oriented, bridging or fragmented chromosomes, and mitotic asymmetries, as well as tri- or tetrapolar spindles. Bars correspond to 5 μm.

Evaluation of CAR T cell–induced tumor killing in ACC primary cultures and in commercial cell lines

B7-H3–targeted CAR T cells were generated by collaborators in the laboratory of Prof. Caruana at the University Hospital of Würzburg (Germany) and were subsequently assessed for functional activity in co-culture cytotoxicity assays using established ACC cell lines (SW13 and H295R), as well as primary tumor–derived and xenograft-derived cells (Figure 18). Non-transduced (NT) T cells displayed minimal or no cytotoxic effects, whereas B7-H3 CAR T cells mediated strong tumor cell killing across all models, consistently reducing residual tumor cell viability to low levels. Notably, cytotoxic activity was evident not only in established ACC cell lines but was even more pronounced in primary tumor– and xenograft-derived cells, demonstrating that B7-H3 CAR T cell efficacy is preserved across these heterogeneous ACC models.

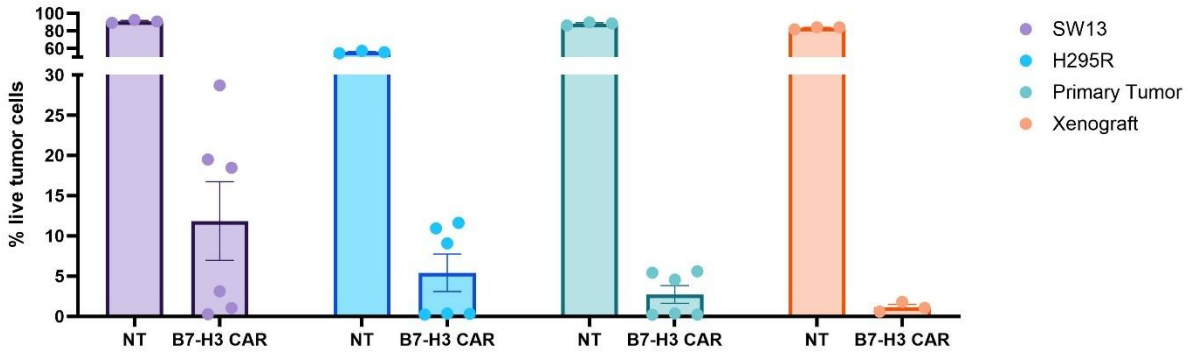


Fig.18. B7-H3 CAR T cell cytotoxicity in co-culture killing assays. Tumor cell viability was measured following co-culture with non-transduced (NT) T cells or B7-H3 CAR T cells across established ACC lines (SW13, H295R), primary tumor–derived cells, and xenograft–derived cells.

In summary, the characterization of primary tumor revealed heterogeneous expression of $p16^{INK4a}$, while the metastasis resulted entirely negative, with increase of Ki67 and mitotic indices. Findings obtained from early-passage PDXs and the CDX and the corresponding cellular models closely mirrored the aggressive p16- negative features, indicating the preservation of key features of the tumor of origin. Consistent with the resected primary tumor,

p16INK4a -negative areas in PDXs and the CDX were associated with increased Ki67 labeling and higher mitotic indexes. Notably, the CDX-bearing mouse, which received bilateral injections of a high number of cells derived from an F1 PDX, developed extensive abdominal and thoracic metastases dissemination pathways, recapitulating the terminal metastatic pattern documented by CT imaging in the patient and responsible for the fatal outcome. In line with the surgically resected patient metastases analyzed by immunohistochemistry, all metastatic lesions identified in the CDX mouse were uniformly $p16^{INK4a}$ -negative, indicating strong selective pressure for this phenotype during distant metastatic spread. Finally, the absence of significant differences in the frequency of aberrant mitoses across $p16^{INK4a}$ expression status, serial PDX passages, and CDX or metastatic lesions supports the notion that mitotic instability represents an early tumor-initiating event that is stably maintained within the NSG mouse platform.

Moreover, immunophenotypic characterization of primary tumor by MACSima showed B7H3 to be the most highly expressed marker among those evaluated. Cytofluorimetric analysis confirmed its high expression across the in vitro models. This finding enabled the development of a B7H3-targeted CAR T-cell immunotherapy, which demonstrated efficacy in functional co-culture assays using primary tumor– and xenograft-derived ACC cells.

Discussion and conclusions

Perioperative metastatic progression represents a rare and poorly understood complication of cancer surgery, with the biological and clinical factors underlying this phenomenon still largely undefined. In this context, we examined the case of a 60-year-old female patient with advanced-stage ACC, characterized by metastatic disease confined to the liver but with multiple hepatic localizations, hypercortisolism, and an IVC neoplastic thrombus with potential tumor cell shedding into the circulation [130,144]. Despite the advanced disease, the patient maintained a good performance status, supporting the feasibility of an extensive surgical approach. Delaying treatment would likely have led to clinical deterioration with progressive metastatic spread and hormonal worsening, while first-line cytoreductive chemotherapy was deemed unsuitable due to its limited timeliness in an aggressive disease setting. For these reasons, the patient underwent synchronous adrenalectomy, liver metastasectomies, and IVC thrombectomy with the aim of removing the primary tumor, debulking metastatic burden, controlling hormone excess, preventing vascular complications, and optimizing the subsequent efficacy of adjuvant mitotane therapy[130,145–149]. The surgery was successfully completed, and histopathological and immunohistochemical analyses confirmed the diagnosis of conventional high-grade adrenocortical carcinoma, with heterogeneous expression of markers including SYP, CALB2, INH, and MELAN-A, consistent with a corticosurrenal origin [130,150,151]. However, in the weeks following surgery, before therapeutic plasma levels of mitotane were achieved, the patient experienced an explosive metastatic progression, with widespread retroperitoneal and mediastinal lymphadenopathy, multiple liver and lung metastases, diffuse pleural involvement, progressive worsening of hormonal hypersecretion, and death within 40 days; an outcome markedly shorter than the reported median survival of 12.1 months for mENS@T stage IV patients [152].

Ultrastructural analysis revealed a distinct morphological heterogeneity within the neoplastic population, consistent across both the primary lesion and hepatic metastases, attributable to the presence of two distinct cellular morphotypes. The majority of the neoplasm consists of voluminous cells with open chromatin (approximately 70%), while a smaller subset displays a sustentacular phenotype with electron-dense cytoplasm, condensed nuclei and elongated cytoplasmic processes interdigitated between adjacent elements. Both cellular populations exhibited signs of lipogenesis and contained ovoid or swollen mitochondria with well-defined transverse cristae, which were particularly prominent in the clear cell variant. The abundance

of mitochondria, a well-developed biosynthetic apparatus, and evidence of lipogenesis are consistent with active hormone production by the neoplasm; however, frequent structural damage to the cristae was observed, suggestive of oxidative stress. These findings may reflect both their role in steroid hormone synthesis and the presence of hypoxic–ischemic conditions, as further supported by the occurrence of widespread areas of coagulative necrosis.

From a biological perspective, this ultrastructural diversity suggests that the tumor is composed of complementary subpopulations that may function synergistically, thereby increasing the overall survivability and resilience of the malignancy.

To elucidate the biological mechanisms driving the aggressive clinical course of this malignancy, we employed a multimodal approach integrating targeted NGS, CGH-SNP array, MSI testing, and immunohistochemistry with ultrastructural and digital pathology, and spatial proteomic. These comprehensive analyses were performed on surgical specimens and subsequently validated using early-passage patient-derived and cell-derived xenograft (PDX and CDX) platforms. These models proved to be high-fidelity surrogates, faithfully recapitulating the complex ecosystem and phenotypic traits of the parental tumors. This characterization was further strengthened by the use of PDX and CDX platforms; these early-passage models functioned as faithful biological replicas, allowing us to study the tumor ecosystem in a controlled setting that preserved the parental tumor's essential features.

While our NGS approach was characterized by a partial genome coverage restricted to 81 cancer-related genes, this targeted strategy effectively encompassed all primary (TP53, MLH1, MSH2, EPCAM, MSH6, PMS2) and secondary (PRKAR1A, MEN1, APC, NF1, FLCN) predisposition genes associated with adrenocortical carcinoma (ACC). To overcome the constraints of a targeted panel, we integrated these findings with a custom CGH–SNP array featuring a genome-wide backbone and specific SNP coverage for chromosome 11, thereby providing a comprehensive overview of the structural landscape. This analysis revealed only a 'likely oncogenic' *TP53* missense mutation [151], which maintained a stable variant allele frequency (~27%) across all tumor sites. This stability, consistent with the allelic skewing of regional SNPs, suggests a structural imbalance at the *TP53* locus. Although the profiling tools, potentially limited by local SNP density, did not fully resolve this noncanonical genomic instability, such a rearrangement could significantly impact *TP53* expression and function, a possibility warranting further investigation [153]. Ultimately, the lack of clinically significant germline mutations, mirroring the patient’s unremarkable family history, confirms that this case should be considered fundamentally sporadic.

In contrast, the genomic landscape of both the primary tumor and metastatic sites was characterized by a high burden of chromosomal-scale abnormalities, specifically arm-level copy number variations (CNVs) and copy-neutral loss of heterozygosity (CNNLOH) [154]. Such alterations serve as definitive hallmarks of chromosomal instability (CIN), a known driver of disease progression, poor prognosis, and therapeutic resistance in several malignancies, including adrenocortical carcinoma (ACC)[155–157]. While whole-genome sequencing remains the gold standard for a definitive diagnosis of CIN [157], the high frequency of aberrant mitoses observed in this study provides compelling circumstantial evidence of its presence. These mitotic defects point toward a failure in the spindle assembly checkpoint, the fundamental mechanism responsible for preserving chromosomal integrity [158–160].

Molecular characterization of five single-nucleotide repeat loci ruled out microsatellite instability (MSI), thereby excluding mismatch repair (MMR) deficiency as an alternative driver of genetic instability in this case. These functional findings were entirely consistent with the absence of both germline and somatic mutations in the MMR-related genes evaluated within our NGS panel. While MSI is a well-established predictive indicator of immunotherapy response and carries a favorable prognosis in various malignancies, *most notably colorectal cancer*, its specific clinical significance and prognostic value in adrenocortical carcinoma (ACC) remain currently undefined [161].

Among the genomic alterations identified in both the primary tumor and metastatic sites, a focal homozygous deletion at the 9p21.3 chromosomal region emerged as a critical putative driver event. High-resolution NGS analysis confirmed the total loss of the CDKN2A and CDKN2B loci, which are positioned in tandem and separated by an 11.5 kbp interval. This specific alteration was characterized by an interstitial deletion coupled with the loss of the wild-type allele and a subsequent duplication of the deleted chromosome, a mechanism that effectively ensures the complete absence of these tumor suppressors.

The functional impact of this loss is profound, as the 9p21.3 cluster serves as a master regulator of cellular homeostasis. The CDKN2A gene, through alternative splicing, generates two distinct oncosuppressive proteins: $p16^{INK4a}$ and p14ARF. While $p16I^{NK4a}$ functions as a selective CDK4/6 inhibitor to maintain the G1-S checkpoint, p14ARF stabilizes TP53 by sequestering the E3 ubiquitin ligase MDM2, thereby preventing its degradation. Complementing this, CDKN2B encodes $p15^{INK4b}$, a TGF-β-induced inhibitor of RB phosphorylation and cell cycle progression that also modulates tumor metabolism by inhibiting enolase-1.

Together, these proteins act as essential safeguards against aneuploidy, chromosomal instability (CIN), and oxidative stress. The frequent somatic deletion or epigenetic silencing of the 9p21.3

region across various malignancies underscores its vital role in preventing malignant transformation. Consequently, the loss of this protective axis not only compromises the cell's ability to manage DNA damage and reactive oxygen species (ROS) but also correlates with increased biological aggressiveness and poor clinical prognosis.[139,140].

In the present case, a significant finding is the persistence of a specific TP53 subclonal population, characterized by the missense mutation c.843C>A p.(Asp281Glu). This mutation, located within the critical DNA-binding domain responsible for mediating cell cycle arrest and apoptosis [162–165], maintained a stable variant allele frequency (VAF) of approximately 27% across both the primary tumor and metastatic sites. The conservation of this frequency suggests that the mutation is not merely a transient event, but rather contributes to a functional equilibrium essential for the maintenance and progression of the neoplastic mass.

It is plausible that this specific TP53 variant confers a selective advantage, particularly by providing a protective effect to sub-populations vulnerable to oxidative stress and hypoxic or ischemic damage [165]. Such a mechanism would act in synergy with the suppressive effects of MDM2, which is frequently overactivated in these contexts due to the loss of p14ARF inhibitory signaling[166,167].

Furthermore, while the prognostic weight of low-frequency TP53 mutations in adrenocortical carcinoma remains to be fully elucidated[168,169], evidence from other malignancies, such as chronic lymphocytic leukemia, indicates that low-VAF TP53 mutations are independent predictors of poor clinical outcomes[170]. Consequently, the presence of this stable subclonal mutation may serve as a key molecular driver behind the clinically aggressive phenotype observed in this patient.

To independently validate the homozygous CDKN2A/B deletion and characterize its topographical distribution, we performed $p16^{INK4a}$ immunohistochemistry (IHC) on both the primary tumor and metastatic lesions[137,147,148,171]. The primary tumor exhibited a distinct mosaic pattern, with alternating $p16^{INK4a}$-positive and -negative regions.

This spatial heterogeneity highlights a critical diagnostic challenge: genomic assessments of homozygous deletions derived from a single tumor fragment may be susceptible to sampling bias, potentially leading to an incomplete representation of the tumor's genetic architecture.

Within the $p16^{INK4a}$-positive sectors, the observed high staining intensity likely reflects a compensatory overexpression mechanism triggered by chromosomal instability (CIN) [150]

Notably, the identification of isolated $p16^{INK4a}$-negative cells, or small clusters thereof, nested within positive regions suggests the multifocal emergence of deleted subclones. This finding is

consistent with the significant selective advantage these alterations provide within a CIN-driven microenvironment [150].

In stark contrast, all analyzed metastatic lesions were characterized by a complete absence of $p16^{INK4a}$ expression. This transition from a heterogeneous primary tumor to uniformly $p16^{INK4a}$-negative metastases points to a powerful selective sweep or bottleneck during the metastatic process; indeed, these findings indicate that while the *CDKN2A/B* deletion emerges subclonally within the primary site, it undergoes significant positive selection during spread, confirming that this phenotype is likely a critical prerequisite for successful dissemination and colonization.

The Ki67 proliferative index, a robust marker of DNA replication that identifies nuclei across all active phases of the cell cycle, remains a critical predictor of recurrence and poor survival in patients with Adrenocortical Carcinoma. Conversely, while the Mitotic Index (MI) is fundamental for histological grading, its prognostic reliability is often limited by the fact that it captures only the transient M phase [72,76,130,151].

In this study, we identified a significant correlation between $p16^{INK4a}$-negative status and a higher Ki67 index, as well as a more modest association with elevated MI. These findings suggest that the 9p21.3 deletion acts as a primary driver of accelerated cellular proliferation, an effect most evident within the primary tumor and hepatic metastases.

Furthermore, the Mitotic Aberration Burden (MAB) frequency remained consistently high across both primary and metastatic sites, regardless of $p16^{INK4a}$ expression or regional heterogeneity. This observation is particularly salient, as the lack of significant variance between $p16^{INK4a}$-positive and -negative regions indicates that chromosome missegregation likely occurred as an early, foundational pathogenic event in the tumor's ontogeny, potentially preceding the subclonal loss of the *CDKN2A/B* locus [172].

To model the evolutionary trajectory of the primary tumor, we established subcutaneous Patient-Derived Xenografts (PDXs) in NSG mice, utilizing fragments expected to harbor both $p16^{INK4a}$-positive and -negative subpopulations [173]. All 16 established xenografts demonstrated rapid growth and, critically, maintained the histopathological, ultrastructural, and immunohistochemical architecture of the parental tumor across serial passages. This phenotypic stability included the persistence of the observed $p16^{INK4a}$ mosaicism. Within the PDX models, the $p16^{INK4a}$-negative clone emerged as the predominant population, a finding consistent with its higher Ki67 and mitotic indices, which were similarly validated in the xenograft tissue.

Interestingly, the localized persistence of $p16^{INK4a}$-positive cells suggests that a superior replicative rate alone was insufficient to achieve complete clonal dominance within the timeframe of serial passages. This suggests that the intratumoral heterogeneity observed in the

PDX is relatively stable, potentially reflecting a complex ecological balance between subclones. Furthermore, the frequency of Mitotic Aberration Burden (MAB) remained consistent with those documented in the primary and metastatic lesions, showing no significant variation relative to $p16^{INK4a}$ status or passage number.

This stability reinforces the hypothesis that defective mitosis and chromosomal instability were foundational, early-stage hallmarks of the tumor's ontogeny rather than late-acquired traits. Finally, the absence of spontaneous metastases in the PDX-bearing mice at necropsy suggests that *while* the subcutaneous model effectively recapitulates the proliferative dynamics and heterogeneity of the primary tumor, additional microenvironmental factors or anatomical contexts may be required to trigger the full metastatic cascade observed clinically.

In summary, the convergent evidence derived from both the patient's clinical course and the PDX/CDX models indicates that chromosomal instability (CIN) acted as a foundational tumor-initiating event. Within this genomic landscape, the homozygous CDKN2A/B deletion and subsequent loss of $p16^{INK4a}$ emerged as critical drivers of aggressive metastatic progression. While $p16^{INK4a}$-negative cells exhibited significantly higher Ki67 and mitotic indices in both human and murine tissues, this enhanced proliferative capacity alone does not fully account for the observed clinical behavior. Instead, our data suggest that $p16^{INK4a}$ loss serves as a key facilitator of metastatic dissemination.

The precise molecular mechanisms by which $p16^{INK4a}$ deficiency promotes metastasis in ACC remain a subject of active investigation. It is hypothesized that this loss confers a multi-faceted selective advantage, potentially through the bypass of cellular senescence, improved metabolic and respiratory fitness, and an augmented capacity for migration and invasion[138,174]

Elucidating the role of $p16^{INK4a}$ within the ACC microenvironment is essential for the development of targeted therapeutic interventions. Our findings suggest that the very instability driving this tumor might be its critical vulnerability. Future strategies could involve leveraging CIN through treatments such as radiation or low-dose microtubule-stabilizing taxanes; by further escalating genomic instability, these therapies aim to push the tumor beyond its survival threshold, ultimately inducing tumor suppression via mitotic catastrophe [175].

Multiplexed spatial analysis performed using the MACSima platform enabled an in-depth immunophenotypic profiling and spatial characterization of both the primary adrenocortical carcinoma and the corresponding liver metastasis. The spatially resolved data confirmed the immune landscape of ACC as a predominantly "cold" tumor microenvironment, in agreement with current evidence reported in the literature. Moreover, the multispatial analysis was fully concordant with immunohistochemical findings, demonstrating p16 negativity, expression of

the principal diagnostic markers, and a markedly elevated proliferative index. Of particular relevance, a strong and homogeneous expression of B7-H3 was consistently detected in both the primary tumor and the metastatic lesion. This molecular feature was preserved across all derived experimental models, including cell lines established from the primary tumor and liver metastasis, cell-derived xenografts (CDX), patient-derived xenografts (PDX), as well as in established ACC cell lines such as SW13 and H295R. The reproducible overexpression of B7-H3 across patient samples and experimental models provided a robust biological rationale for the development and evaluation of B7-H3–targeted CAR T cells. In vitro testing of these engineered CAR T cells on the newly generated ACC cell lines yielded encouraging results, supporting further in vivo validation and suggesting a potential therapeutic avenue for adrenocortical carcinoma. In addition, the CDX-derived ID7ACC cell line retained the ability to produce steroid hormones, a defining functional characteristic of both normal adrenal tissue and ACC. Collectively, these findings indicate that the generated cellular models, together with the CDX and PDX systems, faithfully recapitulate the key biological, molecular, and functional features of the original tumor, thereby representing reliable platforms for future mechanistic investigations and the preclinical testing of innovative therapeutic strategies for metastatic ACC.

Bibliography

1. Adrenal cortex development and related disorders leading to adrenal insufficiency - ScienceDirect. https://www.sciencedirect.com/science/article/pii/S0303720721000502?via%3Dihub.
2. Frontiers | Editorial: Adrenal Cortex: From Physiology to Disease. https://www.frontiersin.org/journals/endocrinology/articles/10.3389/fendo.2016.00051/full.
3. Lerario, A. M., Finco, I., LaPensee, C. & Hammer, G. D. Molecular Mechanisms of Stem/Progenitor Cell Maintenance in the Adrenal Cortex. *Front. Endocrinol.* **8**, (2017).
4. Pihlajoki, M., Dörner, J., Cochran, R. S., Heikinheimo, M. & Wilson, D. B. Adrenocortical Zonation, Renewal, and Remodeling. *Front. Endocrinol.* **6**, (2015).
5. Abusamra, Y., Patil, A. & Clayton, R. Adrenocortical hormones. *Anaesth. Intensive Care Med.* **24**, 636–638 (2023).
6. Frontiers | Functional Zonation of the Adult Mammalian Adrenal Cortex. https://www.frontiersin.org/journals/neuroscience/articles/10.3389/fnins.2016.00238/full.
7. The molecular biology, biochemistry, and physiology of human steroidogenesis and its disorders - PubMed. https://pubmed.ncbi.nlm.nih.gov/21051590/.
8. Lyraki, R. & Schedl, A. Adrenal cortex renewal in health and disease. *Nat. Rev. Endocrinol.* **17**, 421–434 (2021).
9. Kim, J.-H. & Choi, M. H. Embryonic Development and Adult Regeneration of the Adrenal Gland. *Endocrinol. Metab.* **35**, 765–773 (2020).
10. Pignatti, E., Leng, S., Carlone, D. L. & Breault, D. T. Regulation of zonation and homeostasis in the adrenal cortex. *Mol. Cell. Endocrinol.* **441**, 146–155 (2017).
11. Freedman, B. D. *et al.* Adrenocortical Zonation Results from Lineage Conversion of Differentiated Zona Glomerulosa Cells. *Dev. Cell* **26**, 666–673 (2013).

12. Hammer, G. D. & Basham, K. J. Stem cell function and plasticity in the normal physiology of the adrenal cortex. *Mol. Cell. Endocrinol.* **519**, 111043 (2021).

13. Dumontet, T. *et al.* PKA signaling drives reticularis differentiation and sexually dimorphic adrenal cortex renewal. *JCI Insight* **3**, e98394, 98394 (2018).

14. Gallo-Payet, N. & Battista, M.-C. Steroidogenesis-adrenal cell signal transduction. *Compr. Physiol.* **4**, 889–964 (2014).

15. Little, D. W., Dumontet, T., LaPensee, C. R. & Hammer, G. D. β-catenin in adrenal zonation and disease. *Mol. Cell. Endocrinol.* **522**, 111120 (2021).

16. Hoeflich, A. & Bielohuby, M. Mechanisms of adrenal gland growth: signal integration by extracellular signal regulated kinases1/2. *J. Mol. Endocrinol.* **42**, 191–203 (2009).

17. Mathieu, M. *et al.* Steroidogenic differentiation and PKA signaling are programmed by histone methyltransferase EZH2 in the adrenal cortex. *Proc. Natl. Acad. Sci. U. S. A.* **115**, E12265–E12274 (2018).

18. Lotfi, C. F. P., Kremer, J. L., dos Santos Passaia, B. & Cavalcante, I. P. The human adrenal cortex: growth control and disorders. *Clinics* **73**, e473s (2018).

19. Bornstein, S. R. *et al.* Diagnosis and Treatment of Primary Adrenal Insufficiency: An Endocrine Society Clinical Practice Guideline. *J. Clin. Endocrinol. Metab.* **101**, 364–389 (2016).

20. Fassnacht, M. *et al.* European Society of Endocrinology Clinical Practice Guidelines on the management of adrenocortical carcinoma in adults, in collaboration with the European Network for the Study of Adrenal Tumors. https://doi.org/10.1530/EJE-18-0608 (2018) doi:10.1530/EJE-18-0608.

21. Husebye, E. S. *et al.* Consensus statement on the diagnosis, treatment and follow-up of patients with primary adrenal insufficiency. *J. Intern. Med.* **275**, 104–115 (2014).

22. Pitsava, G. & Stratakis, C. A. Adrenal hyperplasias in childhood: An update. *Front. Endocrinol.* **13**, 937793 (2022).

23. Pitsava, G., Maria, A. G. & Faucz, F. R. Disorders of the adrenal cortex: Genetic and molecular aspects. *Front. Endocrinol.* **13**, 931389 (2022).

24. Arlt, W. & Allolio, B. Adrenal insufficiency. *The Lancet* **361**, 1881–1893 (2003).

25. Bouys, L. *et al.* Bilateral Adrenocortical Nodular Disease and Cushing's Syndrome. *J. Clin. Endocrinol. Metab.* **109**, 2422–2432 (2024).

26. Bourdeau, I., Parisien-La Salle, S. & Lacroix, A. Adrenocortical hyperplasia: A multifaceted disease. *Best Pract. Res. Clin. Endocrinol. Metab.* **34**, 101386 (2020).

27. Kamilaris, C. D. C., Hannah-Shmouni, F. & Stratakis, C. A. Adrenocortical tumorigenesis: lessons from genetics. *Best Pract. Res. Clin. Endocrinol. Metab.* **34**, 101428 (2020).

28. Nieman, L. K. *et al.* The Diagnosis of Cushing's Syndrome: An Endocrine Society Clinical Practice Guideline. *J. Clin. Endocrinol. Metab.* **93**, 1526–1540 (2008).

29. Funder, J. W. *et al.* The Management of Primary Aldosteronism: Case Detection, Diagnosis, and Treatment: An Endocrine Society Clinical Practice Guideline. *J. Clin. Endocrinol. Metab.* **101**, 1889–1916 (2016).

30. Kerkhofs, T. M., Roumen, R. M., Demeyere, T. B., van der Linden, A. N. & Haak, H. R. Adrenal Tumors with Unexpected Outcome: A Review of the Literature. *Int. J. Endocrinol.* **2015**, 710514 (2015).

31. Mete, O. *et al.* Overview of the 2022 WHO Classification of Adrenal Cortical Tumors. *Endocr. Pathol.* **33**, 155–196 (2022).

32. Lam, A. K.-Y. Adrenocortical Carcinoma: Updates of Clinical and Pathological Features after Renewed World Health Organisation Classification and Pathology Staging. *Biomedicines* **9**, 175 (2021).

33. Libé, R. & Huillard, O. Adrenocortical carcinoma: Diagnosis, prognostic classification and treatment of localized and advanced disease. *Cancer Treat. Res. Commun.* **37**, 100759 (2023).

34. Pittaway, J. F. H. & Guasti, L. Pathobiology and genetics of adrenocortical carcinoma. *J. Mol. Endocrinol.* **62**, R105–R119 (2019).

35. Habra, M. A. *et al.* Epidemiological risk factors for adrenocortical carcinoma: A hospital-based case-control study. *Int. J. Cancer* **146**, 1836–1840 (2020).

36. Fassnacht, M., Libé, R., Kroiss, M. & Allolio, B. Adrenocortical carcinoma: a clinician's update. *Nat. Rev. Endocrinol.* **7**, 323–335 (2011).

37. Li, Z. *et al.* Survival nomogram and risk classification system for patients with adrenocortical carcinoma: a study based on the SEER database and external validation in China. *Transl. Androl. Urol.* **13**, 493–508 (2024).

38. Angelousi, A., Kassi, E. & Kaltsas, G. A. Adrenocortical Carcinoma. in *Endotext* (eds Feingold, K. R. et al.) (MDText.com, Inc., South Dartmouth (MA), 2000).

39. Chukkalore, D., MacDougall, K., Master, V., Bilen, M. A. & Nazha, B. Adrenocortical Carcinomas: Molecular Pathogenesis, Treatment Options, and Emerging Immunotherapy and Targeted Therapy Approaches. *The Oncologist* **29**, 738–746 (2024).

40. Ilanchezhian, M. *et al.* Pediatric adrenocortical carcinoma. *Front. Endocrinol.* **13**, 961650 (2022).

41. Riedmeier, M. *et al.* Adrenocortical Carcinoma in Childhood: A Systematic Review. *Cancers* **13**, 5266 (2021).

42. Sandru, F. *et al.* Adrenocortical carcinoma: Pediatric aspects (Review). *Exp. Ther. Med.* **23**, 287 (2022).

43. Sharma, E. *et al.* The Characteristics and Trends in Adrenocortical Carcinoma: A United States Population Based Study. *J. Clin. Med. Res.* **10**, 636–640 (2018).

44. Fassnacht, M. *et al.* Adrenocortical carcinomas and malignant phaeochromocytomas: ESMO–EURACAN Clinical Practice Guidelines for diagnosis, treatment and follow-up†. *Ann. Oncol.* **31**, 1476–1490 (2020).

45. Cosentini, D., Cremaschi, V., Grisanti, S., Berruti, A. & Laganà, M. Epidemiology, Presentation, Staging, and Prognostic Factors in Adrenocortical Carcinoma. in *Primary Adrenal Malignancies* (ed. Tiberio, G. A. M.) 1–6 (Springer Nature Switzerland, Cham, 2025). doi:10.1007/978-3-031-62301-1_1.

46. Sarrafan-Chaharsoughi, Z., Yazdian Anari, P., Malayeri, A. A., Naraev, B. & Del Rivero, J. Update on Adrenocortical Carcinoma. *Urol. Clin. North Am.* **52**, 275–286 (2025).

47. Shariq, O. A. & McKenzie, T. J. Adrenocortical carcinoma: current state of the art, ongoing controversies, and future directions in diagnosis and treatment. *Ther. Adv. Chronic Dis.* **12**, 20406223211033103 (2021).

48. Allolio, B. & Fassnacht, M. Clinical review: Adrenocortical carcinoma: clinical update. *J. Clin. Endocrinol. Metab.* **91**, 2027–2037 (2006).

49. Thampi, A., Shah, E., Elshimy, G. & Correa, R. Adrenocortical carcinoma: a literature review. *Transl. Cancer Res.* **9**, 1253–1264 (2020).

50. Ni, H. & Htet, A. Editor's Pick: Adrenal Cortical Carcinoma: Clinical Perspectives. https://www.emjreviews.com/urology/article/editors-pick-adrenal-cortical-carcinoma-clinical-perspectives/ (2017).

51. Else, T. *et al.* Adrenocortical Carcinoma. *Endocr. Rev.* **35**, 282–326 (2014).

52. Fassnacht, M., Puglisi, S., Kimpel, O. & Terzolo, M. Adrenocortical carcinoma: a practical guide for clinicians. *Lancet Diabetes Endocrinol.* **13**, 438–452 (2025).

53. Ponthaud, C. de, Roy, M. & Gaujoux, S. Adrenocortical carcinoma: what you at least should know. *Br. J. Surg.* **111 8**, (2024).

54. Lerario, A. M., Mohan, D. R. & Hammer, G. D. Update on Biology and Genomics of Adrenocortical Carcinomas: Rationale for Emerging Therapies. *Endocr. Rev.* **43**, 1051–1073 (2022).

55. Sada, A. *et al.* The effect of hormonal secretion on survival in adrenocortical carcinoma: A multi-center study. *Surgery* **175**, 80–89 (2024).

56. Flauto, F. *et al.* The management of adrenocortical carcinoma in the era of precision medicine. *Crit. Rev. Oncol. Hematol.* **214**, 104839 (2025).

57. Almarzouq, A., Asfar, S., Hussain, S., Al-Hunayan, A. & Aldousari, S. Giant nonfunctioning adrenocortical carcinoma: a case report and review of the literature. *BMC Res. Notes* **7**, 769 (2014).

58. Viëtor, C. L. *et al.* How to Differentiate Benign from Malignant Adrenocortical Tumors? *Cancers* **13**, 4383 (2021).

59. Yamazaki, Y. *et al.* Updates on WHO 5th edition classification, molecular characteristics and tumor microenvironment of adrenocortical carcinomas. *Endocr. J.* **72**, 243–257 (2024).

60. Mete, O., Gucer, H., Kefeli, M. & Asa, S. L. Diagnostic and Prognostic Biomarkers of Adrenal Cortical Carcinoma. *Am. J. Surg. Pathol.* **42**, 201–213 (2018).

61. Libé, R. Adrenocortical carcinoma (ACC): diagnosis, prognosis, and treatment. *Front. Cell Dev. Biol.* **3**, 45 (2015).

62. Vocino Trucco, G., Duregon, E., Papotti, M. & Volante, M. Diagnosis and grading of adrenal cortical carcinoma. *Virchows Arch.* https://doi.org/10.1007/s00428-025-04278-0 (2025) doi:10.1007/s00428-025-04278-0.

63. Pennanen, M. *et al.* Helsinki score-a novel model for prediction of metastases in adrenocortical carcinomas. *Hum. Pathol.* **46**, 404–410 (2015).

64. Nakamura, Y. *et al.* Adrenocortical Carcinoma: Review of the Pathologic Features, Production of Adrenal Steroids, and Molecular Pathogenesis. *Endocrinol. Metab. Clin. North Am.* **44**, 399–410 (2015).

65. Yamazaki, Y. *et al.* Comparison of the methods for measuring the Ki-67 labeling index in adrenocortical carcinoma: manual versus digital image analysis. *Hum. Pathol.* **53**, 41–50 (2016).

66. Gan, W. *et al.* Diagnostic and prognostic assessments of adrenocortical carcinomas by pathological features, immunohistochemical markers and reticular histochemistry staining. *Diagn. Pathol.* **19**, 71 (2024).

67. Baudin, E. Adrenocortical Carcinoma. *Endocrinol. Metab. Clin. North Am.* **44**, 411–434 (2015).

68. Creemers, S. G. *et al.* Future directions in the diagnosis and medical treatment of adrenocortical carcinoma. *Endocr. Relat. Cancer* **23**, R43–R69 (2016).

69. Cheng, Y., Kou, W., Zhu, D., Yu, X. & Zhu, Y. Future Directions in Diagnosis, Prognosis and Disease Monitoring of Adrenocortical Carcinoma: Novel Non-Invasive Biomarkers. *Front. Endocrinol.* **12**, 811293 (2022).

70. Mihai, R. Diagnosis, treatment and outcome of adrenocortical cancer. *Br. J. Surg.* **102**, 291–306 (2015).

71. Kostiainen, I. *et al.* Adrenocortical carcinoma: presentation and outcome of a contemporary patient series. *Endocrine* **65**, 166–174 (2019).

72. Pato, E. *et al.* Clinical and Pathological Predictors of Death for Adrenocortical Carcinoma. *J. Endocr. Soc.* **8**, bvad170 (2024).

73. Lippert, J. *et al.* Targeted Molecular Analysis in Adrenocortical Carcinomas: A Strategy Toward Improved Personalized Prognostication. *J. Clin. Endocrinol. Metab.* **103**, 4511–4523 (2018).

74. Ayala-Ramirez, M. *et al.* Adrenocortical carcinoma: Clinical outcomes and prognosis of 330 patients at a tertiary care center. *Eur. J. Endocrinol. Eur. Fed. Endocr. Soc.* **169**, 891–899 (2013).

75. Elhassan, Y. S. *et al.* S-GRAS score for prognostic classification of adrenocortical carcinoma: an international, multicenter ENSAT study. *Eur. J. Endocrinol.* **186**, 25–36 (2021).

76. Beuschlein, F. *et al.* Major Prognostic Role of Ki67 in Localized Adrenocortical Carcinoma After Complete Resection. *J. Clin. Endocrinol. Metab.* **100**, 841–849 (2015).

77. Jouinot, A. & Bertherat, J. MANAGEMENT OF ENDOCRINE DISEASE: Adrenocortical carcinoma: differentiating the good from the poor prognosis tumors. *Eur. J. Endocrinol.* **178**, R215–R230 (2018).

78. Landwehr, L.-S. *et al.* Interplay between glucocorticoids and tumor-infiltrating lymphocytes on the prognosis of adrenocortical carcinoma. *J. Immunother. Cancer* **8**, e000469 (2020).

79. Pan, L.-H., Yen, C.-C., Huang, C.-J., Ng, X.-N. & Lin, L.-Y. Prognostic predictors of adrenocortical carcinoma: A single-center thirty-year experience. *Front. Endocrinol.* **14**, (2023).

80. Araujo-Castro, M. *et al.* Spanish consensus on the diagnosis and management of adrenocortical carcinoma. https://doi.org/10.1530/ERC-25-0034 (2025) doi:10.1530/ERC-25-0034.

81. Guan, Y. *et al.* Molecular Cluster Mining of Adrenocortical Carcinoma via Multi-Omics Data Analysis Aids Precise Clinical Therapy. *Cells* **11**, 3784 (2022).

82. Clay, M. R., Pinto, E. M., Fishbein, L., Else, T. & Kiseljak-Vassiliades, K. Pathological and Genetic Stratification for Management of Adrenocortical Carcinoma. *J. Clin. Endocrinol. Metab.* **107**, 1159–1169 (2022).

83. Saygili, E. S. *et al.* Machine Learning–Based Survival Prediction Tool for Adrenocortical Carcinoma. *J. Clin. Endocrinol. Metab.* **110**, e3185–e3192 (2025).

84. Zuber, S. M. *et al.* Validated predictive model for treatment and prognosis of adrenocortical carcinoma. *Surgery* **175**, 743–751 (2024).

85. Chen, T., Zeng, D., Zhou, G., Qin, L. & Qian, X. Prognostic factors and treatment outcomes in patients with adrenal cortical carcinoma: A registry-based study. *Medicine (Baltimore)* **104**, e42831 (2025).

86. Schaap, D. M. *et al.* Therapeutic frontiers in adrenocortical carcinoma: from standards to innovation. *Med. Oncol.* **42**, 311 (2025).

87. Hallanger-Johnson, J. E. Systemic therapy for adrenocortical carcinoma: a review. *AME Med. J.* **5**, (2020).

88. Kiesewetter, B. *et al.* Management of adrenocortical carcinoma: are we making progress? *Ther. Adv. Med. Oncol.* **13**, 17588359211038409 (2021).

89. Fassnacht, M. & Allolio, B. Clinical management of adrenocortical carcinoma. *Best Pract. Res. Clin. Endocrinol. Metab.* **23**, 273–289 (2009).

90. Alyateem, G. & Nilubol, N. Current Status and Future Targeted Therapy in Adrenocortical Cancer. *Front. Endocrinol.* **12**, 613248 (2021).

91. Sun, J. *et al.* Therapeutic strategies for adrenocortical carcinoma: integrating genomic insights, molecular targeting, and immunotherapy. *Front. Immunol.* **16**, (2025).

92. Terzolo, M. *et al.* Adjuvant Mitotane Treatment for Adrenocortical Carcinoma. *N. Engl. J. Med.* **356**, 2372–2380 (2007).

93. Fassnacht, M. *et al.* European Society of Endocrinology clinical practice guidelines on the management of adrenal incidentalomas, in collaboration with the European Network for the Study of Adrenal Tumors. *Eur. J. Endocrinol.* **189**, G1–G42 (2023).

94. Kimpel, O. *et al.* The Value of Local Therapies in Advanced Adrenocortical Carcinoma. *Cancers* **16**, 706 (2024).

95. Pfeffer, A. *et al.* Efficacy and Safety of Radiotherapy and Systemic Treatments in Adrenocortical Carcinoma: Systematic Review and Meta-Analysis. *J. Clin. Endocrinol. Metab.* **110**, 3599–3608 (2025).

96. Altieri, B., Ronchi, C. L., Kroiss, M. & Fassnacht, M. Next-generation therapies for adrenocortical carcinoma. *Best Pract. Res. Clin. Endocrinol. Metab.* **34**, 101434 (2020).

97. Sbiera, I. *et al.* Role of FGF Receptors and Their Pathways in Adrenocortical Tumors and Possible Therapeutic Implications. *Front. Endocrinol.* **12**, (2021).

98. Warmington, E. *et al.* PLK1 inhibitors as a new targeted treatment for adrenocortical carcinoma. *Endocr. Connect.* **13**, e230403 (2024).

99. Butz, H. *et al.* Defactinib in Combination with Mitotane Can Be an Effective Treatment in Human Adrenocortical Carcinoma. *Int. J. Mol. Sci.* **26**, 6539 (2025).

100. Ishikawa, Y. *et al.* Histopathological analysis of tumor microenvironment in adrenocortical carcinoma: Possible effects of *in situ* disorganized glucocorticoid production on tumor immunity. *J. Steroid Biochem. Mol. Biol.* **238**, 106462 (2024).

101. Georgantzoglou, N., Kokkali, S., Tsourouflis, G. & Theocharis, S. Tumor Microenvironment in Adrenocortical Carcinoma: Barrier to Immunotherapy Success? *Cancers* **13**, 1798 (2021).

102. Wu, K. *et al.* Discovery of a glucocorticoid receptor (GR) activity signature correlates with immune cell infiltration in adrenocortical carcinoma. *J. Immunother. Cancer* **11**, (2023).

103. Tourigny, D. S. *et al.* Cellular landscape of adrenocortical carcinoma at single-nuclei resolution. *Mol. Cell. Endocrinol.* **590**, 112272 (2024).

104. Lai, G. *et al.* The Characteristics of Tumor Microenvironment Predict Survival and Response to Immunotherapy in Adrenocortical Carcinomas. *Cells* **12**, 755 (2023).

105. Lu, Q., Nie, R., Luo, J., Wang, X. & You, L. Identifying Immune-Specific Subtypes of Adrenocortical Carcinoma Based on Immunogenomic Profiling. *Biomolecules* **13**, 104 (2023).

106. Zhang, Y. *et al.* Identification of Molecular Subtypes and Prognostic Characteristics of Adrenocortical Carcinoma Based on Unsupervised Clustering. *Int. J. Mol. Sci.* **24**, 15465 (2023).

107. Gao, J. *et al.* The signature of pyroptosis-related gene prognostic and immune microenvironment in adrenocortical carcinoma. *Front. Mol. Biosci.* **10**, (2023).

108. Pegna, G. J. *et al.* The Immunotherapy Landscape in Adrenocortical Cancer. *Cancers* **13**, 2660 (2021).

109. Ababneh, O. *et al.* The Efficacy and Safety of Immune Checkpoint Inhibitors in Adrenocortical Carcinoma: A Systematic Review and Meta-Analysis. *Cancers* **16**, 900 (2024).

110. Brabo, E. P., Moraes, A. B. & Neto, L. V. The role of immune checkpoint inhibitor therapy in advanced adrenocortical carcinoma revisited: review of literature. *J. Endocrinol. Invest.* **43**, 1531–1542 (2020).

111. Raj, N. *et al.* PD-1 Blockade in Advanced Adrenocortical Carcinoma. *J. Clin. Oncol.* **38**, 71–80 (2020).

112. Klein, O. *et al.* Combination immunotherapy with ipilimumab and nivolumab in patients with advanced adrenocortical carcinoma: a subgroup analysis of CA209-538. *OncoImmunology* **10**, 1908771 (2021).

113. Karwacka, I., Obołończyk, Ł., Kaniuka-Jakubowska, S. & Sworczak, K. The Role of Immunotherapy in the Treatment of Adrenocortical Carcinoma. *Biomedicines* **9**, 98 (2021).

114. Drewniak-Świtalska, M., Fortuna, P. & Krzystek-Korpacka, M. Negative Immune Checkpoint Inhibitors. *Pharmaceutics* **17**, 713 (2025).

115. Yin, Q. *et al.* Immune-related adverse events of immune checkpoint inhibitors: a review. *Front. Immunol.* **14**, (2023).

116. Jimenez, C. *et al.* Endocrine and Neuroendocrine Tumors Special Issue—Checkpoint Inhibitors for Adrenocortical Carcinoma and Metastatic Pheochromocytoma and Paraganglioma: Do They Work? *Cancers* **14**, 467 (2022).

117. Sedlack, A. J. H. *et al.* Preclinical Models of Adrenocortical Cancer. *Cancers* **15**, 2873 (2023).

118. Kiseljak-Vassiliades, K. *et al.* American Association of Clinical Endocrinology Disease State Clinical Review on the Evaluation and Management of Adrenocortical Carcinoma in an Adult: a Practical Approach. *Endocr. Pract.* **26**, 1366–1383 (2020).

119. Ruggiero, C., Doghman-Bouguerra, M. & Lalli, E. How good are the current models of adrenocortical carcinoma for novel drug discovery? *Expert Opin. Drug Discov.* **17**, 211–213 (2022).

120. Feely, S., Mullen, N., Donlon, P., Hantel, C. & Dennedy, M. C. 8468 Development And Characterisation Of Three-Dimensional Cell Culture Models Of Adrenocortical Carcinoma. *J. Endocr. Soc.* **8**, bvae163.166 (2024).

121. Feely, S. *et al.* Development and Characterization of 3-Dimensional Cell Culture Models of Adrenocortical Carcinoma. *Endocrinology* **166**, bqae159 (2025).

122. Dedhia, P. H. *et al.* A 3D adrenocortical carcinoma tumor platform for preclinical modeling of drug response and matrix metalloproteinase activity. *Sci. Rep.* **13**, 15508 (2023).

123. Pinto, E. M., Kiseljak-Vassiliades, K. & Hantel, C. Contemporary preclinical human models of adrenocortical carcinoma. *Curr. Opin. Endocr. Metab. Res.* **8**, 139–144 (2019).

124. Kar, A., Wierman, M. E. & Kiseljak-Vassiliades, K. Update on in-vivo preclinical research models in adrenocortical carcinoma. *Curr. Opin. Endocrinol. Diabetes Obes.* **27**, 170–176 (2020).

125. Richards, S. *et al.* Standards and guidelines for the interpretation of sequence variants: a joint consensus recommendation of the American College of Medical Genetics and Genomics and the Association for Molecular Pathology. *Genet. Med. Off. J. Am. Coll. Med. Genet.* **17**, 405–424 (2015).

126. Li, M. M. *et al.* Standards and Guidelines for the Interpretation and Reporting of Sequence Variants in Cancer: A Joint Consensus Recommendation of the Association for Molecular Pathology, American Society of Clinical Oncology, and College of American Pathologists. *J. Mol. Diagn. JMD* **19**, 4–23 (2017).

127. Bocca, P. *et al.* Bevacizumab-mediated tumor vasculature remodelling improves tumor infiltration and antitumor efficacy of GD2-CAR T cells in a human neuroblastoma preclinical model. *Oncoimmunology* **7**, e1378843 (2017).

128. Donovan, T. A. *et al.* Mitotic Figures-Normal, Atypical, and Imposters: A Guide to Identification. *Vet. Pathol.* **58**, 243–257 (2021).

129. Cree, I. A. *et al.* Counting mitoses: SI(ze) matters! *Mod. Pathol. Off. J. U. S. Can. Acad. Pathol. Inc* **34**, 1651–1657 (2021).

130. Mete, O. *et al.* Overview of the 2022 WHO Classification of Paragangliomas and Pheochromocytomas. *Endocr. Pathol.* **33**, 90–114 (2022).

131. Huang, W., Nebiolo, C., Esbona, K., Hu, R. & Lloyd, R. Ki67 index and mitotic count: Correlation and variables affecting the accuracy of the quantification in endocrine/neuroendocrine tumors. *Ann. Diagn. Pathol.* **48**, 151586 (2020).

132. Melchinger, P. & Garcia, B. M. Mitochondria are midfield players in steroid synthesis. *Int. J. Biochem. Cell Biol.* **160**, 106431 (2023).

133. Prasad, R., Kowalczyk, J. C., Meimaridou, E., Storr, H. L. & Metherell, L. A. Oxidative stress and adrenocortical insufficiency. *J. Endocrinol.* **221**, R63-73 (2014).

134. Styk, J. *et al.* Microsatellite instability assessment is instrumental for Predictive, Preventive and Personalised Medicine: status quo and outlook. *EPMA J.* **14**, 143–165 (2023).

135. Stelzer, G. *et al.* The GeneCards Suite: From Gene Data Mining to Disease Genome Sequence Analyses. *Curr. Protoc. Bioinforma.* **54**, 1.30.1-1.30.33 (2016).

136. Vij, M. *et al.* P16 immunohistochemistry is a sensitive and specific surrogate marker for CDKN2A homozygous deletion in gliomas. *Acta Neuropathol. Commun.* **11**, 73 (2023).

137. Sihag, S. *et al.* Next-Generation Sequencing of 487 Esophageal Adenocarcinomas Reveals Independently Prognostic Genomic Driver Alterations and Pathways. *Clin. Cancer Res. Off. J. Am. Assoc. Cancer Res.* **27**, 3491–3498 (2021).

138. Qiao, J. *et al.* CDKN2A Deletion Leading to Hematogenous Metastasis of Human Gastric Carcinoma. *Front. Oncol.* **11**, 801219 (2021).

139. van Dijk, E. *et al.* Chromosomal copy number heterogeneity predicts survival rates across cancers. *Nat. Commun.* **12**, 3188 (2021).

140. Hamdan, A. & Ewing, A. Unravelling the tumour genome: The evolutionary and clinical impacts of structural variants in tumourigenesis. *J. Pathol.* **257**, 479–493 (2022).

141. Xia, Y. *et al.* Dominant role of CDKN2B/p15INK4B of 9p21.3 tumor suppressor hub in inhibition of cell-cycle and glycolysis. *Nat. Commun.* **12**, 2047 (2021).

142. Huang, L. E. Impact of CDKN2A/B Homozygous Deletion on the Prognosis and Biology of IDH-Mutant Glioma. *Biomedicines* **10**, 246 (2022).

143. Fassl, A., Geng, Y. & Sicinski, P. CDK4 and CDK6 kinases: From basic science to cancer therapy. *Science* **375**, eabc1495 (2022).

144. Quencer, K. B., Friedman, T., Sheth, R. & Oklu, R. Tumor thrombus: incidence, imaging, prognosis and treatment. *Cardiovasc. Diagn. Ther.* **7**, S165–S177 (2017).

145. Dressler, L. *et al.* Comparative assessment of genes driving cancer and somatic evolution in non-cancer tissues: an update of the Network of Cancer Genes (NCG) resource. *Genome Biol.* **23**, 35 (2022).

146. Liu, W., Bahig, H. & Palma, D. A. Oligometastases: Emerging Evidence. *J. Clin. Oncol. Off. J. Am. Soc. Clin. Oncol.* **40**, 4250–4260 (2022).

147. Pilon, C. *et al.* Inactivation of the p16 tumor suppressor gene in adrenocortical tumors. *J. Clin. Endocrinol. Metab.* **84**, 2776–2779 (1999).

148. Vij, M. *et al.* P16 immunohistochemistry is a sensitive and specific surrogate marker for CDKN2A homozygous deletion in gliomas. *Acta Neuropathol. Commun.* **11**, 73 (2023).

149. Laan, D. V. *et al.* Adrenocortical carcinoma with inferior vena cava tumor thrombus. *Surgery* **161**, 240–248 (2017).

150. Patel, S., Wilkinson, C. J. & Sviderskaya, E. V. Loss of Both CDKN2A and CDKN2B Allows for Centrosome Overduplication in Melanoma. *J. Invest. Dermatol.* **140**, 1837-1846.e1 (2020).

151. Huang, W., Nebiolo, C., Esbona, K., Hu, R. & Lloyd, R. Ki67 index and mitotic count: Correlation and variables affecting the accuracy of the quantification in endocrine/neuroendocrine tumors. *Ann. Diagn. Pathol.* **48**, 151586 (2020).

152. Libé, R. *et al.* Prognostic factors in stage III-IV adrenocortical carcinomas (ACC): an European Network for the Study of Adrenal Tumor (ENSAT) study. *Ann. Oncol. Off. J. Eur. Soc. Med. Oncol.* **26**, 2119–2125 (2015).

153. Chen, X. *et al.* Recurrent somatic structural variations contribute to tumorigenesis in pediatric osteosarcoma. *Cell Rep.* **7**, 104–112 (2014).

154. Yang, Z., Carrio-Cordo, P. & Baudis, M. Copy number variation heterogeneity reveals biological inconsistency in hierarchical cancer classifications. *Mol. Cytogenet.* **17**, 26 (2024).

155. Russell, A. J., Sibbald, J., Haak, H., Keith, W. N. & McNicol, A. M. Increasing genome instability in adrenocortical carcinoma progression with involvement of chromosomes 3, 9 and X at the adenoma stage. *Br. J. Cancer* **81**, 684–689 (1999).

156. Zheng, S. *et al.* Comprehensive Pan-Genomic Characterization of Adrenocortical Carcinoma. *Cancer Cell* **29**, 723–736 (2016).

157. Chen, X., Agustinus, A. S., Li, J., DiBona, M. & Bakhoum, S. F. Chromosomal instability as a driver of cancer progression. *Nat. Rev. Genet.* **26**, 31–46 (2025).

158. Martínez-A, C. & van Wely, K. H. M. Centromere fission, not telomere erosion, triggers chromosomal instability in human carcinomas. *Carcinogenesis* **32**, 796–803 (2011).

159. Pagotto, S. *et al.* Hsa-miR-155-5p drives aneuploidy at early stages of cellular transformation. *Oncotarget* **9**, 13036–13047 (2018).

160. Guerrero, A. A. *et al.* Centromere-localized breaks indicate the generation of DNA damage by the mitotic spindle. *Proc. Natl. Acad. Sci. U. S. A.* **107**, 4159–4164 (2010).

161. Stelzer, G. *et al.* The GeneCards Suite: From Gene Data Mining to Disease Genome Sequence Analyses. *Curr. Protoc. Bioinforma.* **54**, 1.30.1-1.30.33 (2016).

162. Kato, S. *et al.* Understanding the function-structure and function-mutation relationships of p53 tumor suppressor protein by high-resolution missense mutation analysis. *Proc. Natl. Acad. Sci. U. S. A.* **100**, 8424–8429 (2003).

163. Kotler, E. *et al.* A Systematic p53 Mutation Library Links Differential Functional Impact to Cancer Mutation Pattern and Evolutionary Conservation. *Mol. Cell* **71**, 178-190.e8 (2018).

164. Aubrey, B. J., Strasser, A. & Kelly, G. L. Tumor-Suppressor Functions of the TP53 Pathway. *Cold Spring Harb. Perspect. Med.* **6**, a026062 (2016).

165. Shi, T., van Soest, D. M. K., Polderman, P. E., Burgering, B. M. T. & Dansen, T. B. DNA damage and oxidant stress activate p53 through differential upstream signaling pathways. *Free Radic. Biol. Med.* **172**, 298–311 (2021).

166. Kim, W. Y. & Sharpless, N. E. The regulation of INK4/ARF in cancer and aging. *Cell* **127**, 265–275 (2006).

167. Nag, S., Qin, J., Srivenugopal, K. S., Wang, M. & Zhang, R. The MDM2-p53 pathway revisited. *J. Biomed. Res.* **27**, 254–271 (2013).

168. Sidhu, S. *et al.* Mutation and methylation analysis of TP53 in adrenal carcinogenesis. *Eur. J. Surg. Oncol. J. Eur. Soc. Surg. Oncol. Br. Assoc. Surg. Oncol.* **31**, 549–554 (2005).

169. Assié, G. *et al.* Value of Molecular Classification for Prognostic Assessment of Adrenocortical Carcinoma. *JAMA Oncol.* **5**, 1440 (2019).

170. Bomben, R. *et al.* TP53 Mutations with Low Variant Allele Frequency Predict Short Survival in Chronic Lymphocytic Leukemia. *Clin. Cancer Res. Off. J. Am. Assoc. Cancer Res.* **27**, 5566–5575 (2021).

171. Fortin Ensign, S. P. *et al.* Translational significance of CDKN2A/B homozygous deletion in isocitrate dehydrogenase-mutant astrocytoma. *Neuro-Oncol.* **25**, 28–36 (2023).

172. Levine, M. S. & Holland, A. J. The impact of mitotic errors on cell proliferation and tumorigenesis. *Genes Dev.* **32**, 620–638 (2018).

173. Gu, A., Li, J., Li, M.-Y. & Liu, Y. Patient-derived xenograft model in cancer: establishment and applications. *MedComm* **6**, e70059 (2025).

174. Al-Ansari, M. M. *et al.* p16INK4A represses breast stromal fibroblasts migration/invasion and their VEGF-A-dependent promotion of angiogenesis through Akt inhibition. *Neoplasia* **14**, 1269–1277 (2012).

175. Cosper, P. F., Copeland, S. E., Tucker, J. B. & Weaver, B. A. Chromosome Missegregation as a Modulator of Radiation Sensitivity. *Semin. Radiat. Oncol.* **32**, 54–63 (2022).